Title
Multilayer Interface Tracking Model of Zircaloy Corrosion Under Irradiation

Author
Reyes, Michael Patrick

Publication Date
2018

Peer reviewed|Thesis/dissertation

UNIVERSITY OF CALIFORNIA

Los Angeles

Multilayer Interface Tracking Model of Zircaloy Corrosion Under Irradiation

A dissertation submitted in partial satisfaction of the requirements for the degree Doctor of Philosophy in Mechanical Engineering

By

Michael Patrick Reyes

2018

ABSTRACT OF THE DISSERTATION

Multilayer Interface Tracking Model of

Zircaloy Corrosion Under Irradiation

by

Michael Patrick Reyes

Doctor of Philosophy in Mechanical Engineering

University of California, Los Angeles

Professor Jaime Marian, Chair

A one dimensional numerical model is presented to predict oxide scale growth and failure in zirconium clad exposed to water in out-of-pile as well as in-pile conditions. A Stefan model coupled to diffusion kinetics tracks the interfaces between the two oxide sublayers formed on top of the metal clad. The model involves a temperature dependence to account for the thermal gradient inside the clad. A mechanical failure criterion incorporates the accumulation of compressive stresses in the oxide near the metal interface. In Chapter 2, the results of oxygen diffusion spanning the clad, time-dependent oxide formation and stress induced oxide fragmentation are presented. The results show that the oxide grows as the cubic root of time due to a charge distribution near the oxide interface. Alloying is capable of suppressing this charge distribution which accounts for square root growth in certain Zr alloys. A sensitivity study has shown that ± 15% variations on relevant model parameters produce ± 5% changes in model predictions.

In Chapter 3, the oxidation model adds the effect of radiation enhanced diffusion (RED). The RED assumes a linear formulation for low dose rates due to defect recombination while it assumes a quadratic formulation for high damage rates due because of defect annihilation. The results have found that the corrosion is accelerated and the oxide growth rate increases fivefold as a function of dose rate.

In Chapter 4, the effects of hydride formation are incorporated to the oxidation model. The hydride extension is coupled to the oxidation interface tracking model to follow hydrogen diffusion in the oxide and the metal. The terminal solid solubility for precipitation (TSSP) criterion accounts for hydride growth since hydrogen diffusion in the oxide is the rate-limiting step. The flux boundary condition in the water-oxide interface is incorporated to account for the ability of the oxide to impede hydrogen diffusion. This set of results found that hydride formation is possible above the TSSP while hydride growth is instantaneous in the metal. A desorption analysis has shown that effect of hydrogen resorption is minimal for hydride nucleation.

The dissertation of Michael Patrick Reyes is approved.

Gregory Carman

Timothy Fisher

Gaurav Sant

Jaime Marian, Committee Chair

University of California, Los Angeles

2018

DEDICATION

I dedicate this dissertation to my parents for the love and support they have given me throughout my life.

University of California, Los Angeles

2018

Table of Contents

Chapter 1: Introduction 1

Chapter 2: Multilayer Oxidation 15

Chemical reaction kinetics model 15

Chemistry of low-temperature Zr oxide reaction 15

Qualitative picture of the structural growth of zirconia films 16

Oxidation Kinetic Model 19

Stage 2: ZrO_2 layer breakaway growth 24

Temperature gradient calculation 25

Determining the Stage 1 to Stage 2 transition time 27

Procedure for numerical solution 30

Oxidation model parameterization 32

Oxidation model results 40

Pure Zr 40

Sensitivity analysis of key parameters 46

Alloy composition effects 47

Discussion of oxidation model results 49

Conclusions of oxidation model 52

Chapter 3: Irradiation Enhanced Corrosion 53

Oxidation kinetics model with irradiation 53

Overview of hydride formation 53

Models of radiation enhanced diffusion 55

Irradiated oxidation model parameterization 56

Oxidation model with irradiation results 60

Oxide scale evolutions with irradiation 60

Oxide growth rate evolutions with irradiation 61

Discussion of irradiation model results 63

Conclusions of oxidation model with irradiation 65

Chapter 4: Multilayer Hydriding 67

Chemical reaction kinetics model 67

Overview of hydride formation 67
Hydride formation kinetic model 68
Procedure for numerical solution 70
Oxidation model parameterization 72
Hydride formation model results 75
Hydrogen diffusion in the oxide 75
Hydride formation in zircaloy-4 metal 77
Discussion of hydride formation model results 79
Conclusions of hydride formation model 82
Appendix A: Analysis for justifying an exponentially-decaying charge density 84
Appendix B: Analysis for stability criterion 86
References 88

Table of Figures

Figure 1-1 4

Figure 1-2 9

Figure 1-3 10

Figure 2-1 20

Figure 2-2 34

Figure 2-3 41

Figure 2-4 42

Figure 2-5 43

Figure 2-6 44

Figure 2-7 45

Figure 2-8 46

Figure 2-9 47

Figure 2-10 48

Figure 3-1 53

Figure 3-2 54

Figure 3-3 58

Figure 3-4 59

Figure 3-5 61

Figure 3-6 62

Figure 3-7 63

Figure 4-1 69

Figure 4-2 76

Figure 4-3 77

Figure 4-4 78

Figure 4-5 79

Table of Tables

Table 2-1 33

Table 2-2 39

Table 2-3 49

Table 3-1 57

Table 3-2 60

Table 4-1 73

Table 4-2 75

ACKNOWLEDGEMENTS

This research was supported by my chair Jaime Marian and also the Consortium for Advanced Simulation of Light Water Reactors (CASL), an Energy Innovation Hub for Modeling and Simulation of Nuclear Reactors under U.S. Department of Energy Contract No. DE-AC05-00OR22725. Discussions with A. Couet, A. Motta, B. D. Wirth, A. Van der Ven, G. Was P. Wang, G. Was, and D. Xu are also acknowledged.

Chapter 2 is a version of [166] which has been published. The main source of discussions for [166] has come from J. Marian, the PI. A. Aryanfar developed the earlier version of the oxidation model; I have redone and redeveloped the model from beginning to end. S.W. Baek has assisted me in the analysis of the model. Chapter 3 is a version of [167] which is still unpublished in preparation. The main source of discussions for [167] has come from J. Marian. P. Wang and G. Was provided the experimental data for my simulation of the radiation enhanced diffusion model.

University of California, Los Angeles

2018

VITA

Michael Reyes

University of California, Los Angeles

2018

EDUCATION:

Masters of Science: Electrical Engineering: University of California, Davis. December 2007. 3.83/4.0 GPA.

Bachelor of Science, Electrical Engineering: University of California, Davis. June 2004. 3.68/4.0 GPA. Graduated with Honors.

Bachelor of Science, Biochemistry: University of California, Davis. March 1998. 3.4/4.0 GPA.

PUBLICATIONS:

M. Reyes, P. Wang, G. Was, and J. Marian. "Experimentally-validated Model of Zircaloy Clad Oxidation under Irradiation", *Journal of Nuclear Materials*, TBD, Date TBD

M. Reyes, A. Aryanfar, S. Baek, and J. Marian. "Multilayer Interface Tracking Model of Zirconium Clad Oxidation", *Journal of Nuclear Materials*, vol. 509, pp. 550–565, July 2018.

M. Reyes and R. Fearing. "Macromodel for the Mechanics of Gecko Hair Adhesion", *Proc. IEEE Int. Conf. on Robotics and Automation*, Pasadena, CA, May 2008.

PROFESSIONAL EXPERIENCE:

Engineering Intern, Hoshida and Reyes, May 2014 – May 2015, Supervisor: Allan Hoshida

Flight Controls Engineer, Boeing Company, June 2012 –April 2014, Supervisor: Jack Emadi

AAR/VMS Engineer, Northrop Grumman-Aerospace Systems, Dec 2008 –May 2012, Supervisors: Mike Gomez, Dave Leverich and John Baez

Embedded Controls Engineer, General Electric Infrastructure-Transportation, June 2008 – December 2008, Supervisor: Brian Lawry

ACADEMIC EXPERIENCE:

Research Assistant, University of California, Los Angeles Department of Materials Science, July 2016 – Present, Adviser: Dr. Jaime Marian.

Teaching Assistant, University of California, Los Angeles Department of Mechanical Engineering, January 2016 – March 2016, Supervisor: Dr. John Kim, April 2016 – June 2016, Supervisor: Dr. Ajit Mal, September 2016 – December 2016, Supervisor: Dr. Giacomo Po

Research Assistant, University of California, Berkeley Department of Electrical Engineering and Computer Science, March 2006 – October 2007, Adviser: Dr. Ron Fearing

Teaching Assistant, University of California, Davis Department of Physics, April 2007 – June 2007. Supervisor: Laura Peterson

Tutor, University of California, Davis Learning Skills Center, April 1996 – September 1996. Supervisor: Alfred Wilks

1. Chapter 1: Introduction

Containing implications in many fields of engineering, corrosion of metallic structures is an important and broad phenomenon [1–3]. Since nuclear reactor cores have compounded effects of high temperature, mechanical stresses, complex coolant and fuel chemistry, and irradiation, understanding the corrosion kinetics of metallic materials is particularly challenging [4, 5]. Fuel rods, which consist of long metallic tubes (nuclear fuel cladding) along with uranium dioxide pellets, are the primary form of nuclear fuel used in reactors [6]. The cladding represents the first barrier preventing fission product release into the coolant side [6]. To be able to ensure integrity during service in reactor cores, the metallic cladding material must satisfy the following three requirements. First, corrosion resistance is required to prevent the access of the coolant to the fissionable fuel, and also inhibit releasing the fissionable product to the coolant side; in addition this corrosion resistance precludes the breakdown of the cladding [7]. Second, strong mechanical properties are needed to support the reactor core, and to prevent the fissionable fuel from distorting and swelling the clad due to forces and stresses applied from the nuclear reaction processes [7]. Third, “low thermal neutron capture cross section” is necessary to transfer irradiated products at extremely high rates; the low cross section allows for neutron transparency to form more fission with neighboring clads [7]. Neutron cross section is defined as the probability of the neutron interacting with the atom where a low neutron cross section results in lower probabilities of neutron reaction and absorption [7, 8]. In addition to low cross section, the coolant, which serves as a moderator, slows down the faster neutrons to create fissionable products [8]. Conversely, the reactor core needs control rods to absorb neutrons for stopping and controlling the fission chain reaction; hafnium, boron and cobalt-59 are common elements in control rods [8]. Fourth, high thermal conductivity is needed to transfer heat from the fuel elements (primary heat exchanger) to the secondary heat exchangers during steam generation [7].

Since they have exhibited adequate mechanical properties and corrosion resistance at high temperatures, zirconium alloys are chosen as cladding materials in fuel elements in light-water nuclear reactors (LWR) to provide a mechanical barrier with a low impact on neutron economy between the coolant (water) and the fuel [7, 9–12]. Even though the corrosion performance deteriorates for purer alloys, with the purest metal exhibiting post-transition behavior, zirconium ores are abundant and are inexpensive to fabricate [6, 7]. Alloying additions have improved the corrosion resistance of the cladding by lowering the conductivity of the oxygen ions; for example, zirconium-niobium materials and zircaloy-2 (Zr–1.5% Sn, 0.14% Fe, 0.10% Cr, 0.06% Ni) have exhibited enhanced mechanical strength, hardness and corrosion resistance [6, 7, 12]. Since zircaloy-2 alloys are susceptible to increased hydrogen absorption possibly leading to cladding embrittlement, zircaloy-4 (Zr–1.5% Sn, 0.24% Fe, 0.13% Cr) has been developed to reduce hydrogen pickup and further increase corrosion resistance; the tin, chromium and iron content account for corrosion resistance while the chromium and iron content account for increased hardness [6, 7]. A requirement met by all zirconium alloys regardless of purity is the low thermal neutron capture (low neutron absorption cross section). This requirement is achieved by separating zirconium from hafnium via "counter-current solvent (nitric acid) extraction" since hafnium is an avid neutron absorber [8, 13]. However, this separation along with processes inside the reactor core results in the deposition and irradiation of neutron absorbing corrosion products such as boron-10 (from lithium borate) and cobalt-59 (forms cobalt-60 after absorbing neutrons) which could stop fission [14]. On the contrary, zirconium alloys remain transparent to neutrons in the presence of boron-10 and cobalt-59 because these corrosion products dissolve as the coolant is heated inside the reactor core [14]. Another requirement met by all zirconium alloys is the high thermal conductivities since heat is transferred from the fuel to the coolant, and from coolant to steam generator [7,8].

Since both oxygen and hydrogen penetrates the clad, Zr cladding is subjected to corrosion from the coolant (water) and fuel sides. The oxidation and hydriding performance of zirconium fuel components in LWRs may limit the maximum fuel discharge burn-up, which makes corrosion a critical aspect of Zr materials response in nuclear environments [15–20]. The corrosion process commences when the oxygen is partitioned from the dissociated water molecule and gets adsorbed by an oxygen vacancy site at the surface of the oxide layer [6]. In the presence of a concentration gradient and electric potential across the oxide, the oxygen diffuses along the grain boundaries; at the oxide metal interfaces these oxygen ions react with zirconium cation vacancies to yield monoclinic zirconia (ZrO_2) and also release electrons to reduce the hydrogen ions [6]. Large compressive stresses due to the large Pilling-Bedworth (PB) ratio of 1.56 causes the columnar oxide growth; as the oxide grows; stress accumulates which eventually causes the formation of lateral cracks and subsequent interlinkage of porosity allowing access of the coolant into the oxide-metal interface [6, 17].

Autoclave experiments are the typical means to study corrosion in LWR, where the cladding components are subjected to temperatures and pressures representative of reactor operation [21–23]. As shown in Figure 1-1, the temperatures in the nuclear reactor can be at most 647 K (374℃) given a pressure of 218 atm [24]. These tests can be executed in-pile, with the autoclave directly experiencing conditions in the reactor core, or out-of-pile, with experiments done under controllable laboratory conditions. Since conditions in the reactor core are mimicked, in-pile experiments are considered more scientifically relevant; however they are costly, highly time consuming to perform, and the different contributing factors are difficult to separate [25, 26]. Although out-of-pile autoclave corrosion tests has the ability to predict particular features of in-pile corrosion performance of zirconium alloys, these autoclave experiments normally underestimate corrosion rates and fail to account for enhanced corrosion due to irradiation [12,

26–28]. Several models of zirconium alloy corrosion and hydride embrittlement processes have been developed over the years to reconcile the gap between autoclave measurements and in-reactor Zr corrosion, [29–34]. Since these models focus only on certain aspects from the experimental observations of oxidation and hydriding, they are formulated to reproduce observed experimental time evolutions but do not explain the underlying causes behind the produced data. These models cannot be used for materials evaluation and design since they fail to predict the causes of the experimental observations.

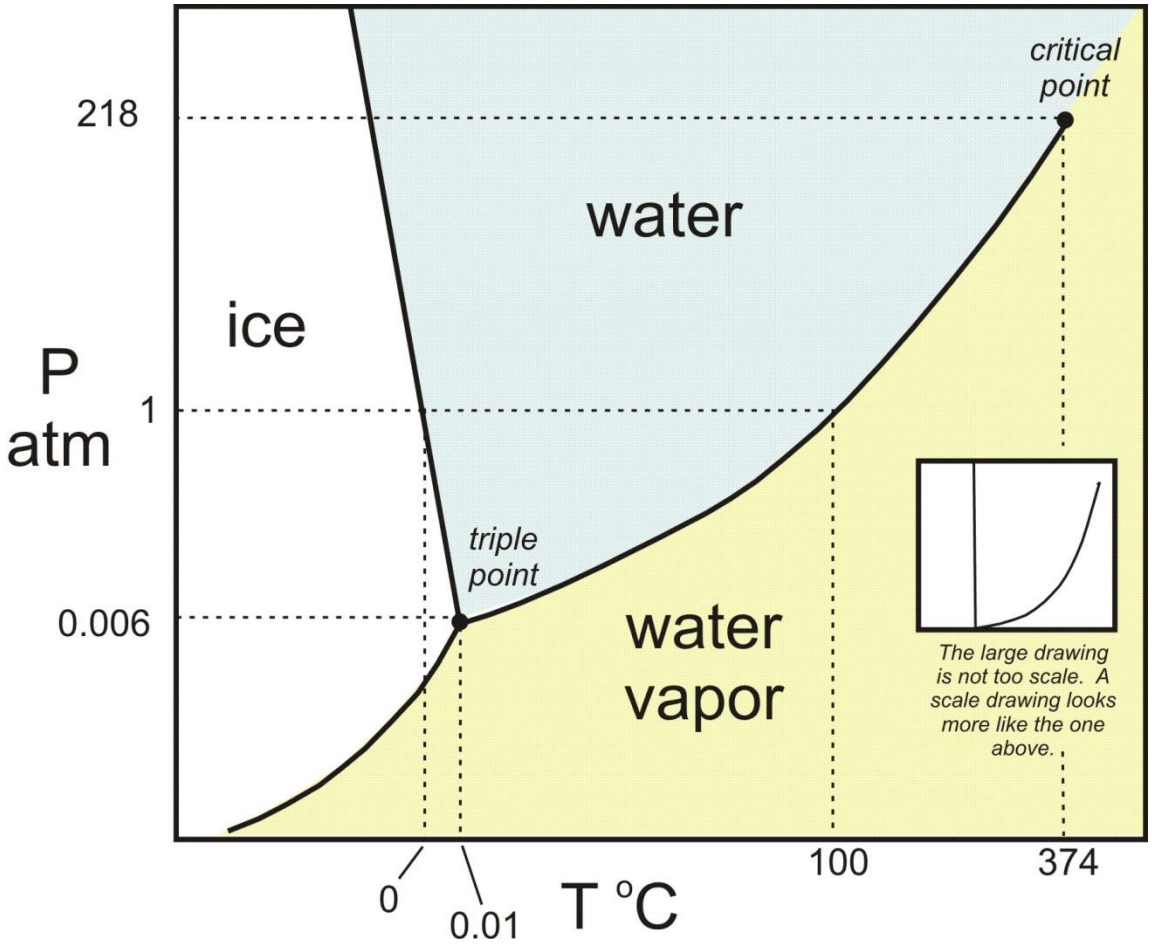

Figure 1-1: Phase diagram for water in terms of pressure and temperature [24]

Based on the phenomenology of corrosion, oxidation and hydriding are typically treated as separate processes, even though ample evidence suggests the existence of coupling between

oxygen and hydrogen pickup and transport which must be considered jointly in the corrosion of Zr [35–37]. This is partially due to the hydride platelet accumulation where a clearly distinguishable outer oxide scale and inner region forms. In keeping with this distinction, in the second chapter of this dissertation I focus on the zirconium cladding oxidation kinetics, assuming no synergistic effects from hydrogen on oxygen transport and reaction. An additional challenge of considering Zr oxidation is the observation of an anomalous oxide layer thickness growth law that does not follow the classical $\sim t^{1/2}$ scaling observed under the assumption of diffusion-limited kinetics but instead scales as $\sim t^{1/3}$ [38–42]. Several explanations exist that have been put forward to explain this anomaly, including charge imbalance [39], and hydrogen/oxygen coupling [37]. However, this cubic growth law has been clearly revealed by detailed experiments of zircaloy exposure to oxygen-only conditions which cast doubt on hydrogen's role in facilitating a deviation from an ideally diffusive behavior [43–45]. Gondi and Missigoli [46] have explained and rationalized that the cubic growth dependence is based on the existence of a concentration gradient of anionic vacancies, which are generated at the oxide-metal interface and assumed an exponential decay in space. Likhanskii and Evdokimov [35] take this line of thought further by relating the vacancy concentration gradient to differences in the Fermi level across the oxide/metal interface, which creates an electric field that is compensated by a differential vacancy concentration. Cubic growth develops under such conditions – and when the Fermi level of oxide is above that of the metal.

During post-transition kinetics, the zirconium oxide layer loses its protective properties when it catastrophically cracks because of the accumulation of compressive stresses at the oxide/metal interface. Delamination or buckling or by shear cracking can cause the occurrence of cracking under compression, which eventually lead to spall (fragmentation) [41]. This can also be aided by microstructural features such as grain boundaries and second-phase particles. Alloys

with enhanced corrosion resistance such as Zircaloy-2 and 4 and/or ZIRLO, however, are seen to undergo a renewed growth stage during their reconstitution after the breakdown of the oxide layer [18]. High temperature is also known to mitigate the breakdown of the oxide scale and the oxide scale has an expectation to entirely recover above 300℃. Nonetheless, the failure mechanisms of the Zr oxide layer are not yet fully understood, and a full thermo-mechanical model linking growth and failure is still lacking in the literature [11, 36, 47].

In the third chapter of this dissertation, irradiation effects needs to be coupled with the corrosion of zirconium assuming no hydriding effects since enough irradiation is still present to alter the corrosion kinetics despite the cladding's strong mechanical properties. Studies show that radioactive particles accelerate the corrosion due to enhanced diffusion [48–51]. Processes and reactions in the zirconium crystals provide an explanation on the mechanism of enhanced diffusion. During oxygen diffusion through the solid, neutron irradiation generates defects in the zirconium cation vacancies and/or interstitials [52]. In addition to irradiation, strain rates sufficient to cause dislocation can produce plastic flows that form defects [52]. As they migrate through the crystal at high temperatures, the defects get annihilated by recombination or trapped at the dislocations [52]. When the mobile vacancies and interstitials anneal until they reach a steady state concentration, diffusion rate is augmented [52]. Energetic particles produce enhanced corrosion at temperatures below the self-diffusion range [52]. At higher dose rates, the oxide growth rate is proportional to the dose rate where the oxide thickness evolves linearly with time following post-transition kinetics [49–51].

While autoclave experiments are the common means to study corrosion, these out-of-pile tests are problematic because irradiation effects are missing, the corrosion rate is low, and the testing is time consuming [50]. Ex-situ tests have been proposed because of limited irradiated materials; these experiments are split into the following environments: 1) exposing pre-irradiated

Zircaloy-2 to high temperature water and 2) exposing pre-corroded Zircaloy-2 to radiation [53]. However, the nuclear reactor conditions have been not replicated by the ex-situ tests [53]. In-situ tests have been performed with proton irradiation because of the higher cost and time constraints from neutron irradiation; at temperatures above 310℃, proton irradiation mimics neutron irradiation at 288℃-300℃ [50, 54]. The experiments needed a 1.7 MV Tandetron accelerator with the capacity to generate proton energies at 3.4 MeV, and deionized water at a constant temperature of 320℃ [50].

To simulate the accelerated corrosion described from the in-situ experiments, radiation enhanced diffusion needs to be taken into account for solid state diffusion models. Previous models such as the linear defect formulation enhanced diffusion can be utilized as the lower bound approximation for the University of Michigan experimental data [52]. Averback and Hahn devised a quadratic power law model, but are not consistent with the Michigan data due to a missing intercept term and different units [55]. A phenomenological version quadratic power law model with matching units needs to be formulated to provide an upper bound on the experimental data.

In the fourth chapter of this dissertation, I focus on the zirconium cladding hydriding assuming synergistic effects from hydrogen on oxygen transport and reaction. The hydrogen transport process also follows the same hydrolysis reaction and diffusion mechanism as the corrosion process. The key difference is that the hydrogen pickup from the hydrogen not reduced by the electrons is formed via the reaction of the oxygen anions and the zirconium cation vacancies. At high temperatures (greater than 1073 K), the unreduced hydrogen is absorbed in the oxide layer to diffuse to the metal in the gaseous state inside an overheated and degraded reactor core; this condition increases the risk of hydrogen detonation [56, 57]. One type of detonation occurs during loss of coolant accident (LOCA) when the cladding attains plastic

deformation and burst due to a pressure gradient in the fuel rod [56]. Another type of accident condition is reactivity initiated accident (RIA) where the increased cladding reactivity results in a rapid rise in temperature followed by a "sudden discharge of fission gas" [56]. Both types of hydrogen detonations result in cladding embrittlement and failure; however, these conditions are rare [56].

Under temperatures between 600 K and 660 K, the common means for degradation is hydride embrittlement. The process begins when hydrogen atoms not reduced by electrons at the oxide-metal interface diffuse from the oxide layer to the metal in the form of protons [6, 58]. A high hydrogen pickup fraction, which is the ratio of hydrogen absorbed by the oxide to the protons generated by the reduction reaction, could result in δ-hydride precipitates in the zirconium metal matrix; this hydrogen fraction varies with oxide thickness as a power law [6]. After absorption in the oxide layer, the hydrides form through a circumferential or radial elongation normal to the uniaxial tensile stress generated by the increased uniaxial anisotropic strain field [11, 59, 60]. Delayed hydride cracking begins when the hydrogen accumulates in the direction of the tensile strain around the crack tip which results in embrittlement [59]. Due to stoichiometric zirconium hydride's "instability with respect to any tetragonal distortion", the increased stress and hydrogen flux in front of the crack activates crack propagation [59–61]. As shown in Figure 1-2, a phase coexistence of α-Zr metal and δ-ZrH is prevalent at 600 K [62].

The hydride formation and fracture is dependent on terminal solid solubility for precipitation/dissolution (TSSP/TSSD). Given an Arrhenius velocity relationship as shown in Figure 1-3, TSSD occurs between 593 K and 793 K (depicted as T3), once the temperature reaches the range of 513 K to 715 K, the hydrogen concentration at the crack tip exceeds the TSSP (depicted as T5); thus hydride formation and crack re-initialization (depicted as T4) occur because the tensile stress lowers the crack energy barrier allowing for increased accumulation

[60, 63, 64]. Once the hydrides attain a critical size, the stress concentration factor (K_I) eventually exceeds the hydride fracture toughness (K_{IH}); consequently, fracture and crack

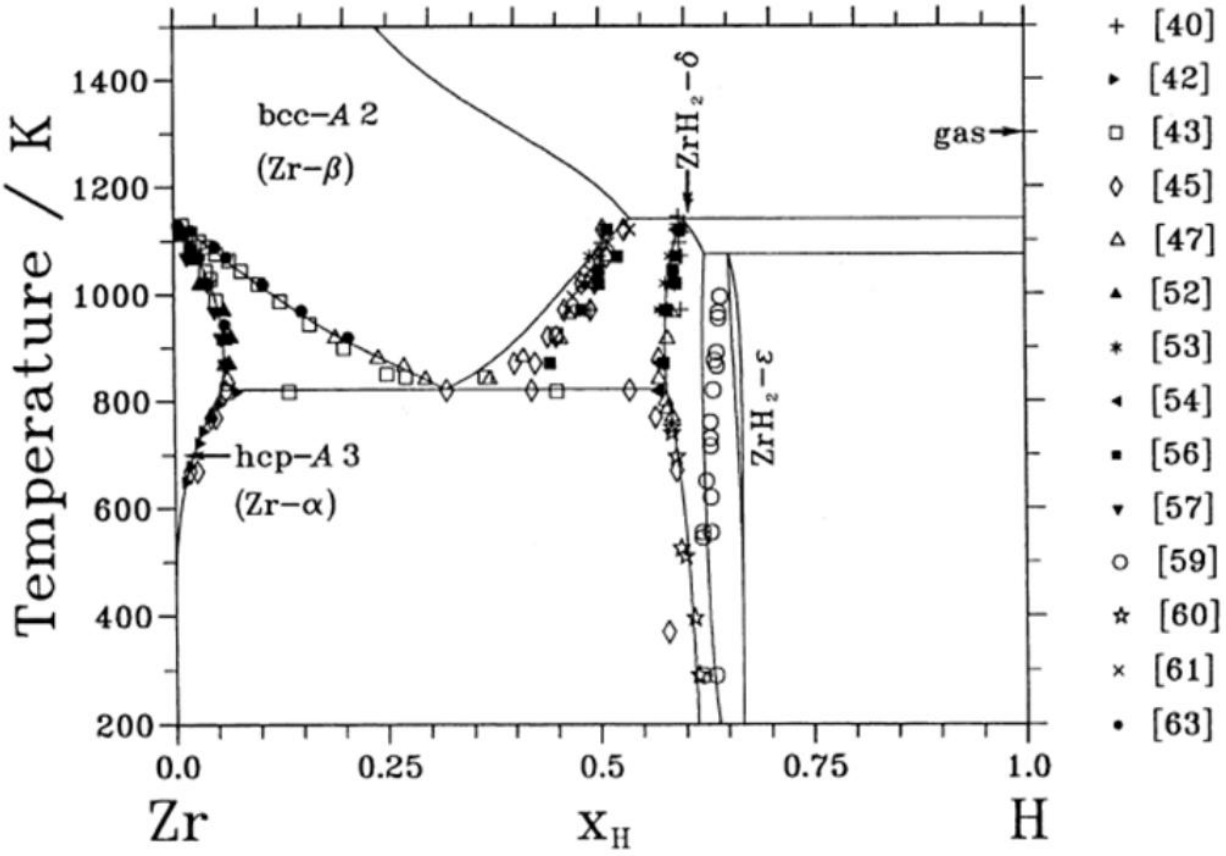

Figure 1-2: Phase diagram for the zirconium hydride system [62]

propagation of the cladding initiate [60, 61, 65]. Prior to attaining post-transition oxide growth (spallation) conditions, the hydride blisters become more lenticular which indicate that the embrittlement generated by the hoop stress precedes the breakaway conditions [56]. As a result, the hydride disrupts the oxide formation of the metal-oxide interface thereby lowering the corrosion resistance of the zirconium cladding [66].

Another important parameter for hydride nucleation is the oxide's ability to be a hydrogen diffusion barrier. At temperatures below 573 K, the oxide layer forms bonds with the

hydrogen ions thereby impeding any diffusion [56, 67]. This restriction in hydrogen accumulation acts as a protective barrier against any tensile stresses that could initiate cracking; in addition, the oxide layer can also inhibit hydrogen from desorbing away from the hydride [56, 67]. At 600 K to 660 K, the O-H bonds dissociate thereby increasing the hydrogen absorption [56, 67].

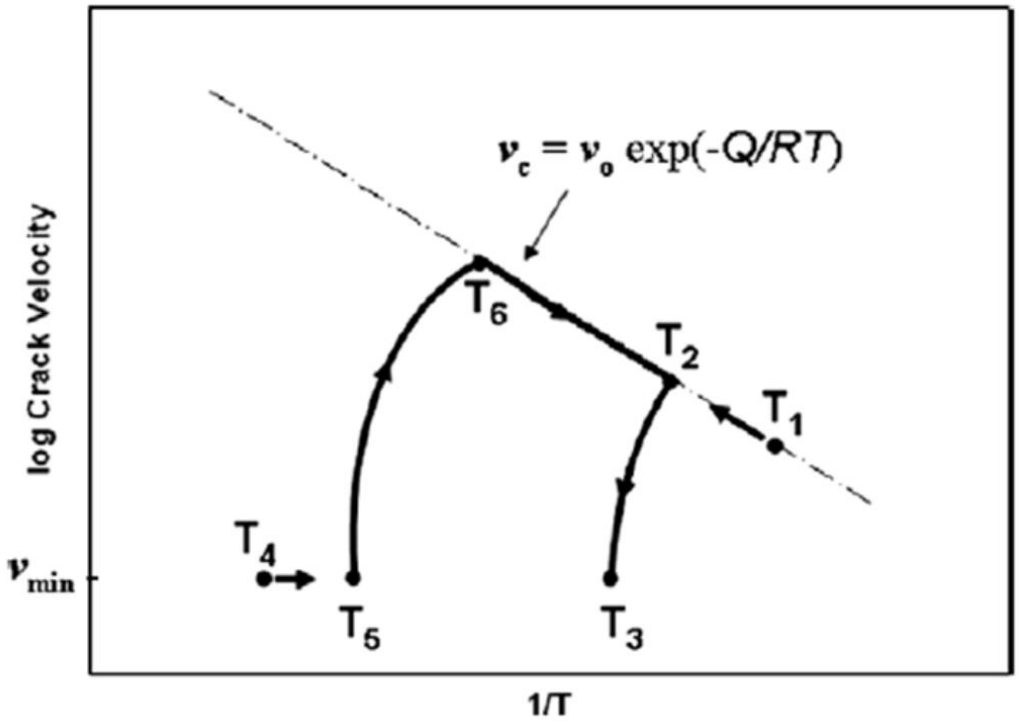

Figure 1-3: Delayed hydride cracking diagram describing the effect of the Arrhenius velocity as a function of temperature. T1 represents the initial heated temperature, while T2 and T6 represent the hysteresis temperatures. T5 is the temperature of terminal solid solubility for precipitation while T3 is temperature of the terminal solid solubility for dissolution. Crack re-initiation occurs at T4. [60].

Since in-pile tests would not be practical due to a scarcity of hydride data, autoclave experiments with variable enhancement methods are typically used to simulate hydride formation in LWR [68]. Gardd has supplemented the autoclave experiments with hydrogen gas treatment for hydriding and impulse furnace heating for providing the thermal gradient to replicate the hydride formation and fracture at the oxide-metal interface [66]. Other methods include the utilization of in situ TEM (transmission electron microscopy) at room temperature to

observe hydride formation during hydrogen ion implantation because of the low solubility of the proton; a model has been developed to validate the observation hydride formation at the crack tip [68, 69]. Zanellato et al. utilized an out-of-pile method that has investigated the dynamic trends of hydride dissolution and precipitation via High-energy synchrotron X-ray diffraction at around 400℃ which can provide higher resolutions and fast flux to successfully predict the TSSP and TSSD [64].

To simulate the hydride precipitation using first principles, previous models have used hydrogen diffusion equations involving at least a concentration gradient at constant temperature to be consistent for autoclave experiments [69, 70]. Shi and Puls have developed a hydrogen diffusion equation dependent on the concentration and stress gradients to emulate hydriding and delayed hydride cracking, but the stress gradient are more essential to model delayed hydride cracking instead of hydride formation [61]. Other models include a thermal gradient or phenomenologically derived drift terms for solid state diffusion equations which are not valid for out-of-pile simulations [60, 63, 71]. All of the previous approximations only account for hydrogen diffusion in the metal thus ignoring the proton diffusion in the oxide layer [60, 61, 63, 69–71]. To obtain a better approximation for the hydrogen diffusion in the oxide, the input of the oxide length generated and the hydrogen diffusivities are necessary. In addition to the inputs, hydrogen diffusion in the oxide needs flux boundary condition instead of constant concentration boundary conditions because the hydrogen concentration at the oxide-metal interface is variable due to the increased hydrogen pickup as a function of oxide thickness [6]. For incorporating hydrogen resorption, Hu et al. [70] and Terrani et al. [72] proposed models that are valid for temperatures around 1033K (gaseous hydrogen) which is out of the range of the TSSP.

Even though my models do not capture their effects, a brief discussion on corrosion products is necessary to better understand corrosion behavior. These corrosion products, also

known as CRUD (Chalk River Unidentified Deposits), act as a thermal barrier because heat transfer is inhibited when they deposit on surfaces neighboring the cladding [11, 14, 73, 74]. In addition, these particles can enhance the corrosion kinetics because of the "harboring and concentrating of aggressive chemicals" [75]. Their transport begins when CRUD particles deposit in the reactor core once the coolant passes through; next the corrosion products become irradiated and dissolves in the coolant inside the core [14]. Then the dissolved particles exit the reactor core and form their own radioactive oxide layer [14]. As the temperature decreases, the corrosion products precipitate, and the process starts again [14].

The inner most CRUD deposits comprise of iron oxides, aluminum oxides, nickel oxides, chromates, sulfates, phosphates, silicates; these particles are mainly responsible for the heat transfer inhibition [13, 14, 73–76]. The outermost corrosion product deposits, which are comprised of cobalt and boron-10, are both high neutron absorbers and can produce deleterious effects on the cladding [8, 13, 73]. Boron-10 particles, derived from lithium metaborate ($LiBO_2$), nickel–boroferrite (Ni_2FeBO_5) and Boric Acid (H_3BO_3), can cause a large depression of the neutron flux in the top half of the reactor core at "sub-cooled nucleate boiling conditions" in boiling water reactors (BWR) [76, 77]. This phenomenon, known as axial offset anomaly (AOA), is caused by boron's high neutron capture; this is not a factor in pressurized water reactors (PWR) since boiling temperatures newer attain sub-cooled nucleate boiling conditions [76, 77]. Similar to boron-10, cobalt-59 also has a large neutron cross section; however, cobalt-60, the transmutation of cobalt-59 after neutron absorption, has a decreased neutron capture cross section of its predecessor [14, 73, 74]. Even though AOA is uncommon in cobalt, spalling and erosion are its primary means of degradation [73]. The mechanism of spalling and erosion is by means of "hydrodynamic action" on the cladding surface where the coolant velocity creates a shear stress accumulation on the affected surface [73].

Another topic not included in my simulations that need some discussion is the coolant chemistry's influence in the corrosion of the zirconium clad. The coolant contains lithium hydroxide (LiOH) to "reduce fuel cycle costs and plant radiation levels" as well as "increase coolant pH and inlet temperatures"; the overall purpose is to increase the reactor's efficiency [78]. However, LiOH concentrates at the pores or cracks in the water/oxide interface and reacts with the zirconia layer to even form new oxides [78, 79]. At critical lithium concentration levels (between 0.1 and l M), the zirconia dissolves locally, and the pores enlarge creating new crystalline boundaries within the oxide film; thus the corrosion rate is enhanced [17, 79]. During post-transition, corrosion rate continues to increase, and the lithium ions have access to oxide/metal interface [79]. To moderate the effects of coolant chemistry in the corrosion kinetics, boric acid has been included in the coolant to react with lithium ions to generate lithium borate; this reaction results in lower pH levels, decreased oxide dissolution and limited interactions with zirconia [79]. Adding boric acid slows down the Stage 2 transition because the boron competes with the monoclinic zirconia for reacting with the lithium ions [79]. However, high lithium hydroxide concentrations can induce crud formation due to elevated lithium borate resulting in large neutron capture at sub-cooled boiling conditions for BWRs only; this type of Axial Offset Anomaly is called Crud Induced Power Shift (CIPS) [78, 80].

As a means to provide new computational and experimental understanding of corrosion, hydriding and irradiation effects, I present three separate comprehensive models for the following phenomena: 1) oxidation model of Zr formulated from first principles reaction kinetics and fundamental thermodynamics and mechanics assuming no coupling to hydriding and irradiation, 2) oxidation model incorporating the effects of radiation enhanced corrosion kinetics, and 3) numerical model predicting hydride formation coupled with oxidation assuming no irradiation. The parameterization of the oxidation model uses oxygen electronic structure

calculations and experiments; the kinetics of the protective oxide layer growth and post-transition growth after oxide scale fragmentation are also captured. In addition, the irradiation model uses parameters based on the University of Michigan's experimental conditions and data, and oxide scale growth from the oxidation model. Furthermore, the hydriding model is parameterized using the solubility limit, hydrogen diffusivities, the oxide layer growth data generated from the oxidation model, hydrogen flux boundary conditions in the oxide, and hydride desorption calculations. As a note, all models assume no effects from crud formation and water chemistry.

The second chapter of this dissertation commences on the description on the fundamental chemistry and phenomenology of the oxidation process followed by a mathematical formulation of the model. After obtaining the equation, numerical results under based on conditions relevant to LWR operation are provided. This chapter finalizes with discussions on the results and the implications of the modeling approach for zircaloy corrosion. After discussing the concept of radiation enhanced diffusion, the third chapter describes its application to the model's mathematical formulation. Similar to the other sections, this chapter includes numerical data from the model's calculation under different irradiation dose (damage) rate, the discussion of the results, and possible implications these results can provide with the inclusion of irradiation effects. The fourth chapter begins with the basic concepts chemistry, and mathematical formulation of hydride kinetics. After providing numerical data from the model's calculation of hydrogen diffusion as well as hydride formation conditions, I conclude with the discussion of the results and what significance these results can provide with the effects of hydrogen pickup and degradation.

2. Chapter 2: Multilayer Oxidation

2.1. Chemical reaction kinetics model

2.1.1. Chemistry of low-temperature Zr oxide reaction

The corrosion of Zr begins with an electrochemical process defined by the hydrolysis reaction

$$2H_2O + 4e^- \rightarrow 2O^{2-} + 2H_2 \quad (1)$$

and followed by the oxidation reaction

$$Zr + 2O^{2-} + 2V_{ZrO_2}^{O} \rightarrow ZrO_2 + 4e^- \quad (2)$$

which lead to the combine stoichiometric reaction:

$$Zr + 2H_2O \rightarrow ZrO_2 + 2H_2 \quad (3)$$

with $V_{ZrO_2}^{O}$ denotes the oxide vacancy in ZrO_2. In the above reaction, hydrogen is chosen to be written in terms of molecular hydrogen H_2. However, some of the hydrogen can remain as atomic hydrogen if they remain dissolved in water or penetrate the solid clad and contribute to hydride nucleation. Reaction (3) represents an ideal stoichiometric reaction of stable chemical species. However, reaction (3) can be incomplete to form nonstoichiometric ZrO_{2-x} if there exists conditions of impoverished oxygen concentrations such as near the oxide/metal interface. It is generally assumed that a negligible range of non stoichiometric oxide is admitted by the monoclinic α-ZrO_2 phase although they are undetectable by conventional techniques [81]. Conversely, concentration limit of the sub-stoichiometric tetragonal β-ZrO_{2-x} phase at $x < 0.02$ is determined by means of metallography [82] and mass spectroscopy [83] measurements. The coexistence of the monoclinic and sub-stoichiometric phases may be behind the stabilization of tetragonal zirconia (which at ambient pressure occurs only above 1200 K, cf. refs. [81,84]) near

the interface. As well, nonstoichiometry may be a factor in the formation of a local charge imbalance at the oxide/metal interface, as will be discussed below.

An agreement exists between experimental [81] as well as computational [84] descriptions of the phase diagram below 1200K and the first compounds that appear after the metal solid solution phase (α-Zr); these phases are ordered ZrOz hexagonal metallic compounds –also termed 'suboxides'– with stoichiometries ranging from z = 1/6 to z = 1/2 (which are often designated by descriptors such as α_2'', α_3'', or α′ [81]). The experimental data become inconclusive as to the expected phases at stoichiometries above 1/2. However, recent findings from density functional theory (DFT) calculations imply the coexistence of a line compound with perfect stoichiometry ZrO (z = 1) with phases ranging from metallic α′ phase ($ZrO_{1/2}$) up to the monoclinic zirconia phase boundary (α-ZrO_2), which starts to nucleate at 1/2 oxygen atomic fraction [84]. Similar to α-TiO, the ZrO phase, also known as δ′, forms in a distorted simple hexagonal crystal lattice. From recent experimental measurements in several Zr-based systems, the δ′ phase (as well as $ZrO_{1/2}$) forms behind the zirconia layer in specimens exposed to 360 °C water [85–87].

To be consistent with the most recent experimental evidence, the model comprises of three consecutive layers (α-ZrO_2)-(δ′ - ZrO)-(α-Zr) separated by two distinct interfaces evolving in time according to chemical, thermal, and mechanical constraints. In the following, only to the α-ZrO_2 layer is referred to the word 'oxide'.

2.1.2. Qualitative picture of the structural growth of zirconia films

Once oxygen ions become available from the reduction of water at the clad outer surface, they penetrate in the Zr matrix via diffusion against a temperature gradient of approximately 60K over 600 μm under in-pile conditions [88]; this results in oxygen transport acceleration as it

penetrates the clad. The resulting Zr-O mixtures evolve through the different phases discussed above with increasing oxygen concentration. A well-defined interface, which separates the ZrO from the region containing the metal and other suboxides, appears when the O to Zr atoms ratio reaches a proportion of 1:1 corresponding to the δ′-ZrO phase; however it is unclear that the ZrO layer can be considered a barrier layer. A second interface separating the newly formed oxide phase from the δ′ phase appears as the atomic fraction of oxygen approaches 2/3. However, the first oxide phase to emerge is a tetragonal β-ZrO_{2-x} because the monoclinic ZrO_2 phase that is expected to form at low temperatures does not form under sub-stoichiometric conditions. The compressive stresses that develop between the α-Zr matrix opposing the transformation to the less dense monoclinic form is believed to stabilize the tetragonal phase at low temperatures [89, 90]. Due to lower surface energies compared with the monoclinic form, keeping the oxide particle size at less than approximately 30nm aids the stability of the tetragonal phase [91, 92].

The oxide that starts to form are comprised of arrays of ZrO_{2-x} nano-crystals that contains many different orientations relative to the orientation of the Zr grain on which they form; the crystals are equiaxed at in-pile conditions [38] while they are columnar at out-of-pile conditions [88]. As previously discussed, tetragonal zirconia is the initial internal structure of these crystallites [6, 88]; although their crystallographic orientation is very difficult to establish, these crystallites is expected to grow with orientations minimizing the stress resulting from the volume change on transforming from Zr to zirconia (the Pilling-Bedworth ratio of 1.56). The Pilling-Bedworth ratio is defined as

$$PRB = \frac{V_{ZrO_2}}{V_{Zr}} = \frac{\rho_{Zr}}{\rho_{ZrO_2}} = 1.56$$ where V is the molar volume and ρ the atomic density.

Based on a recent work, the oxide is comprised of well-oriented columnar monoclinic grains aligned with ⟨001⟩ directions parallel to the metal/oxide interface; in addition, some of the oxide

consists of sporadic tetragonal grains interspersed throughout the oxide with orientations significantly different from the ⟨001⟩ orientation [93]. Since oxygen transport is accelerated with respect to bulk diffusion, free oxygen diffusion is believed to occur preferentially occur along the grain boundaries of these oxide crystallites within the ZrO_{2-x} layer. The oxide scale thickness under these conditions grows as $t^{1/2}$ as described by weight loss experiments [41, 88, 94, 95].

The stoichiometric oxide concentration is first reached near the coolant side as the oxygen ions continue to penetrate the clad causing the oxide crystals to commence their transformation into a more stable monoclinic phase. This conversion of tetragonal → monoclinic zirconia is martensitic and generates microcracks in the oxide due to the volume expansion associated with the phase change; residual stresses developed during the metal-to-oxide transformation compounds these microcracks and eventually shear cracking [6, 93, 96, 97]. In parallel, oxide porosity is developed in the layer since Zr cation vacancy is absorbed by grain boundaries; the weakened bonds of the grains cause them to transform from columnar to equiaxed [6, 98]. Although the mechanisms of the kinetics are not fully understood, the oxide transitions to a $t^{1/3}$ growth dependence (at least under PWR operating temperatures [6, 11, 18, 88, 94, 99]) as it thickens. Stage 2 kinetics commences due to further oxide growth resulting in the eventual activation of cracks to the neutral stress axis in the oxide [17]. Therefore, it is expected for a tetragonal zirconium oxide layer to exist adjacent to the oxide/ZrO (or metal) interface comprising of a less than stoichiometric free oxygen concentration; however these crystallites transform to monoclinic zirconia at the oxide/water interface with an intrinsic distribution of cracks. The shear cracking causes an interlinkage in the porosity from the ZrO/metal interface to the oxide/coolant interface allowing the coolant to access the ZrO/metal interface [6, 98]. The coexistence of the two allotropes of ZrO_2 has been modeled in a previous study [100]. In this

work, however, no distinction between sub-stoichiometric tetragonal zirconia and monoclinic zirconia exists, which bundles them into a single 'oxide' layer.

2.1.3. Oxidation Kinetic Model

A Stefan model is necessary to predict the evolution of the oxide growth with moving boundaries [101]. Solving moving boundary conditions involving mass and heat transport have utilized the Stefan formulation [101–103]. As described in Figure 2-1, oxygen flux discontinuities are generated by the diffusion from distinct layers, represented by ZrO_2, ZrO, and α-Zr (and its suboxides) respectively, which result in variable interfaces moving as a consequence of oxygen flux. From geometric definition in Figure 2-1, the model needs to define the following two evolution equations for two distinct layers where the first represents the ZrO_2/ZrO interface (s_1) and the second represents the ZrO/metal interface (s_2):

$$\dot{s}_1 = \frac{\mathrm{J_{III}}}{2\rho_{\mathrm{Zr}}} = -\frac{\mathrm{D_{III}}}{2\rho_{\mathrm{Zr}}}\frac{\partial c_{III}}{\partial y} \tag{4}$$

$$\dot{s}_2 = \frac{\mathrm{J_{II}}}{\rho_{\mathrm{Zr}}} = -\frac{\mathrm{D_{II}}}{\rho_{\mathrm{Zr}}}\frac{\partial c_{II}}{\partial y} \tag{5}$$

where roman numeral II represents the ZrO layer and III represents the ZrO_2 layer. J_{II} and J_{III} are the mass fluxes, D_{II} and D_{III} are for the diffusivities, c_{II} and c_{III} are the concentrations, and ρ_{Zr} is the atomic density of zirconium.

The flux terms are obtained by solving the drift-diffusion equation below:

$$\frac{\partial c_i}{\partial t} = \nabla(\mathrm{D_i}\nabla c_i) + \frac{\mathrm{U_i D_i}}{\mathrm{kT^2}}\nabla c_i \nabla T + \frac{\mathrm{q_i D_i}}{\mathrm{kT}}\nabla(c_i \nabla \phi) \tag{6}$$

where i = I (metal layer), II (ZrO layer), III (ZrO_2 layer) [104]. The first term of the right hand side of eq. (6) signifies the Fickian diffusion in the presence of a concentration gradient. The

second term represents the thermo-migration in response to a thermal gradient; U_i is the diffusion activation energy, k is the Boltzmann constant, and T is the temperature.

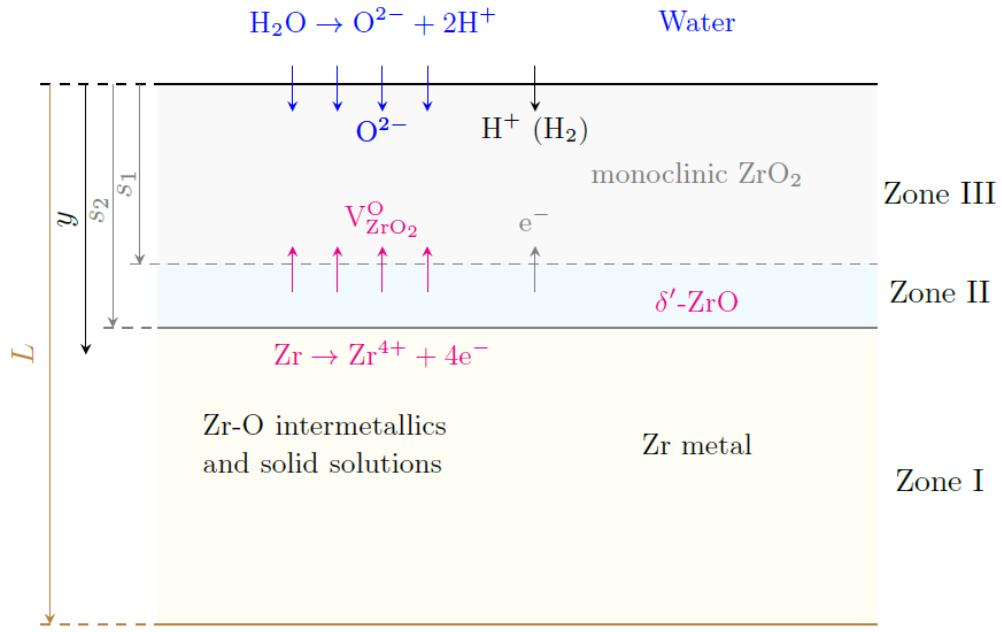

Figure 2-1: Schematic diagram (not to scale) of the moving boundary described in the corrosion model developed in this dissertation. y is the depth variable, s_1 is the position of the ZrO_2/ZrO interface, s_2 is the position of the ZrO/metal interface, and L is the total thickness of the clad.

According to the thermomigration theory known as Soret-Ludwig effect, substitutional atoms are expected to move down the temperature gradient via vacancies, while the motion of interstitial solutes is against the temperature gradient. An interstitial diffusion mechanism has been suggested by evidence of oxygen diffusion in α-Zr down the temperature gradient through experimental and mathematical means [105,106]. According to convention, thermomigration down a thermal gradient is declared 'positive', making the term additive in the equation. The third term is the electro-migration term where q_i is the particle's charge, and ϕ is the electric potential which can be calculated through Poisson's equation shown below:

$$\nabla^2\phi = -\frac{\rho}{\varepsilon} \tag{7}$$

where ρ is the charge density and ε is the permittivity.

As discussed in Section 2.1.1, variable oxide configurations ranging from a solid solution to various subsaturated intermetallic phases begin to form as oxygen builds up in the metal. These phases dissolve and remove oxygen from the free oxygen concentration thereby causing its immobilization. The chemistry and kinetics in each layer determine the relevance of each term in eq. (6), which is discussed in the next section.

2.1.3.1. Zone I: Zr-O solid solution formation

A Zr-O solid solution is formed when the free oxygen penetrates into the clad. According to the zirconium-oxygen phase diagram [84], the oxygen solubility is around 20% at temperatures between 600 K and 660 K. Drift due to electro-migration is neglected since the local charge equilibrium is assumed in the metallic layer. However, thermo-migration activates due to the existence of a temperature gradient. The resulting equation is:

$$\frac{\partial c_I}{\partial t} = \mathrm{D_I}\left(\frac{\partial^2 c_I}{\partial y^2} + \frac{\mathrm{U_I}}{\mathrm{kT^2}}\frac{\partial c_I}{\partial y}\frac{\partial T}{\partial y}\Big|_I\right) \tag{8}$$

where $\mathrm{D_I} = \mathrm{D_o}\exp\left(-\frac{\mathrm{U_I}}{\mathrm{kT}}\right)$ is the oxygen diffusivity in α-Zr, assumed to be independent of the oxygen content.

2.1.3.2. Zone II: diffusional growth of the δ′ suboxide

The first line compound appears with the formation of the δ′ phase corresponding to an atomic fraction of 0.5. Since they are considered saturated phases, line compounds can no longer immobilize oxygen. Therefore a distinct ZrO layer forms with a fixed composition; a plateau in the measured oxygen concentration at 50% from atom probe tomography experiments shows

evidence of this layer formation [45–47]. Assuming charge equilibrium, the mass balance equation reads:

$$\frac{\partial c_{II}}{\partial t} = \mathrm{D_{II}}\left(\frac{\partial^2 c_{II}}{\partial y^2} + \frac{\mathrm{U_{II}}}{\mathrm{kT^2}}\frac{\partial c_{II}}{\partial y}\frac{\partial T}{\partial y}\Big|_{II}\right) \quad (9)$$

where $\mathrm{D_{II}}$ is the oxygen diffusivity in ZrO.

2.1.3.3. Zone III: oxide scale growth

Similar to zone II, the oxygen flux imbalance at the ZrO/ZrO_2 interface drives the growth of zone III (referred to as oxide scale hereafter). Nevertheless, the electric field created by charged species gradients, including oxygen anions and electrons needs to be accounted for to provide completeness of the model. Therefore, the complete equation is used for this layer:

$$\frac{\partial c_{III}}{\partial t} = \mathrm{D_{III}}\left[\frac{\partial^2 c_{III}}{\partial y^2} + \frac{\mathrm{U_{III}}}{\mathrm{kT^2}}\frac{\partial c_{III}}{\partial y}\frac{\partial T}{\partial y}\Big|_{III} + \frac{\mathrm{q}}{\mathrm{kT}}\left(\frac{\partial c_{III}}{\partial y}\frac{\partial \phi}{\partial y} + c_{III}\frac{\partial^2 c_{III}}{\partial y^2}\right)\right] \quad (10)$$

where $\mathrm{D_{III}}$ is the oxygen diffusivity in the oxide.

Although several studies utilizes the concept of a concentration gradient to explain non-parabolic growth in corroded Zr, experiments, per Couet et al. [107], have not firmly established the existence of an oxygen concentration gradient across the oxide [35, 108]. Kinetic models were developed by Couet et al. to ensure a zero charge current condition derived from a charge balance between the anionic and cationic mass flows [107]. If the oxygen ions are the only charged species moving, electron current needs to flow in the opposite direction to achieve charge balance [17]. Since the Zirconium cation vacancies are virtually immobile and hydrogen pickup occurs, excess oxygen vacancies from tetragonal zirconia formation can cause a local charge imbalance [17, 107]. Other sources of charge imbalances include positive charges from zircaloy and zirconium-niobium alloys restricting electron transport, and the lithium and

hydroxide ions generated from the coolant [98, 107]. Based on Beie et al's [109] measurements of the voltage difference between the metal and the oxide surfaces in non-stoichiometric ZrO_{2-x}, a simpler model using an exponentially decaying charge density distribution concentrated near the interface with the ZrO layer has been adopted:

$$\rho(y) = \rho_0 \cdot exp\left(-\frac{s_1 - y}{\lambda}\right) \tag{11}$$

where λ is a spatial constant and ρ_0 is that charge density at the interface. As discussed by Bell et al., this expression for the charge density has been justified since the presence of a thin non-stoichiometric ZrO_{2-x} layer and high compressive stresses can result in extra oxygen vacancies that can trap electrons and create a charge gradient [110, 111]. Equation (11) is simple to integrate from a numerical point of view, which can write the electrical potential and its first derivative as:

$$\phi(y) = -\frac{\lambda^2 \rho(y)}{\varepsilon}\ ,\ \nabla\phi(y) = -\frac{\lambda\rho(y)}{\varepsilon}$$

During Stage 1 growth, the finite difference model is used to solve equations (8)–(10) in one dimension (y) using subjected to the following dynamic boundary conditions:

$$c_I(y, 0) = 0, y > s_2$$

$$c_I(s_2, t) = c_{II}(s_2, t) + \rho_{Zr}$$

$$c_{II}(s_1, t) = c_{III}(s_1, t) + 2\rho_{Zr}$$

$$c_{III}(0, t) = C_0$$

$$\frac{\partial c_I(L,t)}{dy} = 0$$

where C_0 is the constant oxygen concentration available at the cladding/coolant interface. The first condition trivially states that the oxygen content in the clad is initially zero. The next two ensure the oxygen concentration to be continuous at the interfaces while the fourth sets the oxygen concentration in the environment based on values generated by the water chemistry, temperature, pressure, etc. Finally, the last one ensures that no free oxygen can escape the clad into the fuel side, i.e. $J_I(L,t) = 0$, where J_I is the free oxygen flux in the metal.

As the oxide layer grows, an increasing volume differential with respect to the Zr metal creates microcracks developed in the oxide scale. As tetragonal phase transforms into the monoclinic one, an additional expansion of ~3% occurs at 0 K, as given by their respective specific volumes of 0.139 and 0.143nm; these specific volumes are defined as:

$$V_t = a_t^2 c_t \; ; \; V_m = a_m b_m c_m \sin\beta$$

where a_t= 0.514 nm, c_t = 0.526 nm, a_m= 0.518 nm, b_m= 0.521 nm, c_m= 0.537 nm and β = 98.8º [112]. Eventually, fragmentation of the oxide scale commences after these in-grown cracks form a network, giving rise to Stage 2 growth.

2.1.4. Stage 2: ZrO_2 layer breakaway growth

Due to free oxygen diffusion through the microcrack network, Stage 2 growth is assumed to have free oxygen from the environment side to become available immediately on the ZrO_2/ZrO interface (at $y = s_1$). Since the entire oxide layer is assumed to be monoclinic at the point of spall, the model re-solves the mass balance system of equations for the metal phase by using a new boundary condition ($c_{II}(s_1,t) = C_0$) for the oxygen concentration in the oxide metal interface. As the oxide layer grows thicker during Stage 2, the oxygen concentration is assumed

to maintain a fixed concentration of C_0 at the interface while the cracks grow. Breakaway behavior is a result of readily available free oxygen that accelerates oxide layer growth.

In terms of the model, the drift-diffusion equation for Zone III no longer needs to be solved. Instead, only eqs. (9) and (10) need be considered with the updated dynamic boundary condition:

$$c_{II}(s_1, t > t_{1\to2}) = C_0$$

where $t_{1\to2}$ is the transition time for the occurrence of Stage 2. Equation (4) becomes:

$$\dot{s}_1 = \frac{C_0 v}{2\rho_{Zr}} \tag{12}$$

where v is the viscous flow velocity of water through the crack network. Again, it is noted that the model assumes the parameters for pure Zr, which is known to experience breakaway conditions at a thickness less than two microns. However, the oxide scale in more advanced Zr alloys does not break down in the same manner as pure Zr but instead reconstitutes cyclically. In chapters 3 and 4, the model assumes the parameters for zircaloy-4.

2.1.5. Temperature gradient calculation

Based on eqs. (8) – (10), the thermo-migration variables, T(y) and $\frac{dT}{dy}$, are essential inputs to the kinetic model. The definition of the temperature field at every (y,t) point of the finite difference mesh is required to calculate the temperature gradients. For this, the model assumes a constant heat flux flowing through the cladding from the fuel side to the coolant side under steady state reactor operation. Assuming a linear, one-dimensional temperature gradient, the heat

flux q_0 at t = 0 can be obtained from Fourier's law:

$$q_0 = -\kappa_I \frac{dT}{dy} = \kappa_I \frac{T_c^0 - T_L^0}{L} \quad (13)$$

where κ_I is the thermal conductivity of the Zr metal (zone I), T_c^0 is the initial temperature at the outer position of the clad, and T_L^0 is the initial temperatures at the inner position of the clad. It is further assumed that T_c is constant (same as the coolant temperature) as a function of time, while the inner temperature T_L is variable as the cladding oxidizes and the overall thermal conductivity changes. As the oxide and suboxide layers grow, the temperature gradients for each layer are obtained from the following conservation law:

$$q_0 = \kappa_I \frac{T_L - T_2}{L - s_2} = \kappa_{II} \frac{T_2 - T_1}{s_2 - s_1} = \kappa_{III} \frac{T_1 - T_c^0}{s_1} \quad (14)$$

where κ_{II} and κ_{III} are the thermal conductivities for ZrO and ZrO_2, and T_1 and T_2 are the temperatures at the ZrO_2/ZrO (s_1) and ZrO/Zr (s_2) interfaces, respectively. The combination of eqs. (13) and (14) yield:

$$T_1 = T_c^0 + \frac{q_0 s_1}{\kappa_{III}} \quad (15)$$

$$T_2 = T_1 + \frac{q_0 (s_2 - s_1)}{\kappa_{II}} \quad (16)$$

$$T_L = T_2 + \frac{q_0 (L - s_2)}{\kappa_I} \quad (17)$$

where an update of each temperature fields via the thickness variables $s_1(t)$ and $s_2(t)$ allows for the calculation of all thermal gradients.

Equations (15) and (16) show that the interface temperatures T_1 and T_2 are proportional to the thickness of the ZrO_2 and ZrO layers, respectively. Equation (17) shows that T_L rises even though s_2 and the second term on the r.h.s. are inversely proportional.

The model assumes that the energy balance due to the enthalpy phase is insignificant for the overall thermal approximation. For this to be true, the heat flux due to the enthalpy of formation of the oxide must be significantly smaller than the heat flux from the reactor core. Chase [168] has listed the enthalpy of formation for zirconium dioxide as 1097.46 KJ·mol^{-1}. Using the equation $q_H = \Delta H \cdot \dot{s}_1$, the heat flux do to enthalpy of formation is 896 W·m^{-2} which is much lower than the heat flux of the reactor core from eq. (13) (q_0 = 1.917x10^6 W·m^{-2}).

2.1.6. Determining the Stage 1 to Stage 2 transition time

2.1.6.1. Stress buildup

Thermal and compressive stresses due to growth are the main sources of stress during the oxide layer growth. Differential thermal expansion between the oxide and metal layers generates the thermal stresses. A biaxial stress state is assumed where the hoop stress and the axial stress are equal ($\sigma_\theta = \sigma_z$ in cylindrical coordinates). At this state, the metallic substrate can be much thicker than the oxide phase; thus the hoop stress in the oxide scale is:

$$\sigma_\theta^{th} = \frac{E_{ox}}{1-\nu_{ox}} \int_{T_1}^{T_c^0} \Delta\alpha(T)\,dT \tag{18}$$

where E_{ox} is the Young's modulus, ν_{ox} is the Poisson's ratio of the oxide. $\Delta\alpha(T)$ is the differential thermal expansion:

$$\Delta\alpha(T) = \alpha_{ox}(T) - \alpha_m(T)$$

where $\alpha_{ox}(T)$ and $\alpha_m(T)$ are the thermal expansion of the oxide and metal, respectively.

The conditions in the oxide scale determine the sign of the thermal stresses. In most cases, metals have much larger thermal expansion coefficients than oxides. For nominal conditions, the metal expands by an amount much larger than the oxide scale at the oxide/metal

interface because the temperature of the metal substrate is higher than the oxide scale. This expansion results in local tensile stresses on the oxide layer.

Cooling the clad to room temperature can cause compressive thermal stresses that can lead to oxide scale failure. However, growth stresses due to internal oxidation are the main source of stresses under operating conditions. Growth stresses are normally in-plane compressive reaching to levels up to few GPa [34, 95, 113]. Following the ideas of Birks et al. is necessary to obtain the magnitude of the growth stresses [40]. The change of specific volume between the consumption of the metallic substrate and the creation of the oxide scale at the oxide/metal interface would produce an inelastic volume eigenstrain. The Pilling-Bedworth ratio (PBR) is the parameter associated with this phenomenon. Given an isotropic oxidation process, the tangential strain due to oxide growth is approximately:

$$\varepsilon_{ox}^{g} = \frac{1}{3}(PBR - 1)$$

The compressive and bi-axial stress due to this strain is as follows:

$$\sigma_{ox}^{g} = -\frac{E_{ox}}{(1-\nu_{ox})}\varepsilon_{ox}^{g} = -\frac{E_{ox}(PBR-1)}{3(1-\nu_{ox})} \quad (19)$$

During the initial stages of oxide formation, the oxide/metal interface is where these stresses develop. Less significant stress generation or deformation occurs for subsequent oxide scale growth since the top of the existing layer accommodates new oxide formation. Thus, compressive and constant growth stresses maintain the oxide near the interface, independent of the oxide scale thickness. Even though the oxide growth is highly anisotropic in reality, the assumptions given by eq. (19) result in an overestimation of the stresses [114]. The next section establishes a criterion to determine the conditions in which the oxide layer growth leads to uniform fragmentation and the loss of the protective layer.

2.1.6.2. Failure criterion

Two means for spalling can occur from compressive stresses. The nucleation and growth of a wedge crack is the first route for spalling which occurs preferentially for strong interfaces and weak oxide scales. Buckling is the second route, which occurs preferentially for weak interfaces and strong oxide scales. At low temperatures, protective oxide layers experiences brittle properties. Hence, Griffith's theory can be applied to calculate $t_{1\rightarrow 2}$ in the temperature range of interest for LWR operation. A stress σ_{ox} can develop a continually growing flaw in the oxide layer if its strain energy release G exceeds the critical energy release rate G^* of the oxide [40, 114]:

$$G_{ox} = \frac{K^2}{E_{ox}} = \frac{{\sigma_\theta}^2 Y^2 \pi a}{E_{ox}} > G^* \; ; K = Y\sigma_\theta\sqrt{\pi a}$$

where K is the stress intensity factor, a is the flaw size, and Y is a geometric parameter whose value becomes closer to unity for a small crack embedded in a two-dimensional solid. A proportional relationship between G^* and the surface energy γ can be formulated, which results in the following criteria for fracture:

$$\frac{{\sigma_\theta}^2 Y^2 \pi a}{E_{ox}} > \gamma \tag{20}$$

Equation (20) states that cracks will form and propagate when the accumulated elastic energy surpasses the surface energy. The flaw size is assumed to increase with oxide scale thickness because it is an unknown quantity in zirconia described by the relation, $a = \varepsilon s_1$, where ε is a proportionality constant set by value of 0.2 [115]. Equation (20) applies to mode I crack growth under tensile stresses even though the actual crack growth occur by vacancy aggregation under compressive stresses via creep rupture [116]. However, the model assumes a mode I crack growth for simplicity which eventually leads to fragmentation across the oxide scale. Cracks can

originate at the ZrO_2/ZrO interface, or during the transformation of the tetragonal to monoclinic phases. Impurities, precipitates, pores, or other cavities can also impact the likelihood of cracking.

Equations (18) and (19) can show that thermal stresses have scaling factors with values of $\sim 10^{-5} \cdot E_{ox}$, whereas growth stresses have scaling factors with values of $\sim 10^{-1} \cdot E_{ox}$. Consequently, the model only considers growth stresses for σ_{ox} going forward. By inserting eq. (19) into eq. (20), the failure criterion is updated as:

$$\frac{E_{ox}(PBR-1)^2 Y^2 \pi \varepsilon s_1}{9(1-\nu_{ox}{}^2)} > \gamma \tag{21}$$

The finalized criterion for the critical oxide scale thickness s^* is furnished at the onset of fragmentation:

$$s_1^* > \frac{9\gamma(1-\nu_{ox}{}^2)}{E_{ox}(PBR-1)^2 Y^2 \pi \varepsilon} \tag{22}$$

Equation (22) is utilized to extract the value of ε assuming s^* to be between the commonly cited values of one and two microns [17, 28, 117, 118]. For the parameters listed in Table 2-1, $\varepsilon \approx 10^{-4}$ is the value obtained, suggesting that small cracks can trigger fragmentation in ZrO_2. Calculating the $s_1(t)$ relation as $s_1(t_{1\to2}) = s^*$ can directly provide the time $t_{1\to2}$.

2.1.7. Procedure for numerical solution

In order to solve coupled PDEs of the above system, the finite difference method requires the discretization of eqs. (8)–(10) in space and time. Here, time and space are partitioned into finite grids as follows:

$t^i = i\delta t\,, i = 1,2,\dots,N$ and $y_j = j\delta y\,, j = 1,2,\dots,M$

where the superscripts are the conventional notation to represent time (t^i) while subscripts represent space (y_j). For uniform grids, δt and δy are:

$\delta t = t/N$ and $\delta y = L/M$

where N and M represent the grid size, and t signifies the total simulated time.

Adopting the Forward Time Central Space (FTCS) scheme where forward differences replace time derivatives, and central differences replace space derivatives, the drift-diffusion equation for the most general case, represented by eq. (10) (Zone III) can be discretized in the following form:

$$\frac{c_j^{i+1} - c_j^i}{\delta t} = D_{III(T_j)}\left[\frac{c_{j+1}^i - 2c_j^i + c_{j-1}^i}{\delta y^2} + \frac{U_{III}}{kT_j^2}\left(\frac{dT}{dy}\right)_{III}^{i}\frac{c_{j+1}^i - c_{j-1}^i}{2\delta y}\right.$$

$$\left. + \frac{q\rho_0\lambda}{2kT_j\varepsilon\delta y}\left\{exp\left(-\frac{s_1^i - y_j^i}{\lambda}\right)\left(c_{j+1}^i - \frac{2\delta y}{\lambda}c_j^i - c_{j-1}^i\right) - c_{j+1}^i + c_{j-1}^i\right\}\right] \quad (23)$$

which can be written in explicit form as:

$$c_j^{i+1} = c_{j+1}^i(1 + a_1 + a_2 + a_3 + a_4) + c_j^i(1 - 2a_1 + a_5) +$$

$$c_{j-1}^i(1 + a_1 + a_2 + a_3 + a_4) \quad (24)$$

with

$$a_1 = \frac{D_{III}\delta t}{\delta y^2} \qquad a_2 = a_1\frac{U_{III}\delta y}{2kT^2}\left(\frac{dT}{dy}\right)_{III} \qquad a_3 = -a_1\frac{q\lambda\rho_0\delta y}{2kT\varepsilon}$$

$$a_4 = -a_3 exp\left(-\frac{s_1 - y}{\lambda}\right) \qquad a_5 = a_3\frac{2\delta y}{\lambda}$$

where eq. (23) evaluates T, y, s1, and s2 at time i and location j. Neumann's analysis is a method to access the numerical stability of the explicit FTCS scheme which, for a purely parabolic

problem is described by $a_1 \leq \frac{1}{2}$ which is guidance when $a_1 > a_2, a_3$. Based on eq. (24), the stability criterion is derived in Appendix B including all the terms given in the equation:

$$\delta t \leq \frac{2kT}{D_{III}\left[\frac{U_{III}}{T}\left(\frac{dT}{dy}\right)_{III} + \frac{q\lambda(\rho(y)-\rho_0)}{\varepsilon}\right]}\delta y$$

The explicit form of eqs. (8) and (9) can be obtained by setting a3 = a4 = a5 = 0 and replacing D_{III}, U_{III}, and $(dT/dy)_{III}$ with their respective counterparts for Zones I and II in eq. (24).

During Stage 1 growth, the update steps for s1 and s2 (eq. (4) and (5)) are discretized as:

$$s_1^{j+1} = s_1^j + \frac{D_{III}\left(T_{M-1}^j\right)c_{III}^j|_{M-1}\delta t}{2\rho_{Zr}\delta y} \tag{25}$$

$$s_2^{j+1} = s_2^j + \frac{D_{II}\left(T_{M-1}^j\right)c_{II}^j|_{M-1}\delta t}{\rho_{Zr}\delta y} \tag{26}$$

where the index (M − 1) represents the spatial point immediately before the corresponding interface. Figure 2-2 displays the schematic flow diagram of the integrated numerical model.

2.1.8. Oxidation model parameterization

The assurance of the calculations' physical fidelity depends on the parameterization of the above kinetic model. During Stages 1 and Stage 2 kinetics, the key parameters are the diffusivities of free oxygen in α-Zr, in the δ′ suboxide, and in monoclinic zirconia, as well as thermal conductivities, elastic properties, and electrical properties. Although the model lacks a comprehensive data set to satisfy its needs, available experimental and numerical sources can fill those needs. First-principles electronic structure calculations have enhanced capabilities of providing diffusion coefficients in oxide structures due to recent improvements in the levels of

accuracy and computational efficiency. However, despite the potential of ab initio methods, performing calculations are exceedingly difficult for parametric spaces greater than one; thus

Table 2-1:
Physical parameters used in the model. The sources for each parameter are given in Section .

Property	Symbol	α-Zr (Zone I)	ZrO (Zone II)	ZrO_2 (Zone III)
Diffusivity prefactor [$m^2 \cdot s^{-1}$]	D_o	6.61×10^{-6}	1.26×10^{-11}	9.00×10^{-8}
Activation energy [eV]	U	1.9	1.24	1.24
Thermal conductivity [$W \cdot m^{-1} \cdot K^{-1}$]	κ	$8.8527 + 7.0820 \times 10^{-3} T + 2.5329 \times 10^{-6} T^2 + 2.9918 \times 10^{3} T^{-1}$	$\frac{\kappa_I + \kappa_{III}}{2}$	$1700 T^{-1}$ **
Charge density [$C \cdot m^{-2}$]	ρ_0	N/A		662.0
Charge [C]	q_i	N/A		-3.204×10^{-19}
Permittivity constant [$C^2 \cdot eV^{-1}$]	ε	N/A		3.262×10^{-29}
Young's modulus [GPa]	E	N/A		236
Poisson's ratio	ν	N/A		0.25
Surface energy [$J \cdot m^{-2}$]	γ	N/A		1.2
Heat flux [$W \cdot m^{-2}$]	q_0		1.917×10^{6}	

**With a factor of 0.86 applied if during Stage 2.

electronic structure calculations are complemented with experimental data where needed. Table 2-1 lists the compilation of all parameters used. The following subsections discuss the specific values and source of origin for each type of parameter.

2.1.8.1. Oxygen diffusivity in metallic Zr

In principle, temperature (T) and depth (z) are key independent variables needed to obtain the diffusion coefficient of oxygen in hexagonal closed pack (hcp) Zr. As noted above, the Arrhenius expression captures the temperature dependence. Although the dependence on z has not been established based on literature, the extrapolation of experimental measurements where the oxygen concentration is needed to capture the final value of the parameters.

Several studies have focused on oxygen diffusion in Zr ever since Pemsler's first experimental measurements [119]. Ritchie and Atrens [120] have provided a best fit of data

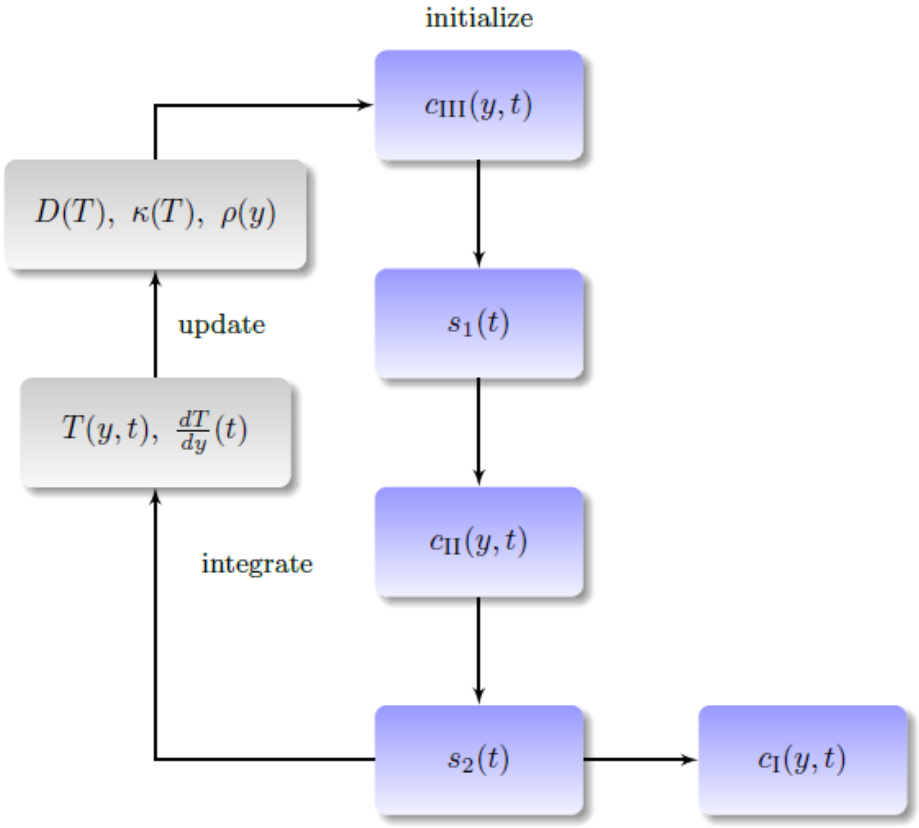

Figure 2-2: Flow diagram of the numerical procedure employed in this model.

based on an excellent compilation of all the experimental data up to 1977. For temperatures in the range 290–650 °C, they extrapolated the following expression:

$$D_I(T) = 6.61x10^{-6} exp\left(-\frac{1.9\ [eV]}{k_B T}\right)\ \ [m^2 \cdot s^{-1}]$$

The activation energy has units of eV per atom which is approximately equivalent to 44,000 cal per mole. Jumps of oxygen interstitials in the basal plane is the method of diffusion in this case. Above 400 °C some authors have measured a different expression with higher diffusivities

resulting to diffusion along grain boundaries [121]:

$$D_i^{GB}(T) = 1.55x10^{-10}exp\left(-\frac{1.0\ [eV]}{k_BT}\right)\ \ [m^2 \cdot s^{-1}]$$

Subsequent experiments have obtained similar values based on revisions on the measurements provided by Ritchie and Atrens [122]. Recent density functional theory calculations of interstitial oxygen migration with reported energies of approximately 1.0eV have been replicated by experimentally measured values for U_i despite a relatively high degree of anisotropy depending on the nature of the jump [106].

2.1.8.2. Oxygen diffusivity in monoclinic ZrO_2

Measurements of oxygen diffusivity in monoclinic zirconia have started back in the late 1960s, with Smeltzer and collaborators providing results for temperatures above 1000℃ [123, 124] which is extracted from their data shown below:

$$D_{III}(T) = 9.73x10^{-7}exp\left(-\frac{2.42\ [eV]}{k_BT}\right)\ [m^2 \cdot s^{-1}]$$

while Keneshea and Douglass [125] measure the following:

$$D_{III}(T) = 2.34x10^{-6}exp\left(-\frac{1.96[eV]}{k_BT}\right)\ [m^2 \cdot s^{-1}]$$

where both diffusivities are in $[m^2 \cdot s^{-1}]$ and the activation energies are in eV. Both measured diffusivities appear to be relatively "fast" which indicates oxygen diffusion through grain boundaries and/or defects. Cox and Pemsler [126] has noted that lattice diffusion and defect-mediated diffusion are equally important at temperatures below 600 °C since lattice diffusion occurs at a significantly lower activation energy, < 1.5 eV. Reduced vacancy formation energy in the presence of impurities is a cause of the lower activation energies. While Cox and Pemsler's

measurements were made in the 400–585°C temperature range, the earlier work by Smith was done in the 380–386°C temperature range [121] along with a reduced activation energy (1.24 eV). Due to the model's temperature range of 327–387°C, Smith's diffusivities are used as given by the expression:

$$D_{III}(T) = 9.00x10^{-8} exp\left(-\frac{1.24\ [eV]}{k_B T}\right)\ \ [m^2 \cdot s^{-1}]$$

2.1.8.3. Oxygen diffusivity in the δ′ suboxide

Since ZrO is a relatively new phase, no sources of data for oxygen diffusivity in ZrO are currently available in the model. The diffusion is assumed to proceed through a vacancy mechanism because the δ′ suboxide is a saturated line compound resulting with slower diffusivities. An approach is utilized to estimate the oxygen diffusivity by matching the ZrO thickness to the corresponding experimentally measured ZrO layer thickness ($s_2 - s_1$ from our model) between appoximately 60 nm and 120 nm [85–87]. Matching D_{II} (value is = 1.46×10^{-22} $m^2 \cdot s^{-1}$ at 600 K) in eq. (9) is calculated into the drift diffusion equation to yield a thickness of 65nm. The reason for the very low diffusivity of oxygen in the δ′ suboxide is unknown at this point. It is expected that anion diffusion exceedingly slow for strong line compounds, with a very small concentration of oxygen vacancies. This is a gap for understanding the physics of the Zr-O system; thus speculation and approximations can be done at this point until reliable experimental data and calculations are available for the diffusion mechanism of oxygen in this δ′ phase.

2.1.8.4. Thermal conductivities

From a statistical analysis of experimental measurements from 1951 to 1995, Fink and Leibowitz have developed an equation for the thermal conductivity of zirconium metal between

298 K to 2000K is:

$$\kappa_I(T) = 8.8527\ [\mathrm{W}\cdot\mathrm{m}^{-1}\cdot K^{-1}] + 7.0820\times 10^{-3}[\mathrm{W}\cdot\mathrm{m}^{-1}\cdot K^{-2}]T + 2.5329 \times 10^{-6}[\mathrm{W}\cdot\mathrm{m}^{-1}\cdot K^{-3}]T^2 + 2.9918\times 10^{3}[\mathrm{W}\cdot\mathrm{m}^{-1}]T^{-1}$$

in units of $W\cdot m^{-1}\cdot K^{-1}$ [127]. As a note the units of the constants are listed in the brackets.

Since ZrO_2 is an excellent insulator, lower κ_{III} vales are expected; thus experimental measurements at higher temperature can be assumed to be valid at lower temperatures. Klemens [128] has proposed the thermal conductivity of ZrO2 described by:

$$\kappa_{III}(T) = 1700[\mathrm{W}\cdot\mathrm{m}^{-1}]T^{-1}\ [\mathrm{W}\cdot\mathrm{m}^{-1}\cdot K^{-1}]$$

As the oxide layers grow and intrinsic pore network is developed during Stage 1, the thermal conductivity gradually decreases from the value provided by Klemens et al [128]. Nait-Ali et al has developed an expression to account for the deteriorating thermal conductivity which is described below:

$$\kappa_{III}(T,f) = \kappa_{III}(T)\left(1-\frac{3f}{2+f}\right)\ [\mathrm{W}\cdot\mathrm{m}^{-1}\cdot K^{-1}]$$

where f is the pore volume fraction [129]. During the commencement of spall, values of $f \approx 0.14$ are assumed [130], and the model assumes the pore volume fraction to be linearly dependent as a function of time; the time frame is between t = 0 and $t = t_{1\rightarrow 2,}$ and the fraction is from f = 0 to f = 0.14. During Stage 2 kinetics, the coolant permeates through the pores and equilibrates the oxide layer temperature with the coolant. Since no data for the thermal conductivity in ZrO is available, we assume κ_{II} as the average between κ_I and κ_{III}. As a note the heat flux of calculated from eq. (13) is $1.917x10^6$ $W\cdot m^{-2}$.

2.1.8.5. Electrical properties

The key electro-migration terms parameters from eq. (6) are the charge of oxygen anions, q_i , the charge density at the oxide interface, ρ_0, the absolute permittivity of the monoclinic oxide, ε, and the decay constant, λ. The absolute permittivity was measured to have a value of $\varepsilon = 3.26 \times 10^{-29}$ $C^2 \cdot eV^{-1}$ from various experimental data [131, 132]. While the charge of the oxygen anion (O^{2-}) is $q_i = -3.20 \times 10^{-19}$ C, the charge density is used as a fitting parameter set at a value of $\rho_0 = 662.0$ $C \cdot m^{-2}$ which is satisfactory for pure zirconium under the conditions studied here. Since dedicated measurement for ρ_0 are lacking in nuclear-grade Zr, it is difficult to determine if the value from the model is reasonable. Nevertheless, this fitted parameter is larger than of charge density measurements at oxide interfaces in metal/semiconductor junctions involving Zr [133, 134]. Finally, the decay constant is set to $\lambda = dy$. The maximum voltage at the ZrO_2/ZrO interface by calculations is 0.011 V and the electric field by calculations is 1.9×10^5 $V \cdot m^{-1}$.

2.1.8.6. Mechanical properties

Very few data on elastic properties of pure monoclinic zirconia has been reported in literature. Several authors have derived elastic constants using simulation on lattice vibration for tetragonal zirconia [135]. In monoclinic single crystals, Chan et al. [136] have performed ultrasonic velocity measurements up to 1000℃ using Brillouin scattering. Yeugo et al. [137] have reported an elastic modulus value of $E_{ox} = 236$ GPa between 300 and 600 °C for monoclinic zirconia based on a compilation of different values published in the literature. Equations (18)–(22) use this value.

The mechanical model uses a Poisson's ratio with a value of $\nu_{ox} = 0.25$ as given in commercial databases [138]; the surface energy of monoclinic zirconia, on the other hand, has an

experimental measurement at $\gamma \approx 1.2$ J m^{-2} [92, 139]. Either either s^* or ε can be estimated from eq. (22) if either one or the other is known.

2.1.8.7. Boundary conditions and physical dimensions

The boundary conditions and physical dimensions of the model are the final set of parameters needed to be defined for running the model. The clad thickness L, and the inner clad temperature T_0 and the initial outer clad temperature T_L (at t = 0) are nominal values under LWR conditions. The outer clad temperature is initially 660 K because the maximum heat transfer and maximum heat output occurs at that temperature [140].

Since the oxygen partial pressure in water is dependent on temperature, pressure, and water chemistry, the value of C_0 is allowed to be variable in LWR. Billot et al. [141] has provided initial concentration values for pressurized water reactors (PWR), boiling water reactors (BWR), water-water energetic reactors (VVER), and heavy water CANDU reactors. However, it is expected to have a relatively small amount of oxygen (and hydrogen) dissolved in water in the temperature range explored here because reduction of water on the surface of the clad make oxygen ions available. For example, Pemsler has reported a value of 0.54 g·cm^{-3} (or 1.69×1028 m^{-3}) in his studies of water corrosion of Zr [119]. To be consistent with the measurements by Motta et al. [85,142], the value of C_0 is fitted such that the model predicts a Stage 1→2 transition of 55 days for pure Zr specimens. Table 2-2 provides all these numbers.

Table 2-2:
Numerical Parameters used in the pure Zr oxidation model.

L[μm]	T_0 [K]	T_L^0 [K]	C_0 [m^{-3}]	ρ_{Zr} [m^{-3}]	s^* [μm]	δt [hr]	δy [μm]	λ [μm]
600	600	660	1.56×10^{28}	4.31×10^{28}	1.27	1.14×10^{-2}	0.058	1.0·δy

In addition, a constant value of $s^* = 1.27$ μm is used for consistency with experiments [28], regardless of reactor type. Calculating eq. (22) utilizing this choice produces a value of $\varepsilon \approx 4\times10^{-6}$ which is much smaller than the value of other oxides reported [115]. Finally, Table 2-2 also provides the spatial and temporal mesh sizes, δy and δt.

2.2. Oxidation model results

The model has been explained in Section 2.1.3 to describe the oxidation process during Stages 1 and 2 spatio-temporally. Next, the main results are presented with a brief discussion about their relevance and validity.

2.2.1. Pure Zr

The time evolution of the inner clad temperature, T_L, commences this section. The variation of T_L as a function of exposure time is shown in Fig. 2-3. The figure displays that the temperature varies by only two degrees, which produces a negligible impact on the thermal gradients developing in both layers captured by the model. Since the conservation of the total heat flux is emphasized (as to mimic constant power conditions in a LWR), the inner clad temperature changes as a consequence of maintaining a fixed coolant temperature with a value of 600 K.

Based on the calculations of eqs. (15)–(17), Fig. 2-4 shows the temperature profiles at 0, 20, and 60 days. Because water percolates through the crack network after 55 days (Stage 2 oxidation), the temperature in the entire oxide layer equilibrates with the coolant temperature. As an important feature for thermo-migration, gradients with a value of 106 $K\cdot m^{-1}$ develop in the oxide scale even though the absolute temperature changes are small. After breakaway, oxygen

diffusion is implied to be unaffected by the absence of temperature gradients in the ZrO_2 layer.

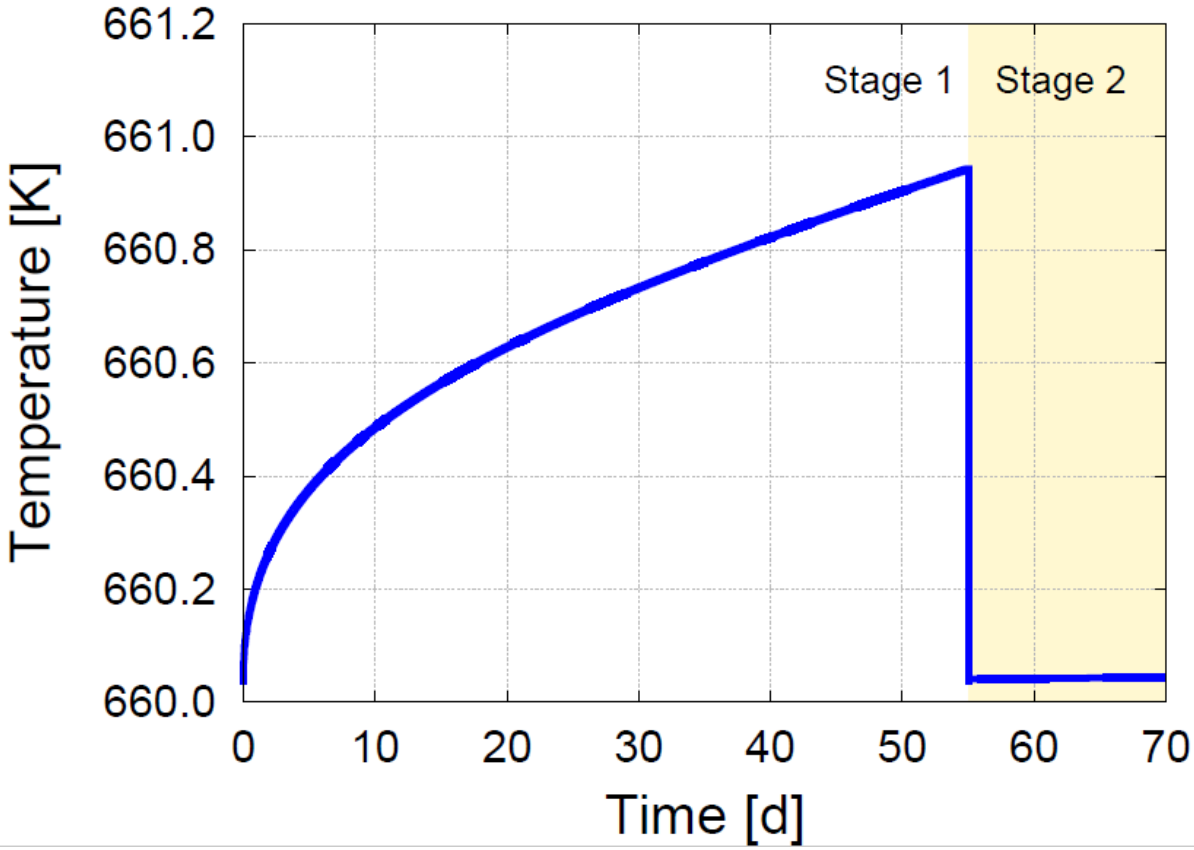

Figure 2-3: Temperature variation at y = L (inner clad radius, fuel side) as a function exposure time. The temperature steadily increases during Stage 1 and then abruptly drops after Stage 2 oxidation.

Next, the variation of the oxygen penetration inside the clad is studied as a function of depth with two distinct exposure times during Stage 1; the concentration profiles are depicted in Figure 2-5. These profiles are obtained by the solution of the drift-diffusion equation described in eqs. (8) through (10). Solid and dashed lines represent the oxygen concentrations at 20 and 40 days of exposure, respectively. Even though mass continuity exists at the ZrO_2/ZrO and ZrO/metal interfaces (marked by dashed black lines), the moving boundaries from the Stefan problem generates discontinuities in the mass fluxes. The shaded areas represent the stoichiometric oxygen concentration at ZrO_2 (blue) and ZrO (yellow) layers. As a note, the units

of concentration are in terms of the atomic density of zirconium (ρZr); the ZrO_2/ZrO interface has a value of $2\rho_{Zr}$ while the ZrO/metal interface has a value of ρ_{Zr}.

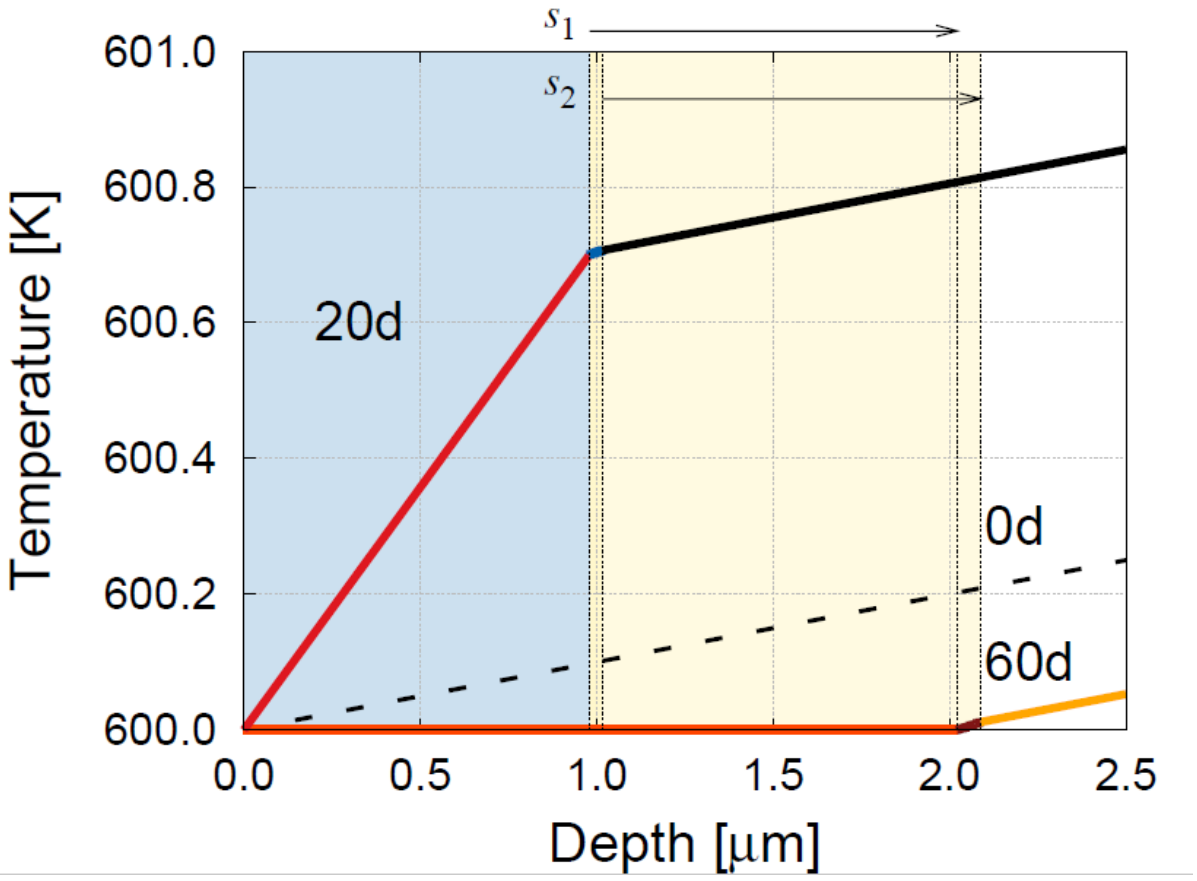

Figure 2-4: Temperature variance as a function of depth at 0, 20, and 60 days. The growth of the oxide layer(s) is depicted in the graph during each time interval. The flat temperature profile is also shown.

Figure 2-6 shows the oxygen concentration depth profiles at 60 and 70 days which are two distinct time instants during Stage 2. With complete coolant permeation during spall after 55 days, oxygen diffuses through the cracks unimpeded to the ZrO_2/ZrO interface (s_1). In terms of oxygen diffusion, the initial oxygen concentration (C_0) at the surface equilibrates at the ZrO_2/ZrO interface which results in a shift of the outer boundary of the clad from y = 0 to y = s_1. During post-transition (post-breakaway), the figure shows a transient for the oxygen content in the ZrO layer which is driven by an adjustment by the maximum in the concentration curves.

From Fig. 2-7, the positions of s_1 and s_2 are tracked as a function of time which allows for the time evolution for the oxide scale growth. The thickness of the ZrO_2 layer is denoted by the value s_1, while the value $(s_2 - s_1)$ represents the thickness of ZrO layer which is fixed to

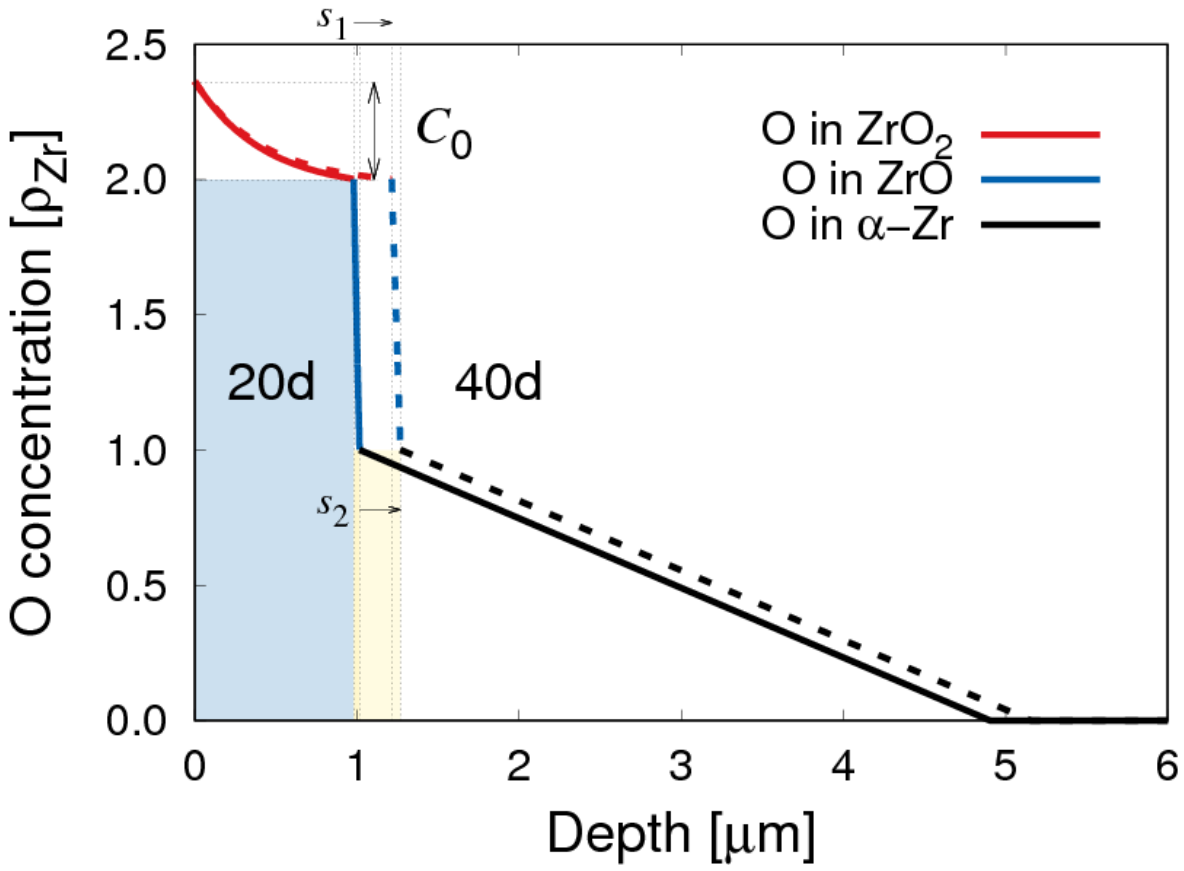

Figure 2-5: Total oxygen concentration as a function of depth at two distinct times during Stage 1 oxide scale growth. The concentration is expressed as in units of ρ_{Zr}. The shaded areas represent the thickness of the ZrO_2 (blue) and ZrO (yellow) layers**.**

approximately 65nm in this study. Both curves display nonlinear behavior up to the set value of $s^* = 1.27$ μm, which shows the transition from Stage 1 to Stage 2. Solid and dashed black lines denote the oxide scale power laws ($s = a*t^b$) which indicate the coefficients, a, and exponents, b, for each layer. The main features of our kinetic model are: (i) Prior to breakaway, the oxide scale grows as $s_1(t) = 0.33*t^{0.34}$ while the oxide-metal interface layer grows as $s_2(t) = 0.33*t^{0.35}$ (as a note, both s_1 and s_2 are expressed in microns while t is in days); (ii) the model has been

calibrated such that Stage 2 starts when $s_1 = s^* = 1.27$ μm, for a Stage 1 duration of approximately 55 days [142]; (iii) the oxide scale grows linearly after Stage 2. The model

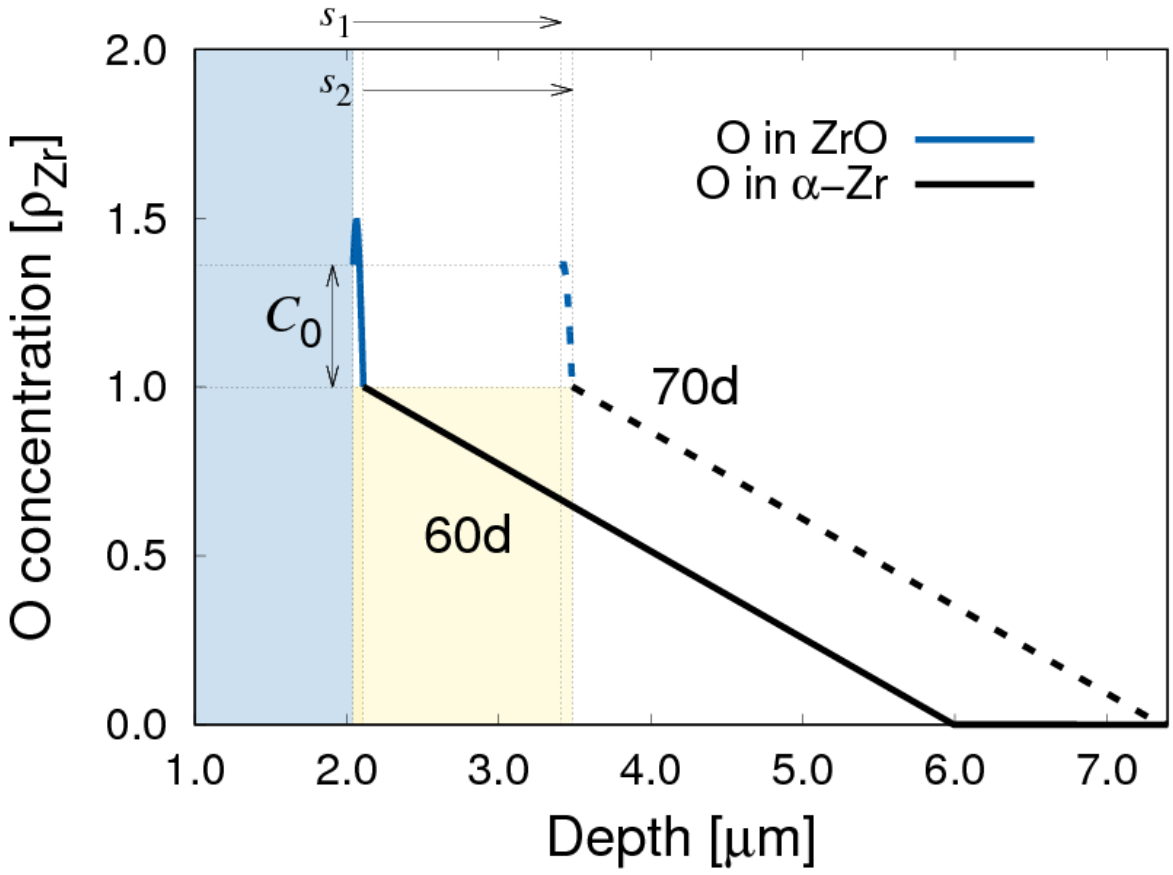

Figure 2-6: Total oxygen concentration as a function of depth at two distinct times during Stage 2 oxide scale growth. The concentration is expressed as in units of ρ_{Zr}. The shaded areas represent the thickness of the ZrO_2 (blue) and ZrO (yellow) layers.

incorporates the results from Motta et al. for pure Zr [142] based on the parameters chosen for s^* and $t_{1\to2}$ although experimental measurements found in the literature contain large variability even under nominally equivalent conditions.

Studying the relative contribution of each of the terms from the drift-diffusion equation in eq. (10) is another important topic for oxygen transport in the oxide. To determine the corresponding contribution, each term is disabled one at a time and examined for the oxide

length vs. time behavior during Stage 1. Figure 2-8 shows the results displaying three curves for each scenario. First, the diffusion equation is solved with only the Fickian term. This term alone

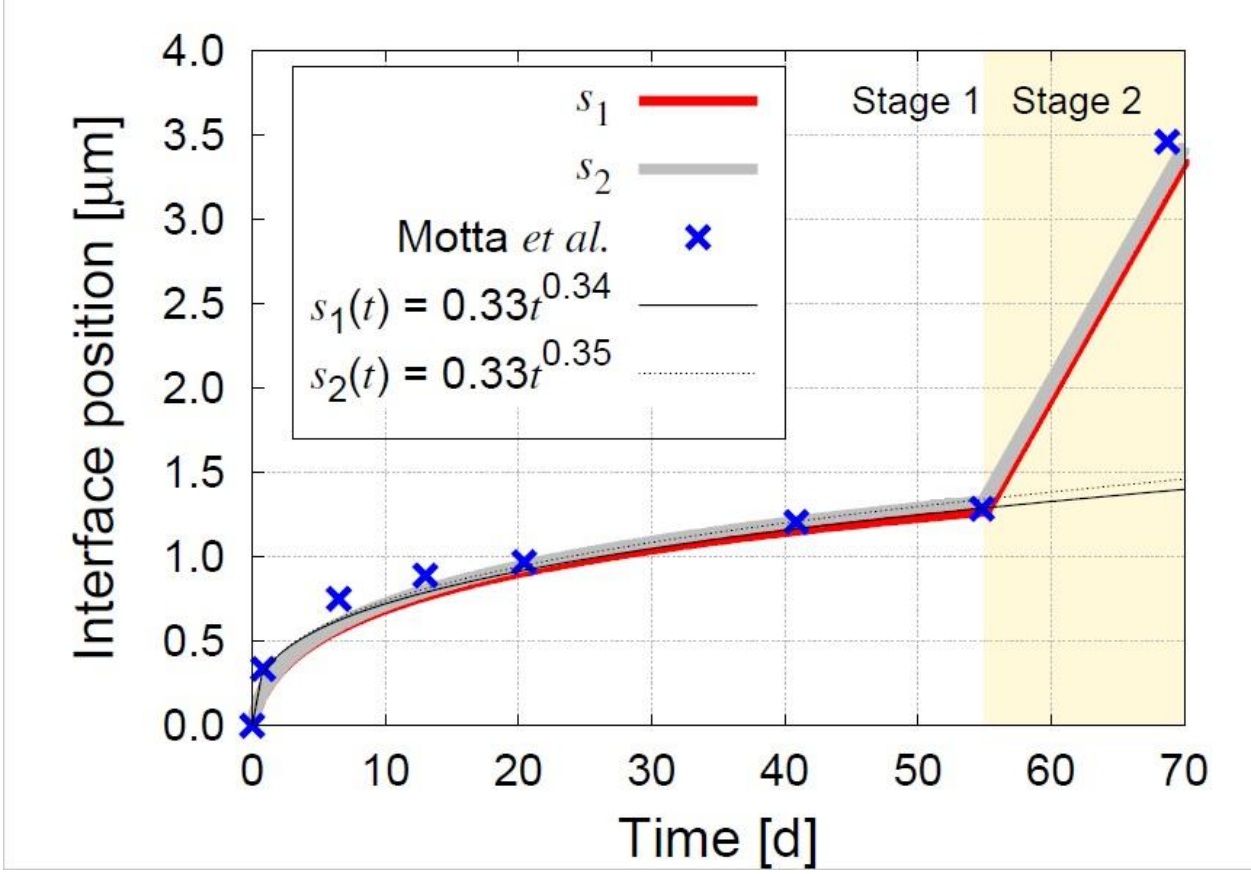

Figure 2-7: Time evolution of following two interfaces for pure Zr: s_1 (oxide scale thickness for ZrO_2) and s2 (thickness for the ZrO-metal interface). The shaded region to the right indicates the Stage 1 to Stage 2 transition where an abrupt increase in the oxide growth rate after Stage 2. The solid and dashed black lines denote the scale growth law fitted to the data for Stage 1. Experimental data from Ref. [142] is shown for comparison.

produces an expected evolution that is best fit by a $t^{1/2}$ power law. Second, the electro-migration contribution is added which results in the 'bending' of the curve towards a $t^{1/3}$ evolution. Finally, adding the thermo-migration term generates minimal variations s_1 on the order of 2% with respect to the previous case.

2.2.2. Sensitivity analysis of key parameters

To consider its response to variations in relevant parameters, a sensitivity study of the model is performed. The impact on the oxide scale for ZrO_2 (in pure Zr) is shown in Fig. 2-9 in

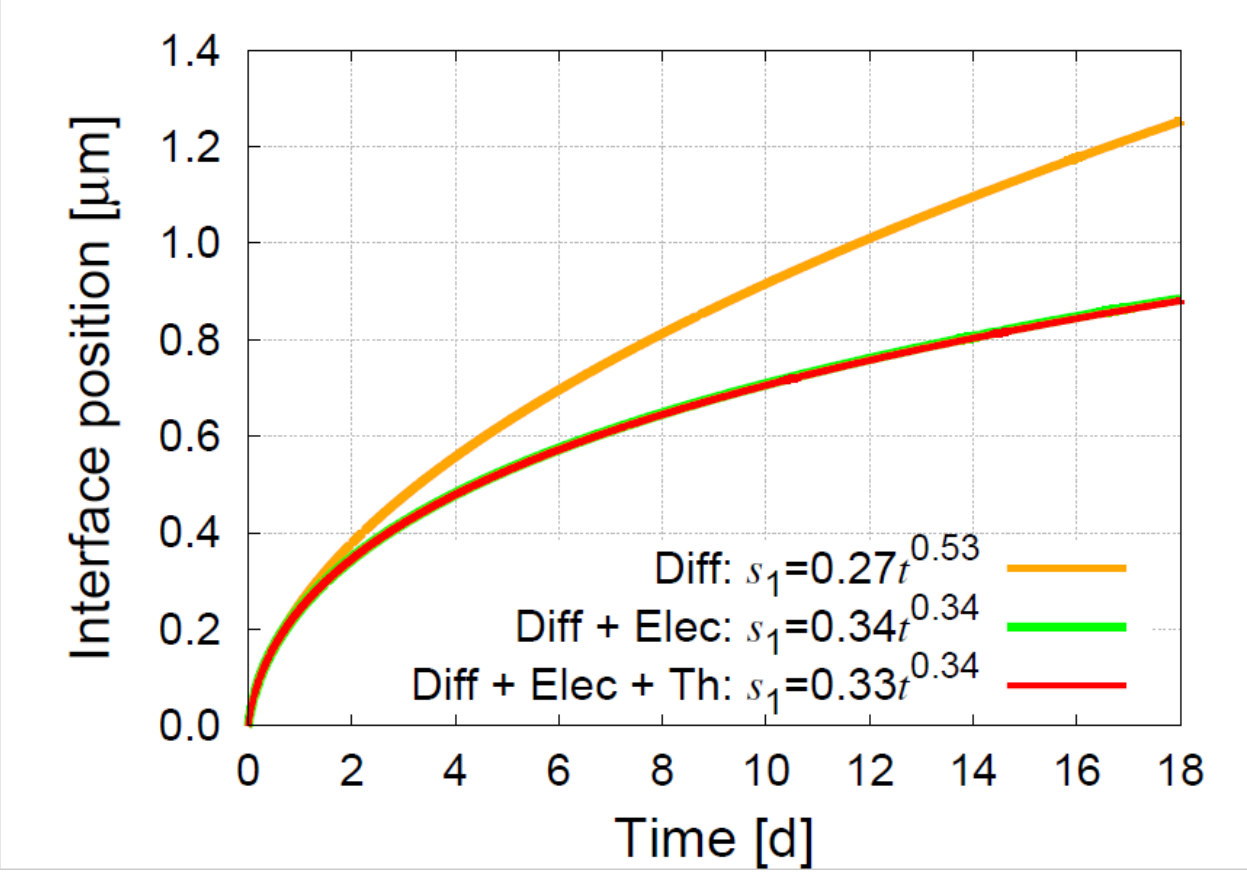

Figure 2-8: Analysis of contributions for different combination of term of the drift-diffusion equation (eq. (10)) for oxide thickness evolutions with time in ZrO_2 during Stage 1.

response to variations of the following parameters: the oxygen concentration in the environment, C_0 (Fig. 2-9a), the oxygen diffusivity in the oxide, D_{III} (Fig. 2-9b), and the charge density at the oxide/metal interface, ρ_0 (Fig. 2-9c). The plots show that variations of less than 5% in the values of s_1 is caused by changes of ± 15% in these parameters; this suggests that the model attenuates the impact of the variations in model parameters. This analysis is useful for understanding the effect of uncertainties for some of the key parameters serving as input to the model to allow for

reasonable limits on these parameters; however the study cannot exhaustively quantify uncertainties.

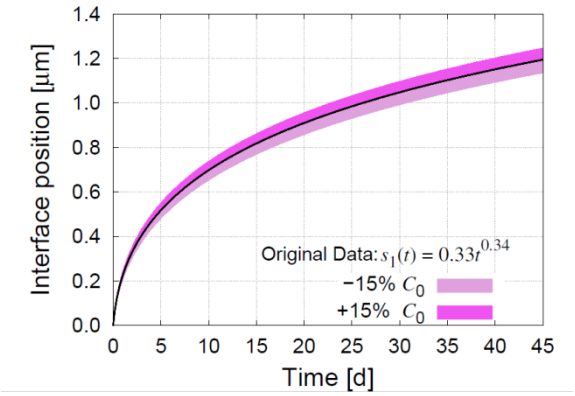

(a) Variation of s_1 with a ± 15% change in C_0

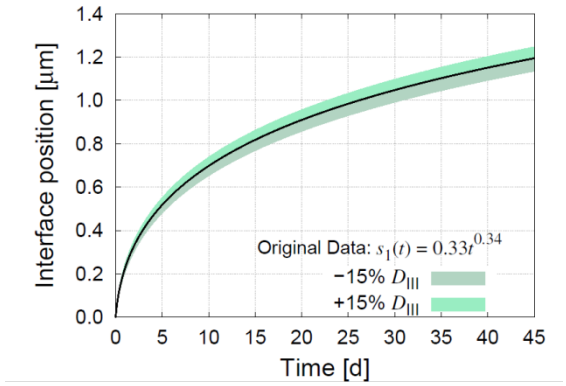

(b) Variation of s_1 with a ± 15% change in D_{III}

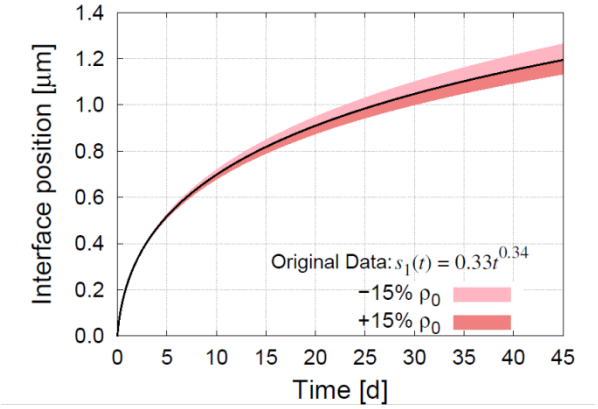

(c) Variation of s_1 with a ± 15% change in ρ_0

Figure 2-9: Oxide scale sensitivity of ZrO_2 (in pure Zr) to ± 15% variations of relevant model parameters.

2.2.3. Alloy composition effects

Considering the impact of alloy composition is another important feature on the model predictions. Even though Bell et al. [111] have recently discussed qualitative effects on alloy composition on zirconium oxidation using electronic structure arguments, Motta et al. [142] still has an excellent anthology on this topic. Similar to pure Zr, data sets for different Zr-based alloys can be challenging to obtain. Choosing alloys with known and accurately measured oxygen diffusivities (from both the oxide and the metal) is the primary approach to study chemical composition effects. In addition, the existence of a charge gradient is accessed based on the

oxide growth power law exponent in the experimental literature. Based on these criteria, Zircaloy-4 (nominal composition: Zr-1.5Sn-0.24Fe-0.13Cr) [143, 144] and Zr-2.5Nb [145] has been chosen as the alloys for this analysis. The comparison between the three alloys is displayed in Figure 2-10, with the corresponding time exponents given for each case. Pure Zr and Zircaloy-4 virtually has no distinction between each other when plotted in a normalized scale due to

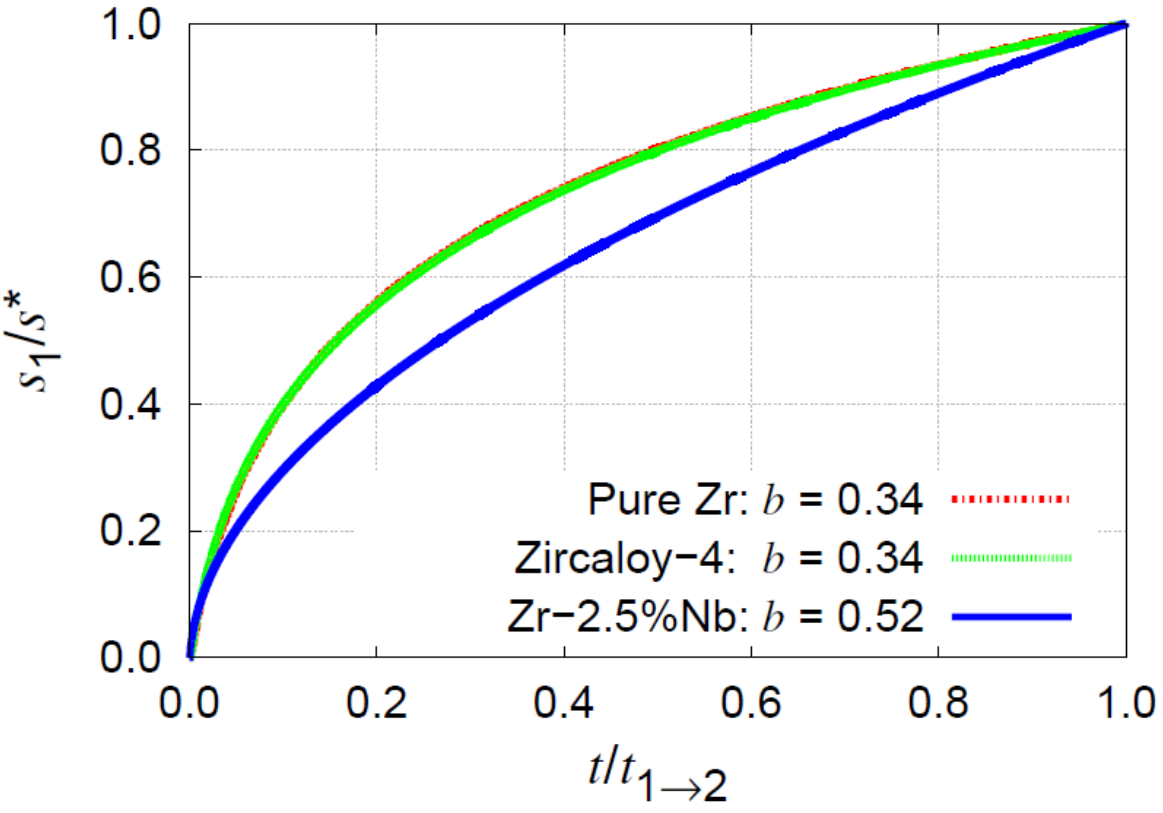

Figure 2-10: Oxide scale thickness power laws for pure Zr, Zircaloy-4, and Zr-2.5Nb. For a simpler comparison, the graph has been normalized to the failure thickness s^* (abscissa) and failure time $t_{1\to2}$ (ordinate) in each case. As a reference, the plot also provides the time exponent b in the expression $s1(t) = at^b$.

exhibiting cubic behavior. Conversely, Zr-2.5Nb differs from pure Zr and zircaloy-4 since it displays a quadratic behavior based on established experimental data. Electro-migration plays a large role for the alloy comparison since it is qualitatively identical for Zr and Zircaloy-4, but absent for Zr-2.5Nb. Bell et al. [111] has justified that the absence of electro-migration for Zr-

2.5%Nb is a result of the +5 charge from the Nb cations completely lowering the conductivity of the oxygen ions. Other features that separates Zr-2.5Nb from zircaloy-4 and pure Zr are its superior hardness and creep resistance [146]. Table 2-3 provides the differing failure thicknesses, transition times, oxygen diffusion coefficients and the rest of the fitting parameters. Chapters 3 and 4 will refer to Table 2-3 for zircaloy-4 parameters.

Table 2-3:
Parameter comparison for Pure Zr, Zirc-4, and Zr-2.5Nb. The pure Zr parameters are taken from Table 2-1. Zircaloy-4 data is taken from Refs. [142,143], while the Zr-2.5Nb data are from Zhang et al. [144].

Alloy	s^* [μm]	$t_{1\rightarrow2}$ [days]	D_I^0 [$m^2 \cdot s^{-1}$]	U_I [eV]	D_{III} [$m^2 \cdot s^{-1}$]	U_{III} [eV]	C_0 [ρ_{Zr}]	ρ_0 [$C \cdot m^2$]
Pure Zr	1.27	55	6.61×10^{-6}	1.9	9.00×10^{-8}	1.24	0.36	662.0
Zircaloy-4	2.47	149	3.92×10^{-4}	2.2	2.76×10^{-6}	1.5	0.52	156.0
Zr-2.5Nb	2.41	112	1.72×10^{-5}	1.9	1.72×10^{-5}	1.9	142.22	0.0

2.3. Discussion of oxidation model results

The potential of the methodology to model oxygen corrosion kinetics in nuclear environments is revealed by the three-layer spatio-temporal simulation of the oxidation process in Zr shown in the previous section. The formulation uses a Stefan model to track the motion of the two interfaces representing the three layers. Mass conservation boundary conditions tie the three layers together by simultaneously solving drift-diffusion equations for each layer.

The numerical treatment of the equation system is simplified by assuming a one-dimensional spatial dependence in the model along the depth direction. Although this assumption fails to account for oxide formation from a grain nucleation and growth process based on Zr clad corrosion operating mechanisms, the model has to predict relevant features associated with a polycrystalline microstructure, such as the formation of a substoichiometric (tetragonal) oxide phase near the interface as well as oxide fragmentation over time. The model also assumes that O

and Zr are the only chemical species considered even though hydrogen and water chemistry strongly impact the oxidation kinetics and alloy composition in Zr alloys.

One of the model's main features is the ability to capture a multilayer representation of the oxidation process. Based on the literature, the formation of the δ' suboxide occurs in out-of-pile (autoclave or corrosion loop) conditions, but this phase has not yet been detected under in-pile conditions. Since the explanation for the suppression of the ZrO region under in-pile conditions remain unclear, the model assumes out-of-pile conditions leaving the effects of irradiation for future studies. In addition, the model does not consider the third line compound ($ZrO_{1/2}$) predicted by DFT calculations and seen in experiments because the beneficial inclusion of this extra compound fails to outweigh additional difficulties to formulate a four-layer model.

A combination of first-principles and (semi)phenomenological elements is required to formulate a corrosion model due to the complexity of the oxidation process. Moreover, the sources of the parameters can range from decades old experimental data to more recent electronic structure calculations. Since the sources of the data are often not interchangeable, caution must be exercised when mixing both old and recent data. Most of the time, calculations are the only means to obtain relevant model parameters and material constants.

The oxygen concentration in the environment side, C_0, and the charge density, ρ_0, are the two key parameters than merit additional discussion for the model mainly designed for pure Zr and zircaloy-4 since detailed experimental data sets exist. For example, pure Zr is known to attain Stage 2 behavior at a critical oxide thickness of 1-to-2 μm, while Zircaloy-4 is seen to reach post-transition around 2.5 μm. The parameters C_0 and ρ_0 has been used to recover characteristic $t^{1/3}$ kinetics for Stage 1 which can be obtained by multiple combinations of values for these two variables. Although the values employed are noted to be not definitive, these parameters are ensured to stay within experimental limits and avoid uncontrollable fluctuations.

Although electro-migration induced by a charge gradient near the oxide interface has the capability of bending the quadratic diffusive curves, only a suitable parameter choice can yield the $t^{1/3}$ behavior observed from experiments previously known in the community for some time [107, 147]. This oxidation model has been presented to showcase how to achieve the cubic behavior.

The model uses an explicit second-order finite difference discretization to solve partial differential equations numerically. Based on the numerics of the present calculations, the timescale utilized has been the main difficulty because the time increments set by material constants (e.g. diffusivities, and dielectric constants) must meet the limits set by the numerical stability criteria. In addition, achieving time synchronicity across different layers can be challenging because material constants dictate the relationship between δt and δy (from Sec. 2.1.7); thus the time step needs an extra constraint to ensure synchronous evolution of the interfaces.

Finally, irradiation effects are not explicitly incorporated in the oxidation model. According to multiple studies, irradiation slightly affects Stage 1 oxidation while it produces major effects on Stage 2 kinetics [53,148]. However, oxidation during the early stages of corrosion is significantly enhanced by higher dose rates based on newer data [149]. As mentioned above, a model capturing these effects is described in chapter 4 of this dissertation. Capturing the cubic growth kinetics for Stage 1 oxidation and obtaining a mechanical failure criterion based on Stage 2 kinetics have been the primary goals for this chapter. Although the goals have been met quantitatively, additional work is necessary to fully understand the peculiarities of Zr oxidation in nuclear environments.

2.4. Conclusions of oxidation model

This chapter is ended with a list of the most relevant conclusions for the oxidation model:

- A numerical model of oxide scale formation and growth in zirconium under nuclear reactor operating conditions has been developed in one dimension. The motion of interfaces is tracked based on equations governed by oxygen diffusion in response to concentration, thermal, and electrical gradients.
- Formation of three layers is incorporated in the model: monoclinic oxide (outermost), δ′ suboxide (middle), and metallic Zr suboxides and solid-solutions (innermost).
- Oxide fragmentation and Pilling-Bedworth stresses have been used to derive the mechanical failure criterion for predicting the transition from Stage 1 to Stage 2 oxidation.
- Experimental and computational data has parameterized the model, and a complete temperature dependence across the Zr clad has been captured in the model.
- When it considers electro-migration and selects a suitable combination of parameters, the model can predict a cubic growth behavior for Stage 1 oxidation. The desired oxide scale is yielded when these parameters are fitted to reasonable values.
- Due to compressive stresses accumulating in the oxide/metal interface, the sharp transition to breakaway growth in Stage 2 has been exhibited after oxide scale fragmentation.
- Based on the preliminary sensitivity analysis, variations of ± 15% in key model parameters have produced changes of less than 5% in the oxide layer thickness as a function of time.

3. Chapter 3: Irradiation Enhanced Corrosion

3.1. Oxidation kinetics model with irradiation

3.1.1. Overview of irradiation effects

Neutron irradiation generates zirconium vacancies and interstitials at a constant rate [52]. Zircaloy-4 becomes hardened above 288°C arising from dislocation loops caused by neutron irradiation [54]. At 288°C, surface migrations and direct defect annihilation causes the hardening of the mobile zirconium vacancies and interstitials until they reach a steady state concentration [52]. This production and annealing of the mobile vacancies and interstitials results in an increased diffusion rate [52]. This irradiation eventually leads to the degradation of corrosion resistance thereby enhancing the cracking from Stage 2 kinetics [54]. Depending on the dose rate, the oxide starts to form in arrays with different orientations relative to the orientation of the Zr grain on which they form. As depicted in Figure 3-1, columnar nano-crystals (Fig. 3-1a) form at lower dose rates ($\approx 7.0 \times 10^{-8}$ dpa·s^{-1}) while equiaxed nano-crystals (Fig. 3-1c) form higher dose rates ($\approx 3.5 \times 10^{-6}$ dpa·s^{-1}) [38, 150]. A combination of equiaxed and columnar crystals (Fig. 3-1b)

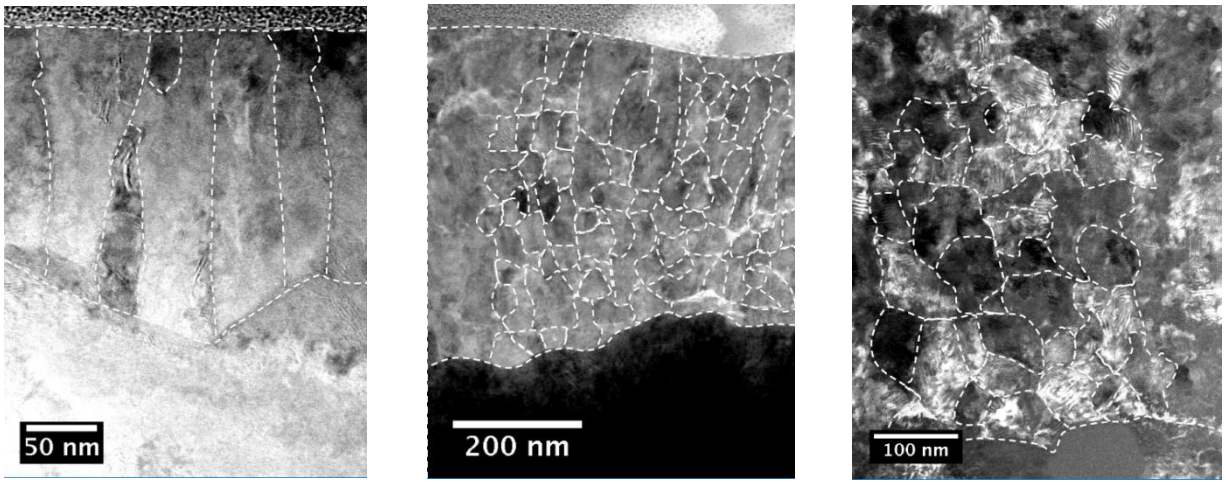

(a) 7.0×10^{-8} dpa·s^{-1} (b) 2.2×10^{-7} dpa·s^{-1} (c) 3.5×10^{-6} dpa·s^{-1}

Figure 3-1: Evolution of microstructure as a function of damage rate. The transition from columnar to equiaxed grain growth is shown with increasing dose rate. The top of the figures represents the environment side [150].

exist under normal irradiation condition at dose rate equal to $2.2x10^{-7}$ dpa·s^{-1} [150] (originally $4.4x10^{-7}$ dpa·s^{-1} [50, 51]).

While in-pile data is dispersed and difficult to reproduce using charged particle irradiation [151–153], alternatives using ion–beam data has been inconclusive [154–156]. Zu et al has proposed to utilize proton instead of neutron irradiation due to cost and time constraints [54]. Even though protons feel electrostatic repulsion, they are able to reproduce neutron damage since both particles contain high energy and deeper penetration [54]. At higher dose rates, the oxide growth rate evolves linearly with the dose rate; from their findings, the oxide kinetics follows post-transition behavior [49–51]. From the Crystallographic orientation deviation plots shown in Figure 3-2, the following crystal orientations exist: non-irradiated oxides (Fig. 3-2a) exposed at 350°C for 106 days grow in columnar orientation while both neutron irradiated (Fig. 3-2b) and proton irradiated (Fig. 3-2c) exposed at 320°C grow in a mixture of equiaxed and

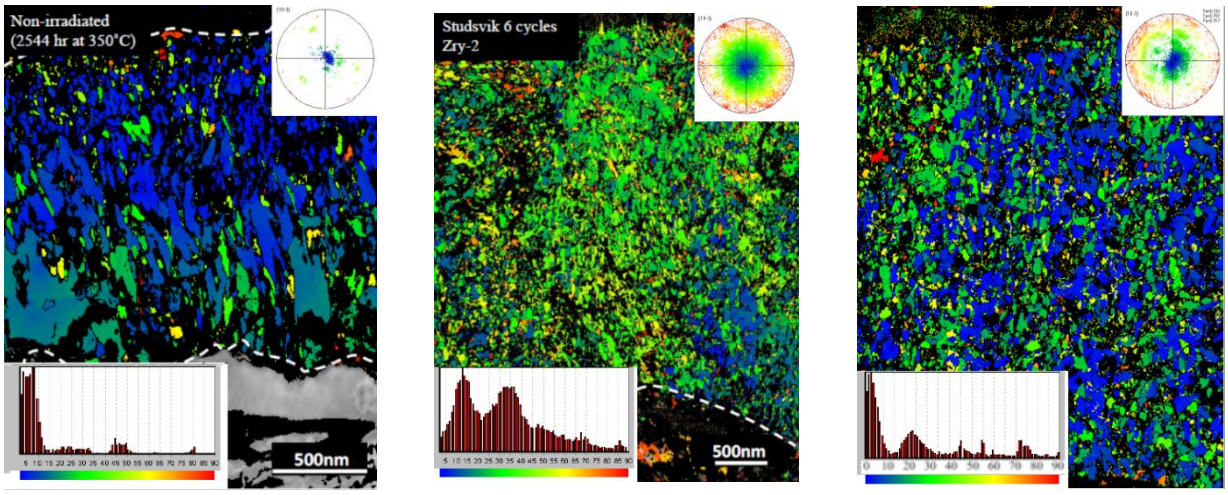

Figure 3-2: Crystallographic orientation deviation plots under (a) non-irradiated conditions (106 days at 350°C), (b) neutron-irradiated in-pile conditions (six cycles in the Leibstadt Nuclear Reacor at 320°C), and (c) proton-irradiated in-pile conditions (24 hours at 320°C) [150].

columnar orientations. Proton irradiated oxides contain more columnar grains than the neutron irradiated ones because protons have lower energy than neutrons at the same temperature [51, 54].

3.1.2. Models of radiation enhanced diffusion

In this section, the irradiation effects, previously not incorporated in the oxidation model, are accounted for because major effects on are produced in Stage 2 kinetics [53,148]. Even though most equations described in Chapter 2 hold for the irradiation model, any equations involving thermal gradients are nonexistent because the experimental conditions for the proton irradiation are performed at a constant temperature (320℃). Thus eq. (6) simplifies to:

$$\frac{\partial c_I}{\partial t} = \nabla(\mathrm{D_I}\nabla c_I) \tag{27}$$

$$\frac{\partial c_{II}}{\partial t} = \nabla(\mathrm{D_{II}}\nabla c_{II}) \tag{28}$$

$$\frac{\partial c_{III}}{\partial t} = \nabla(\mathrm{D_{III}}\nabla c_{III}) + \frac{\mathrm{q_{III}D_{III}}}{\mathrm{kT}}\nabla(c_{III}\nabla\phi) \tag{29}$$

where a charge gradient is assumed to develop due to an excess oxygen vacancy concentration at the interface associated with tetragonal zirconia formation [107]. The boundary conditions for eqs. (27)–(29) are identical the ones described in section 2.1.3. Furthermore, the same numerical procedure and equations described in 2.1.7 apply for the oxidation model with irradiation effects.

The other addition to the oxidation model involves the enhancement of corrosion by higher dose rates due to the production of defects and dislocations on the vacancies in the metal [149]. Dienes and Damask [52] have predicted the behavior of radiation enhanced diffusion linearly while Averback and Hahn [55] utilized a quadratic model for the enhanced diffusivity in

terms of the ion flux and fluence instead of damage rate. Applying both formulations, the standard form for radiation enhanced diffusion (RED) coefficient under steady state conditions is:

$$D_{ox}^{rad} = D_{ox}(1 + a\dot{\varphi}^b) = D_{ox}^0 \cdot exp\left(-\frac{U_{ox}}{kT}\right)(1 + a\dot{\varphi}^b) \quad (30)$$

where D_{ox} represents D_{II} and D_{III}, U_{ox} represents U_{II} and U_{III}, $\dot{\varphi}$ is the dose rate, *a* is a proportionality constant, and b is the exponent reflecting the nature of irradiation defect recombination. When point defects annihilate at fixed sinks or recombine, the RED coefficient depends linearly on irradiation flux (b =1) [52]. On the other hand, the RED coefficient depends quadratically on irradiation flux (b = 1/2) when the defects annihilate by recombination [55]. In terms of Stage 2 kinetics, the oxide growth rate is independent of dose rate. Even though the oxide thickness during fragmentation is virtually unaffected by irradiation, the transition times accelerate in response to the dose rate.

3.1.3. Irradiated oxidation model parameterization

Parameterization of the oxide kinetics model involving both non-irradiated and radiation enhanced oxidation are necessary to ensure physical fidelity of the model. In terms of non-irradiated oxide kinetics, the diffusivities of free oxygen in zircaloy-4 metal, in the ZrO, and in ZrO_2 are listed in Table 2-3. In terms of irradiation effects, the key parameters are the radiation enhanced diffusivities of free oxygen in all zones and the damage rates provided by the University of Michigan's experimental data. The model is independent of thermo-migration because the University of Michigan [49–51] conducted their experiments at 320^{o}C. The values and sources of each parameter will be discussed in the following subsections.

3.1.3.1. Zircaloy-4 under non-irradiated conditions

While diffusivities of non-irradiated zircaloy-4 are available in Table 2-3, parameters such as s^* and $t_{1\rightarrow2}$ are different because of the experimental conditions performed by the University of Michigan [49–51]. Motta [142, 157] and Yilmazbayhan [28] have obtained experimental measurements of post-transition kinetics in zircaloy-4 exposed to 360^{o}C water where the Stage 2 transition times $t_{1\rightarrow2}$ = 28–149 days and the oxide length of s^* = 1.5–2.47 μm. However, the different experimental setup (320 ^{o}C with 3 wt ppm H_2) from Wang and Was [49, 50] produced post-transition behavior at 512 days with oxide thickness s^* = 2.2 μm [150]. For consistency with the experimental conditions of University of Michigan, the model matches identical post-transition behavior. Other properties include the electrical parameters of the oxide which are provided in Table 3-1.

Table 3-1:
Numerical parameters used in the zicaloy-4 non-irradiated oxidation model.

T [K]	C_0 [m^{-3}]	ρ_0 [$C \cdot m^{-2}$]	$t_{1\rightarrow2}$ [days]	s^* [μm]	δt [hr]	δy [μm]
593	3.74×10^{28}	145.0	512	2.2	0.26	0.15

3.1.3.2. Zircaloy-4 under irradiated conditions

Findings from Wang and Was discussed at the CASL meeting [149, 150] have showed data containing a plot of oxide thickness as a function of the cube root of time with increasing dose rate; this data is based on in-pile and out-of-pile corrosion kinetics using the MATPRO simulation. Within one year, their updated data [158] as shown in Figure 3-3, describes the acceleration of the corrosion transition with increasing dose rate with the square root of time. To be consistent with experimentally obtained data [28, 142], the oxide lengths should be between 1.5 – 2.47 μm since the actual breakaway points are not measured at higher doses in Figure 3-3.

Assuming $s^* = 2$ μm for all nonzero dose rates, the approach is to match $t_{1\rightarrow 2}$ corresponding to thicknesses of 2 microns.

Under non-irradiated conditions, the diffusivity corresponding to zone III zircaloy-4 from Table 2-3 and the Stage 2 parameters from Table 3-1 are used. With non-zero damage rate, the diffusivities are measured based on the $t_{1\rightarrow 2}$ corresponding to $s^* = 2$ μm. Table 3-2 lists the relevant parameters obtained from Figure 3-3 and eq. (30). The following paragraphs will discuss the details on the calculated diffusivities.

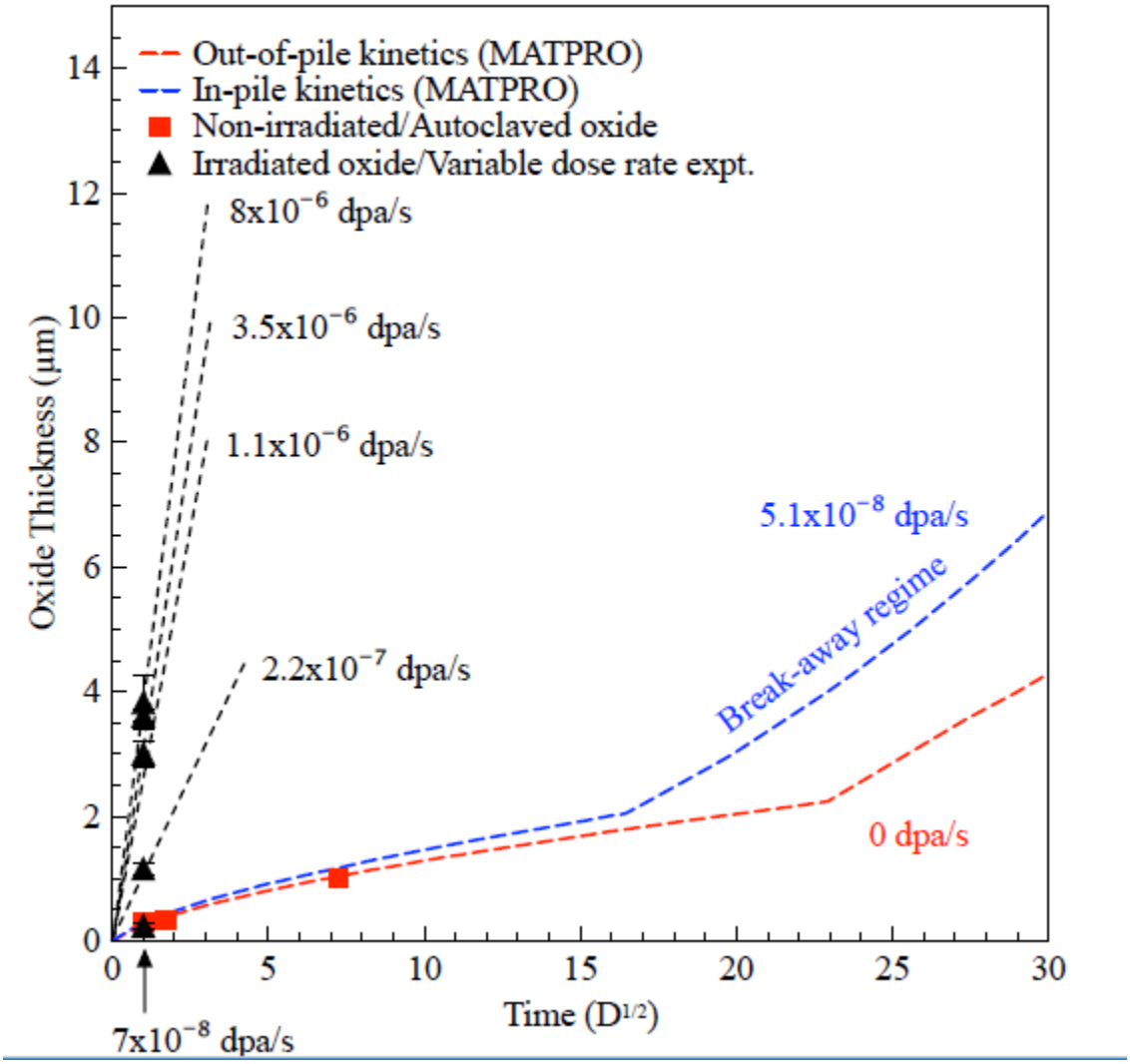

Figure 3-3: Evolution of the irradiated oxide scale thickness for zircaloy-4 as a function of the square root of time with increasing damage rate [158].

Figure 3-4 tracks the dose rate as a function of diffusivity under linear and quadratic approximations in a log-log scale. The accuracy is improved by partitioning the data sets into linear approximations for low damage rates and quadratic approximations for high damage rates.

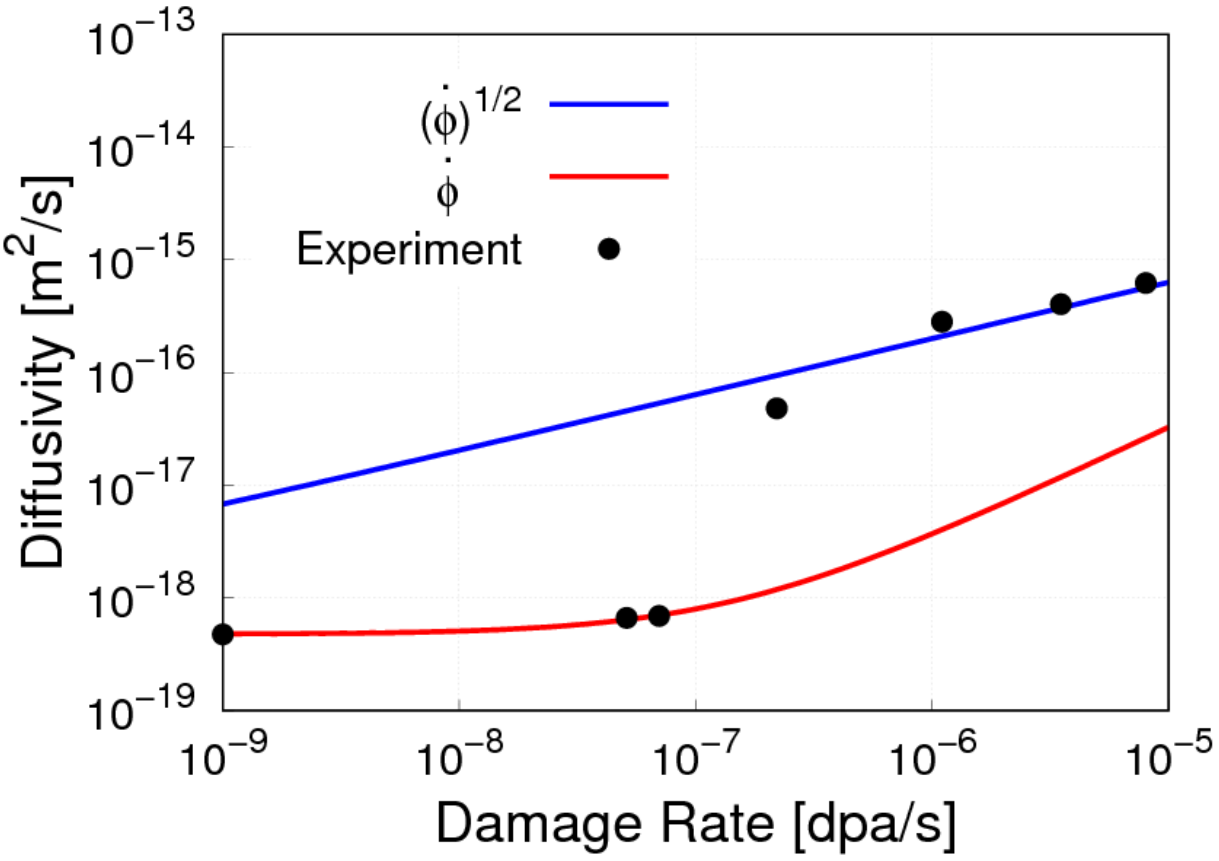

Figure 3-4: The radiation enhanced diffusivity (RED) as a function of dose rate and fits to two RED models based on eq. (30).

Based on statistical analysis of diffusivities from Table 3-2, the linear and quadratic proportionality constants from the radiation enhanced diffusion expression are "b = 6.8×10^{-6} s·dpa^{-1}" and "b = 4.2×10^{-5} s·dpa^{-1}" respectively. From Figure 3-3, data sets for low dose rates almost match the linear measurement while data sets for the three highest dose rate data almost correspond to the quadratic calculation. The dose rate of 2.2×10^{-7} dpa·s^{-1} is neither linear nor quadratic since this point represents the transition; more data points are needed to get a more

accurate representation of this point. This observation clearly shows that $\dot{\varphi} = 2.2\text{x}10^{-7}$ dpa·s^{-1} is considered the normal irradiation condition.

Table 3-2: Key irradiation parameters from experimental and calculated sources.

Source		Experimentally		Calculated by eq. (30)	
$\dot{\varphi}$ [dpa·s^{-1}]	s^* [μm]	$t_{1\rightarrow2}$ [days]	D_{ox}^{rad} [m^2·s^{-1}]	$t_{1\rightarrow2}$ [days]	D_{ox}^{rad} [μm^2·hr^{-1}]
0	2.2	512	$4.75\text{x}10^{-19}$	512	$4.75\text{x}10^{-19}$
$5.1\text{x}10^{-8}$	2.0	265	$6.65\text{x}10^{-19}$	276	$6.40\text{x}10^{-19}$
$7.0\text{x}10^{-8}$	2.0	255	$6.92\text{x}10^{-19}$	251	$7.01\text{x}10^{-19}$
$2.2\text{x}10^{-7}$	2.0	3.7	$4.81\text{x}10^{-17}$	3.7	$4.81\text{x}10^{-17}$
$1.1\text{x}10^{-6}$	2.0	0.64	$2.82\text{x}10^{-16}$	0.83	$2.10\text{x}10^{-16}$
$3.5\text{x}10^{-6}$	2.0	0.42	$4.03\text{x}10^{-16}$	0.47	$3.74\text{x}10^{-16}$
$8.0\text{x}10^{-6}$	2.0	0.28	$6.22\text{x}10^{-16}$	0.31	$5.66\text{x}10^{-16}$

3.2. Oxidation model with irradiation results

3.2.1. Oxide scale evolutions with irradiation

Originally, Wang and Was [149, 150] has plotted the evolution of the oxide thickness as a function of the cube root of time instead of the square root of time to impose a linear relation on Stage 1 kinetics. For consistency with the original formulation, Figure 3-5 depicts the tracking of s_1 with the cube root of time along with data points shown in Figure 3-3. The colors for each oxidation profiles are different based on the corresponding dose rate. The squares represent the experimental data from Wang and Was [158] while the triangles represent the model generated $t_{1\rightarrow2}$ from Table 3-2. All oxide thickness profiles are linear before the transition from Stage 1 to Stage 2; at post-transition, the plots become nonlinear.

For dose rates above $2.2\text{x}10^{-7}$ dpa·s^{-1}, an $s^* = 2$ μm is assumed to match the corresponding $t_{1\rightarrow2}$ since the transition time and oxide thickness are not known at these dose rates. The data points from Wang and Was [158] are within the range of the model. The tracking of s_1 as a function of time corresponds to the following power laws at the specified damage rates

are:

$$s_1^0(t) = 0.28t^{0.33} \quad s_1^{5.1x10^{-8}}(t) = 0.30t^{0.33} \quad s_1^{7.0x10^{-8}}(t) = 0.31t^{0.33}$$

$$s_1^{2.2x10^{-7}}(t) = 1.31t^{0.33} \qquad s_1^{1.1x10^{-6}}(t) = 2.12t^{0.32}$$

$$s_1^{3.5x10^{-6}}(t) = 2.55t^{0.32} \qquad s_1^{8.0x10^{-6}}(t) = 2.91t^{0.32}$$

where units of the constants are in $\mu m \cdot d^{-1/3}$.

3.2.2. Oxide growth rate evolutions with irradiation

The effects of corrosion rate with dose rates are another relevant topic to consider. From Wang and Was [50], the damage rate and oxide growth rate are proportional since oxide

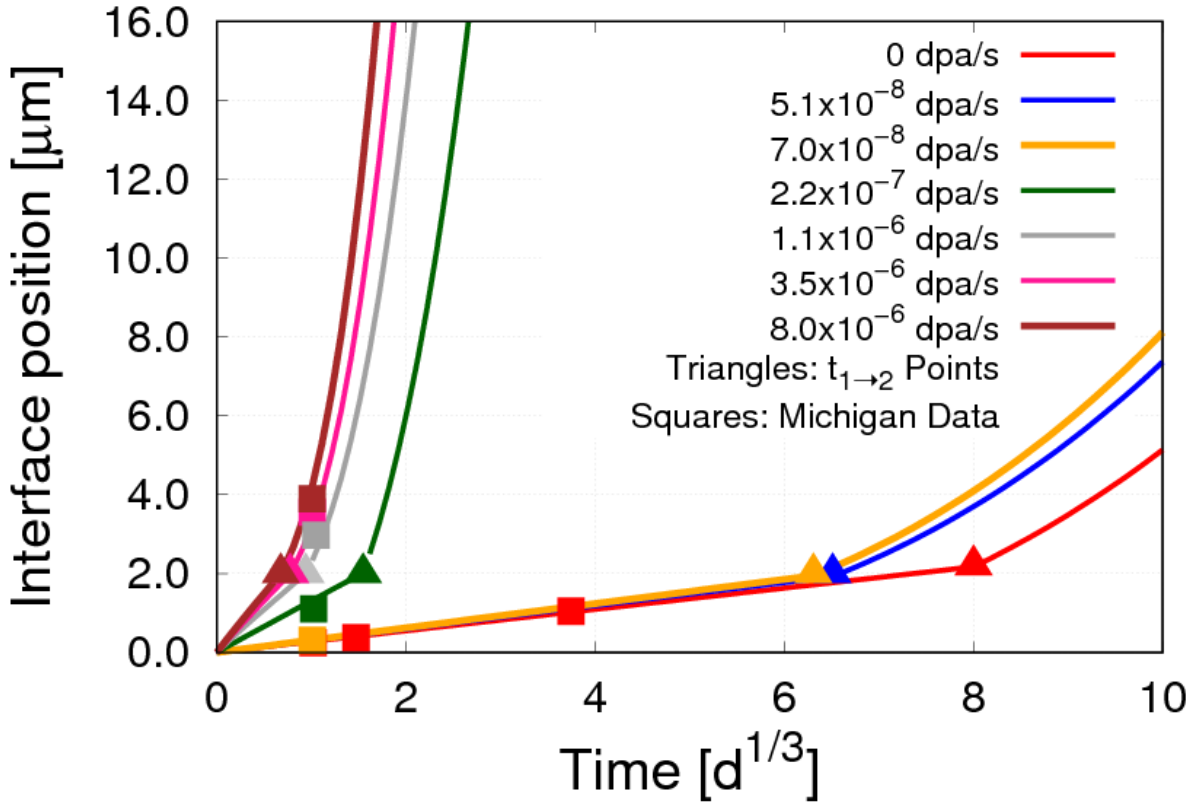

Figure 3-5: The variation of the oxide scale model predictions and associated experimental data (squares) [158] with dose rate. The colored triangles represent the Stage 2 transition at each dose rate.

thickness depends on time [50]. Figure 3-6 displays the corrosion rate as a function of dose rate. The growth rate is obtained by taking the derivative of s_1 for the corresponding dose rate followed by substituting a time equivalent to one day for consistency with the experimental conditions (zircaloy-4, exposed at 3 weight ppm H_2 for 24 hours at 320℃) [150]. The

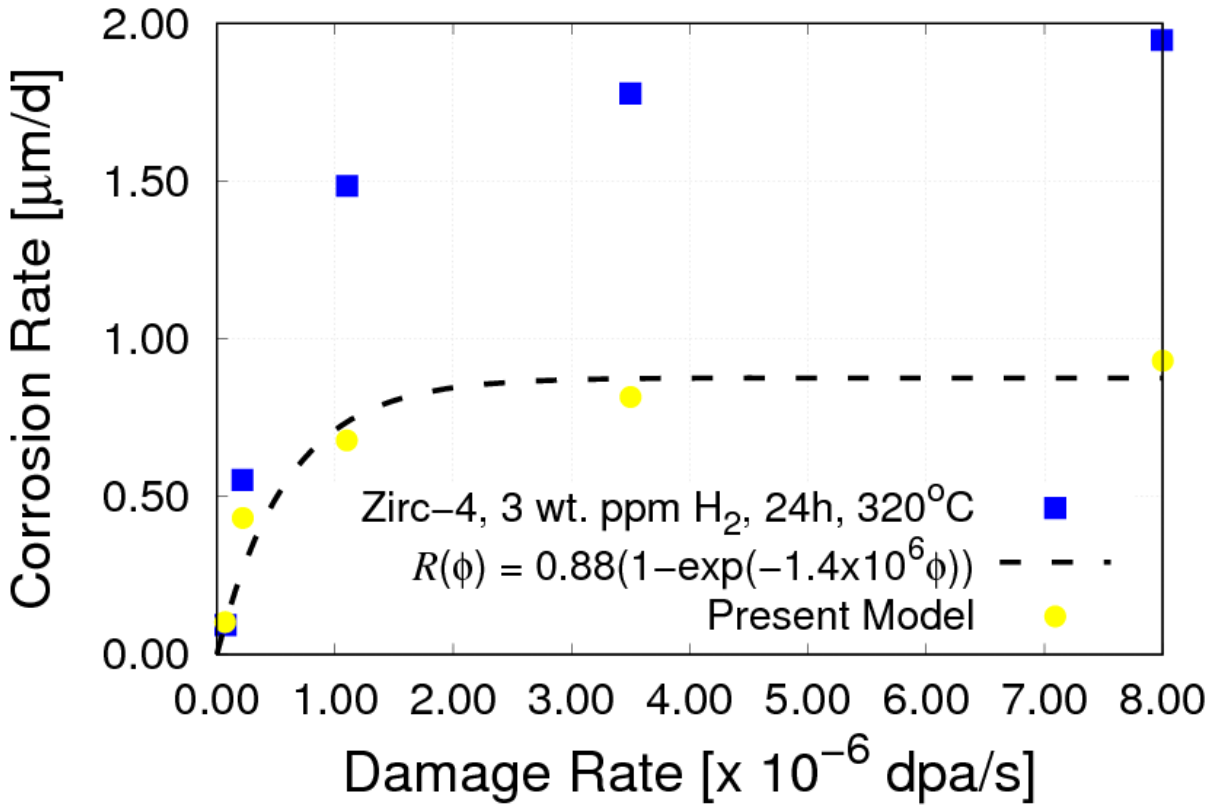

Figure 3-5: The variation of the oxide scale model predictions and associated experimental data (squares) [158] with dose rate. The colored triangles represent the Stage 2 transition at each dose rate.

University of Michigan data is denoted by the blue squares while the present model is denoted by the yellow circles. An exponential function similar to Wang and Was [150] has been used in the model. At lower dose rates (< $2.2x10^{-7}$ dpa·s^{-1}), the University of Michigan data is in agreement with the present model. However, discrepancies exist for dose rates at or above normal irradiation conditions because the data analysis from the University of Michigan data (from Figure 3-3) assumes that the oxide scale does not exhibit Stage 2 behavior at two microns. To be

consistent with corrosion rate profile from Figure 3-6, the growth rate should increase for only Stage 1 kinetics as a function of damage rate while it remains unchanged for Stage 2 growth. To

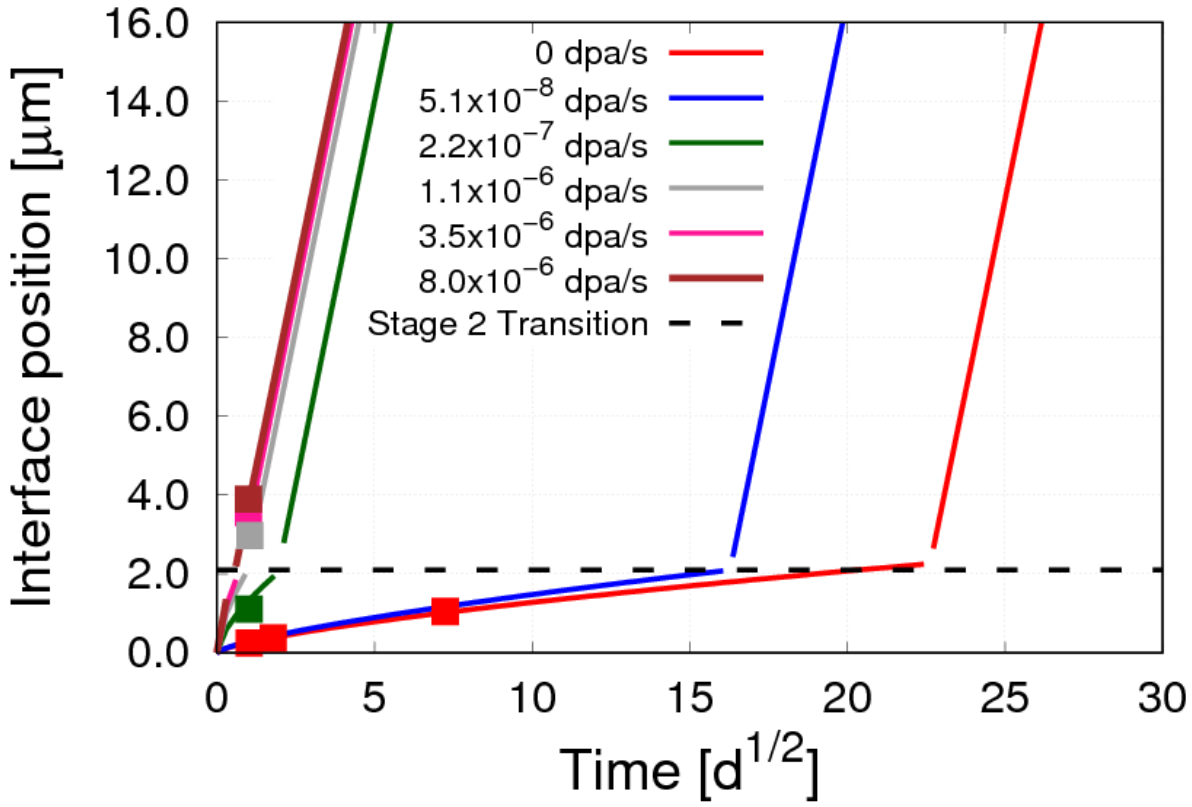

Figure 3-7: Re-plot of the irradiated oxide scale thickness for zircaloy-4 as a function of the square root of time with increasing damage rate. The square points represent the data from [158]. The dashed line represents the thickness of Stage 2 transition.

describe this concept, Figure 3-7 re-plots Figure 3-3 with transition at around two microns and a constant Stage 2 growth rate. The square points represent the data from [158] while the dashed line represents the thickness of Stage 2 transition.

3.3. Discussion of irradiation model results

The results from section 3.2 describe the potential for incorporating the effects of irradiation in zircaloy-4 oxidation. The key approach depends on applying the radiation

enhanced diffusion coefficients on the Stefan model described in section 2.1.3. First principles and (semi) phenomenological aspects are needed to calculate the key variables because the oxidation process with irradiation effects is complex. In addition, experimental data and conditions from the University of Michigan are the main sources for most parameters. The radiation enhanced diffusion (RED) uses a linear approximation at low dose rates because point defects primarily recombine [52]. Conversely, the RED utilizes a quadratic approximation at high dose rates because defects annihilate by recombination [55]. At normal irradiation conditions, the given experimental data for RED is used since the approximation is neither linear nor quadratic.

The radiation enhanced diffusivity (D_{ox}^{rad}), dose rate ($\dot{\varphi}$), $t_{1\rightarrow2}$, the oxide scale coefficient, and the growth rate are the relevant parameters for explaining the accelerated corrosion. From Table 3-2, larger diffusivities and larger growth law coefficients result from an increasing dose rate. From [49], the oxide growth rate is expected to augment by a factor of five times or more (specifically 10 times) than the non-irradiated case under proton irradiation; the present model produced a five-fold increase corrosion rate. In addition, the growth law coefficients have experienced a tenfold augmentation after the dose rate varies from 0 to $8.0\text{x}10^{-6}$ dpa/s. Furthermore, Stage 2 kinetics is accelerated with increasing damage rate for the original University of Michigan data. The corrosion rate is increased by five times with dose rate for the computational data while it is increased by ten times for the experimental data. The explanation for the discrepancy arises because Wang and Was has assumed that the oxide scale does not exhibit Stage 2 behavior at 2 microns for dose rates at or above normal irradiation conditions. Including a Stage 2 transition described by Motta et al [142] would result in accelerated corrosion at the higher dose rates. In addition, the accelerated Stage 1 kinetics and constant post-

transition kinetics would provide consistency between the oxide scale and growth rate evolutions with dose rate.

The exponent of oxide growth law is a parameter that merits a separate discussion. Under neutron exposure, the growth rate is expected to vary with a constant cubic exponent. Based on model results, the exponent remains approximately cubic but slightly reduces above dose rates under normal irradiation conditions. As described in [49], proton irradiation above 310℃ and neutron irradiation at temperature at 288^{o}C have similar properties such as dislocation microstructure, oxidation kinetics, irradiation creep, and localized deformation for proton and neutrons. The hardening parameter is one property that diverges because neutrons yield larger radiation hardening than protons [49]. Thus, the reduction of the exponent at high dose rate can be attributed to the proton's lower radiation hardening.

Finally, the RED model does not capture the effects of water chemistry and hydriding under irradiation. Based on different studies, water chemistry and delayed hydride cracking could accelerate Stage 2 behavior.

3.4. Conclusions of oxidation model with irradiation

Chapter 4 is ended with a list of the key conclusions for the RED model:

- A one-dimensional numerical oxidation model incorporates the effects of accelerated corrosion due to radiation enhanced diffusion.
- The RED assumes a linear approximation for low dose rates due to defect recombination while it assumes a quadratic approximation for high dose rates because of defect annihilation.
- The RED model is calibrated to exhibit the predicted Stage II behavior for each dose rate.

- The model parameterization includes both experimental and computational data consistent with Zircaloy-4 with no thermal gradient.
- The oxide growth rate increases fivefold as a function of damage rate.
- The lower radiation hardening in protons possibly decreases the exponent of the oxide scale as a function of dose rate.
- An increasing Stage 1 growth (up to 2 microns) and a constant Stage 2 growth rate are consistent with an asymptotic corrosion rate profile as a function of dose rate.

4. Chapter 4: Multilayer Hydriding

4.1. Hydride formation kinetics model

4.1.1. Overview of hydride formation

The hydride formation process begins with the oxide absorption of unreduced hydrogen ions; the protons then diffuse to the oxide-metal interface as described by the chemical reactions from 2.1.1 [6, 58]. A high hydrogen pickup fraction, with a power law variance as a function oxide thickness, could result in δ-hydrides precipitates in the zirconium metal [6]. After oxide absorption, the uniaxial tensile stress results in hydride formation through a circumferential or radial elongation [11, 59, 60]. For hydrides to form, the hydrogen concentration at the crack tip must exceed the terminal solid solubility for precipitation (TSSP) between temperatures of 513 K and 715 K [60, 63].

Delayed hydride cracking begins when the hydrogen accumulates in the direction of the tensile strain around the crack tip [59]. The stress concentration factor (K_I) eventually exceeds the hydride fracture toughness (K_{IH}) when the hydride reaches a critical size; consequently, fracture and crack propagation of the cladding initiate [60, 61, 65]. Due to stoichiometric zirconium hydride's "instability with respect to any tetragonal distortion", the increased stress and hydrogen flux in front of the crack activates crack propagation [59–61]. Before Stage 2 kinetics commences, the hydride blisters become more lenticular which indicate that the breakaway conditions occur after embrittlement due to the hoop stress [159]. As a result, the corrosion resistance of the zirconium cladding is reduced since the hydride disrupts the oxide formation of the metal-oxide interface [66].

4.1.2. Hydride formation kinetic model

In this section, the zirconium cladding oxidation kinetics accounts for the synergistic effects of hydrogen on oxygen transport and reaction. Prior to using the drift-diffusion equation for hydrogen diffusion, the model needs the positions for the ZrO_2/ZrO interface (s_1) and ZrO/metal interface (s_2) using zircaloy-4 parameters from Table 2-3 to serve as an input. Similar to the calculations from eqs. (24)–(26) and results from section 2.2.1, Figure 4-1 displays the evolution of the oxide scale with time. The model assumes a Stage 2 behavior of zircaloy-4 breaking down in the same manner as pure Zr instead of the cyclical reconstitution because hydriding occurs prior to breakaway [56].

In addition to the oxide lengths obtained from the Figure 4-1, the hydrogen diffusivities are prerequisites for better approximation for the hydrogen formation in the oxide. For simplicity, the calculation of hydrogen concentration by diffusion is separated into two steps to account for two instead of three layers assuming that the ZrO and ZrO_2 layers are merged to a single layer since the δ′ suboxide is less than 10% of the monoclinic oxide [85]. Therefore, the combination of the δ′ suboxide and monoclinic oxide is referred as the oxide for the hydride formation model only. The resulting drift-diffusion equation for hydrogen diffusion is:

$$\frac{\partial h_i}{\partial t} = \nabla(\mathrm{D_{Hi}}\nabla h) + \frac{\mathrm{U_i D_{Hi}}}{\mathrm{kT^2}}\nabla h_i \nabla T \qquad (31)$$

where i = I (metal layer), III (ZrO + ZrO_2 layer); the assumption has eliminated zone II, and the layer numbering remains the same to retain consistency with the oxidation model. Similar to eq. (6) described in section 2.1.3, eq. (31) carries a Fickian and thermo-migration contributions where h_i is the hydrogen concentration and D_{Hi} is the hydrogen diffusion coefficient; the other terms are identical to eq. (6). Additional assumptions are listed below: 1) the thermo-migration

term is zero since out-of-pile data is performed at a constant temperature (at 360℃ for the corrosion loop); 2) electro-migration is absent since protons diffuse much faster than the oxygen.

Even though the thickness of the metal remains fixed at 600 μm, a different form of the Stefan problem is necessary to track the hydride growth in the metal assuming that the hydride and metal are integrated into one layer. The length when the hydrogen concentration reaches zero for each time step represents the sum of the hydride thickness and the oxide-metal interface position. The maximum thickness corresponding to the entire span of the metal is:

$$s_h(t) = y(t)_{h=0} \tag{32}$$

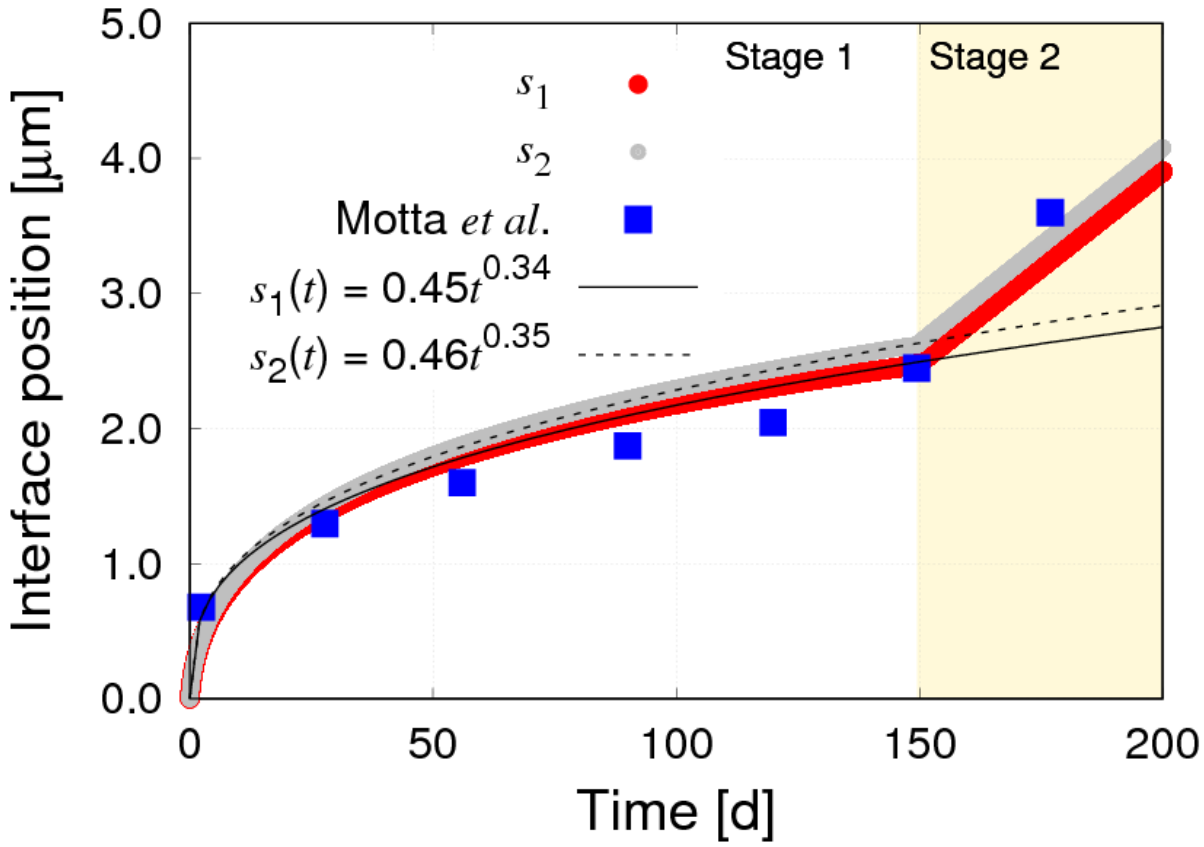

Figure 4-1: Time evolution of following two interfaces for zircaloy-4: s_1 (oxide scale thickness for ZrO_2) and s2 (thickness for the ZrO-metal interface). The shaded region to the right indicates the Stage 1 to Stage 2 transition where an abrupt increase in the oxide growth rate after Stage 2. The solid and dashed black lines denote the scale growth law fitted to the data for Stage 1. Experimental data from Ref. [142] is shown for comparison.

While all previous models have boundary conditions for constant hydrogen concentration, the use of a flux boundary condition has been proposed for the oxide layer since the hydrogen concentration at the oxide-metal interface is not constant; this variance is attributed to the increased hydrogen pickup as a function of oxide thickness [6]. However, a constant hydrogen concentration boundary condition in the metal for an instance in time is assumed because hydrogen diffusion is unimpeded in the metal. Equation (31) is subjected to the following dynamic boundary conditions:

$$h_I(y,0) = 0, y > s_H$$

$$h_I(0,t) = h_{III}(s(t),t) = H_0$$

$$h_{III}(y,0) = 0, y > s$$

$$J_{HIII}(0,t) = D_{HIII}\frac{\partial h_{III}(0,t)}{\partial y} = 2f_H\rho_{Zr}\frac{\partial s(t)}{\partial t}$$

where $s(t) = at^b$; $\frac{\partial s(t)}{\partial t} = abt^{b-1}$, J_{HIII} is the hydrogen flux in the oxide, f_H is the hydrogen fraction, *a* is the coefficient of the oxide power law, and *b* is the exponent of the power law.

4.1.3. Procedure for numerical solution

4.1.3.1. General numerical procedure for hydride formation

The procedure for the numerical solution is almost identical to the one presented in section 2.1.7 with the exception of eq. (23) having no thermo-migration and electro-migration contributions. The simplification eq (23) with Fickian only contribution for hydrogen diffusion is:

$$\frac{h_j^{i+1} - h_j^i}{\delta t} = D_{Hi}\left[\frac{h_{j+1}^i - 2h_j^i + h_{j-1}^i}{\delta y^2}\right] \quad (33)$$

which is solved for Zone I and Zone III (ZrO and ZrO_2 combined)

From the Neumann analysis described in 2.1.7, the numeric stability of the FTCS scheme is:

$$\frac{D_{Hi}\delta t}{\delta y^2} \leq \frac{1}{2}$$

From the above condition, the resulting Neumann stability criterion is:

$$\delta t \leq \frac{\delta y^2}{2D_{Hi}}$$

The discrete update step for the hydride thickness is:

$$s_h^i = y_j^i\left(h_j^i = 0\right) \tag{34}$$

4.1.3.2. Hydrogen resorption numerical model

At 600 K to 660 K, hydrogen absorption is increased due to the dissociation of the O-H bonds; in addition, the oxide layer does not fully inhibit hydrogen from desorbing away from the metal [67, 149]. Previously, Hu et al. [70] and Terrani et al. [72] proposed hydrogen resorption models that have concentration and pressure gradients; however, the equations are valid for temperatures above the TSSP (around 1033K). For non-gaseous hydrogen, Platt et al. [34] developed a hydrogen pickup model involving hydrogen fraction and the ratio between the oxide length and metal layer length. Incorporating Platt's formulation, the total hydrogen concentration is equal to the sum of concentrations obtained from the drift-diffusion equation and the hydrogen desorbed from the metal. The hydrogen concentration including the resorption is:

$$h_j^i = h_j^i + \frac{\delta y}{L - s(i-1)} h_j^{i-1} \tag{35}$$

Equation (35) can only formulate a numerical solution because the desorbed hydrogen is dependent on the oxide length due to the hydrogen concentration from the previous time step

being bound to the metal; the fraction is based on a flux balance. The δy represents the oxide thickness at the instant of the resorption and the $L - s(i - 1)$ signifies the thickness of the metal layer; the hydrogen fraction is absent in the equation since the boundary condition already accounts for this parameter. The calculation is post-processed since resorption is expected to minimally contribute to the total concentration.

4.1.4. Oxidation model parameterization

Parameterization of the hydride formation model is necessary to provide consistency and fidelity between the calculations and physics. In terms of hydride nucleation, the key parameters are the diffusivities of free hydrogen in the zircaloy-4 metal and in the monoclinic zirconia oxides, as well as the solubility limit of hydrogen in liquid phase. The following subsections will provide the values and sources of each key parameter. The model is isothermal since out-of-pile experiments such as corrosion loops operate at a constant temperature (at 360°C). Available experimental and numerical sources can help the model satisfy its needs while it lacks other data sets. Similar to the oxidation model, the first-principles calculations have the capabilities to obtain the hydrogen concentration at the oxide/metal interface to predict the formation of hydrides. Table 4-1 lists all parameters used in the hydriding model. The specific values and sources for each parameter are discussed in the following subsections.

4.1.4.1. Hydrogen diffusivity in metallic zircaloy-4

In principle, the diffusivity of hydrogen in Zircaloy-4 metal depends on temperature and concentration. Similar to the oxide model in the previous section, the Arrhenius equation is necessary to capture the temperature dependence; however, experimental means are required to

obtain the concentration dependence. The expression, statistically obtained by Kearns [160] for the through-thickness diffusivity of Zircaloy-4, is:

$$D_{HI}(T) = 7.90x10^{-7} exp\left(-\frac{0.47\ [eV]}{k_B T}\right)\ \ [m^2 \cdot s^{-1}]$$

where the activation energy is equivalent to 44,894 J/mol (10,730 cal/mol).

Table 4-1:
Physical parameters used in the model. The sources for each parameter are given in Section 4.1.4. The parameters δt and δy are obtained through calculations.

Property	Symbol	α-Zr (Zone I)	ZrO (Zone II)	ZrO2 (Zone III)
Diffusivity prefactor [$m^2 \cdot s^{-1}$]	D_{oH}	$7.90x10^{-7}$	$2.50x10^{-14}$	
Activation energy [eV]	U	0.47	0.35	
Time differential [s]	δt	$2.6x10^{-9}$	0.82	
Spatial differential [μm]	δy	0.13	0.13	

4.1.4.2. Hydrogen diffusivity in monoclinic ZrO_2

Hydrogen diffusivity in monoclinic zirconia has been measured started back in the late 1980s, with Smith providing results for temperatures above 596℃ [161] extracted from the data for pure Zr, is shown below:

$$D_{HIII}(T) = 1.13x10^{-12} exp\left(-\frac{1.04\ [eV]}{k_B T}\right)\ [m^2 \cdot s^{-1}]$$

while the data for Zr-2.5Nb measure the following:

$$D_{HIII}(T) = 3.05x10^{-13} exp\left(-\frac{0.56\ [eV]}{k_B T}\right)\ [m^2 \cdot s^{-1}]$$

where both diffusivities are in [$m^2 \cdot s^{-1}$] and the activation energies are in eV. Khatamian [162] has experimentally obtained the hydrogen diffusion coefficient in the oxide for pure Zr at a temperature range of 360–447°C shown below:

$$D_{HIII}(T) = 2.76x10^{-9} exp\left(-\frac{1.19\ [eV]}{k_B T}\right)\ [m^2 \cdot s^{-1}]$$

All of the obtained hydrogen diffusivities in the oxide are much slower than the ones in the metal since the oxide is a diffusion barrier to hydrogen. Tupin et al [163] have provided experimental data on hydrogen diffusivity in the monoclinic oxide for zircaloy-4 as described by the following expression:

$$D_{HIII}(T) = 2.50x10^{-14} exp\left(-\frac{0.35\ [eV]}{k_B T}\right)\ \ [m^2 \cdot s^{-1}]$$

where the activation energy is equivalent to 33,430 J/mol. The smaller pre-factor from Tupin [163] also accounts for the oxide's ability to inhibit hydrogen diffusion. From the assumption that the ZrO + ZrO_2 oxide layer is a single layer, the hydrogen diffusivity of the δ'-ZrO suboxide is the same as the monoclinic oxide.

4.1.4.3. Terminal solid solubility for precipitation (TSSP)

The parameter involved with solubility limit determines the terminal solid solubility for precipitation. TSSD occurs between 593 K and 793 K while TSSP is in a range of 513 K to 715 K [60, 63, 64]. As described in Figure 1-2, the phase is comprised of alpha zirconium and delta zirconium hydride when the hydrogen fraction is 1.0% at a temperature between 630 K and 660 K. From the corresponding phase, the terminal solid solubility for hydride nucleation is defined as

$$TSSP = 0.01 \cdot \rho_{Zr} = 4.31 \times 10^{26} [m^{-3}]$$

4.1.4.4. Hydrogen fraction

The hydrogen fraction, which is the parameter involved with hydrogen pickup, is the ratio of hydrogen absorbed by the oxide to the hydrogen yielded in the reduction reaction [6].

Even though this parameter varies with oxide thickness as a power law, Platt et al [6] has assumed a constant hydrogen fraction averaged for each zirconium sample to account for an isotropic volumetric expansion [6, 34]. While Platt [34] uses f_H = 0.2, Motta et al [6] provides a range between 0.2 and 0.25.

4.1.4.5. Boundary conditions and physical dimensions

The final set of parameters needed to run the hydride formation model defines the physical dimensions and boundary conditions of the model. Since no thermal gradient exists for out-of-pile experiments, the clad temperature is based on the water temperature in the out-of-pile tests (633 K). Other properties include the fitting parameters of the oxide. All these values are provided in Table 4-2.

Table 4-2:
Numerical parameters used in the hydride formation model.

a [μm·day^{-1}]	b [dimensionless]	T [K]	H_0 [m^{-3}]	TSSP [m^{-3}]	f_H [dimensionless]
0.45	0.34	633	1.56x10^{28}	4.31 x10^{26}	0.2

4.2. Hydride formation model results

The model has been explained in Section 4.1.2 to describing the process of hydride formation prior to Stages 2 in time and in space. Next, the main results as well as its relevance and validity are presented.

4.2.1. Hydrogen diffusion in the oxide

The section begins with the evolution of the hydrogen diffusion inside the clad (oxide layer) with depth at four distinct exposure times. The concentration profiles without hydrogen resorption, as depicted in Figure 4-2a, are obtained by solving the numerical hydrogen drift-

diffusion equation described in eq. (33) for the oxide layer. Each profile is color coded for its corresponding time. Given continuities in the mass fluxes, the moving interfaces from the Stefan problem generates mass discontinuities at the oxide-metal and oxide-water positions. The shaded areas represent the depth of the oxide (yellow) layer. As a note, the units of concentration are in terms of the atomic density of zirconium (ρ_{Zr}). Figure 4-2b shows the hydrogen concentration profiles with the addition of resorption. Since both Figures 4-2a and 4-2b are identical, the effect of the hydrogen resorption is minimal.

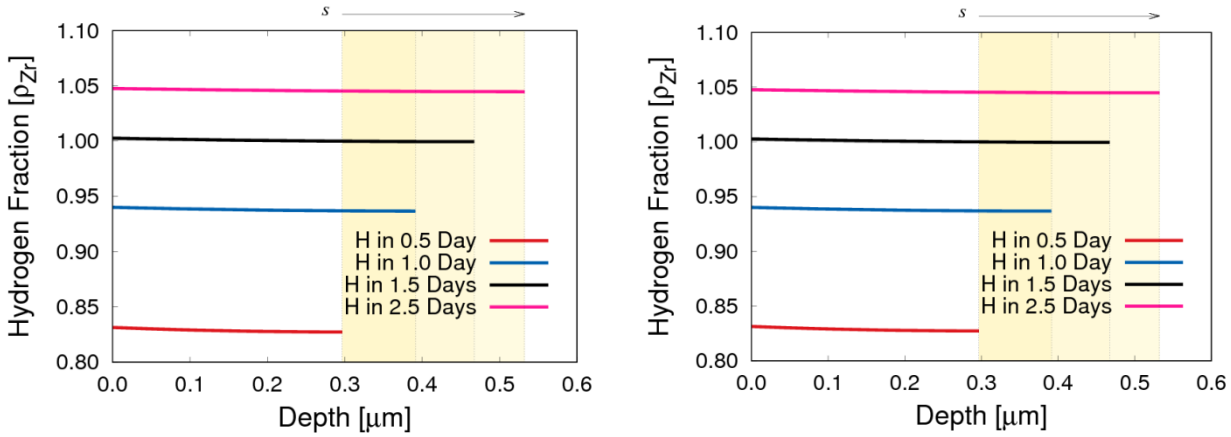

(a) Without resorption.

(b) With resorption

Figure 4-2: Total hydrogen concentration in the oxide as a function of depth at four different times expressed as a hydrogen fraction in units of ρ_{Zr}. The yellow shaded area represents the oxide thickness.

Next, the hydrogen penetration (or hydride population density) is studied at the oxide-metal interface as a function of time. The evolution of the concentration profile with time, as depicted in Figure 4-3a, is also derived from solving the numerical hydrogen drift-diffusion equation described in eq. (33); the units of concentration are in terms of the atomic density of zirconium (ρ_{Zr}). The yellow line denotes the terminal solid solubility for precipitation. At 633 K, the plot shows that the hydrogen penetration surpassing the TSSP is necessary to initialize hydride formation. In order to increase the resolution, the hydrogen profile at the oxide metal

interfaces is closely viewed between 0 and 0.004 days (0.10 hours). Figure 4-3b clearly shows the hydrogen concentration exceeds the TSSP in less than one tenth of an hour.

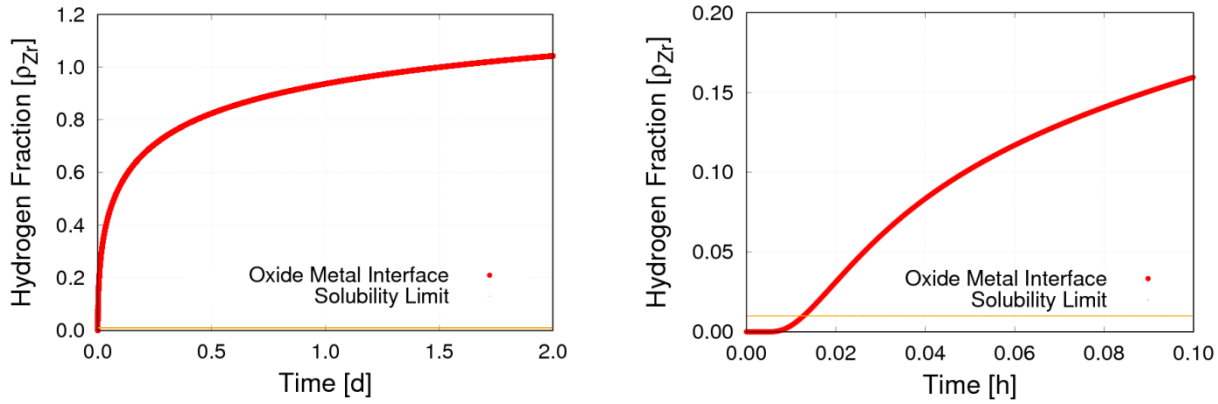

(a) Full size view

(b) Close-up view

Figure 4-3: Total hydrogen concentration at the oxide metal interface as a function of time in reference to the hydrogen solubility. The concentration is expressed as in units of ρ_{Zr}.

4.2.2. Hydride formation in zircaloy-4 metal

Due to highly discontinuous diffusivities in the oxide and metal, the depth evolution of the hydrogen penetration inside the metal layer is studied separately at four distinct exposure times. The concentration profiles, as depicted in Figure 4-4, are obtained by solving the same drift-diffusion equation used for the oxide layer; each profile is color coded for its corresponding time. Assuming a continuous mass at the oxide and hydride, the moving interfaces from the Stefan problem generates discontinuous mass fluxes in the oxide-hydride. The shaded areas represent the depth of the oxide (blue) and hydride (yellow) layers. As a note, the units of concentration are in terms of the atomic density of zirconium (ρ_{Zr}). The zero crossing of each concentration profile signifies the position of the hydride layer.

Tracking the time evolution of hydride position shows the growth of the hydride formation as a function of time; the hydride profile is displayed in Figure 4-5. The thickness of

the hydride layer is denoted by the value s_h; the curve exhibits quadratic behavior. The solid black line denotes the hydride power law ($s_h = a*t^n$) which indicates the constants

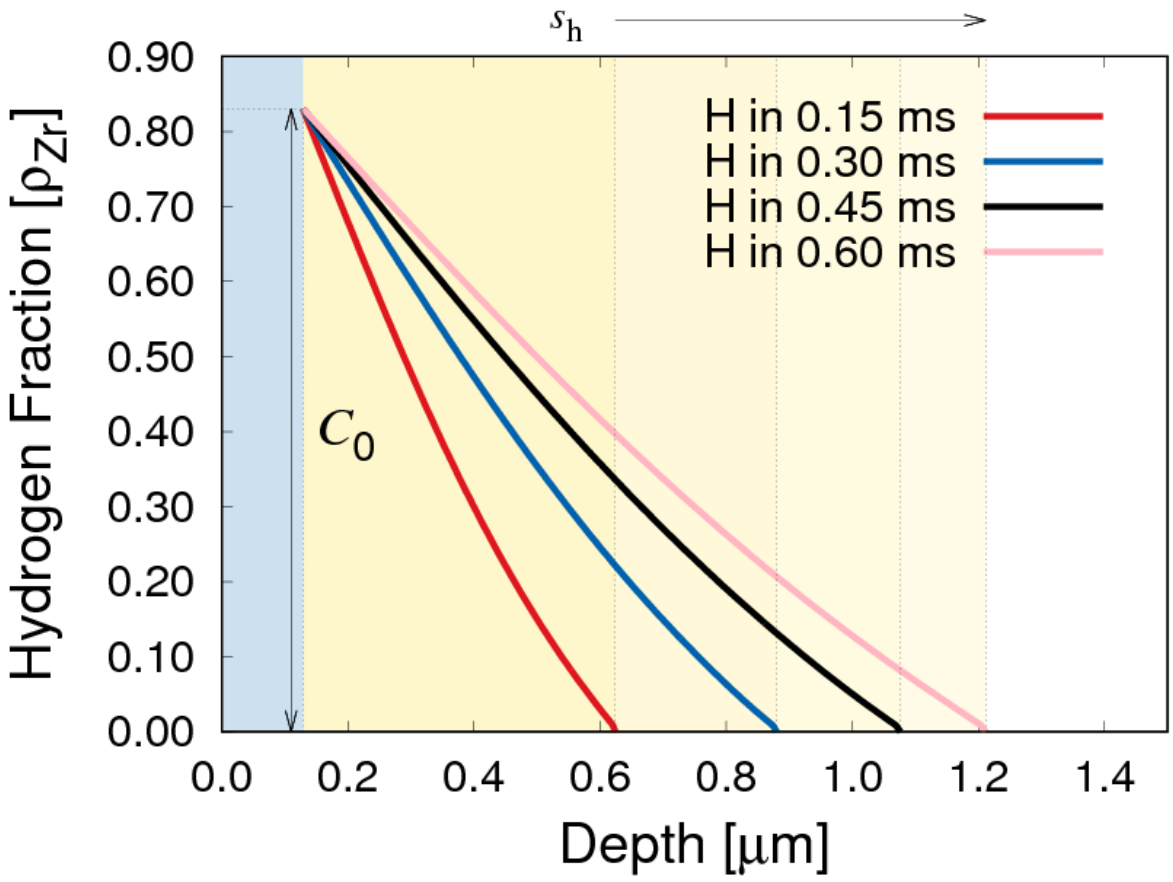

Figure 4-4: Total hydrogen concentration in the metal as a function of depth at four distinct times expressed as a hydrogen fraction in units of ρ_{Zr}. The shaded areas represent the thickness of the oxide (blue) and hydride (yellow) layers.

and exponents for each layer. The main features of our kinetic model are: (i) the hydride grows instantaneously with a power law of $s_h(t) = 1.34*t^{0.54}$ where s_h is in microns and t is in milliseconds.

4.3. Discussion of hydride formation model results

Hydride formation is the key phenomenon modeled in this work. The results described in the previous section shows a potential to model hydride formation given the input of oxide thickness and hydrogen flux. The approach is also based on a simplified Stefan problem tracking

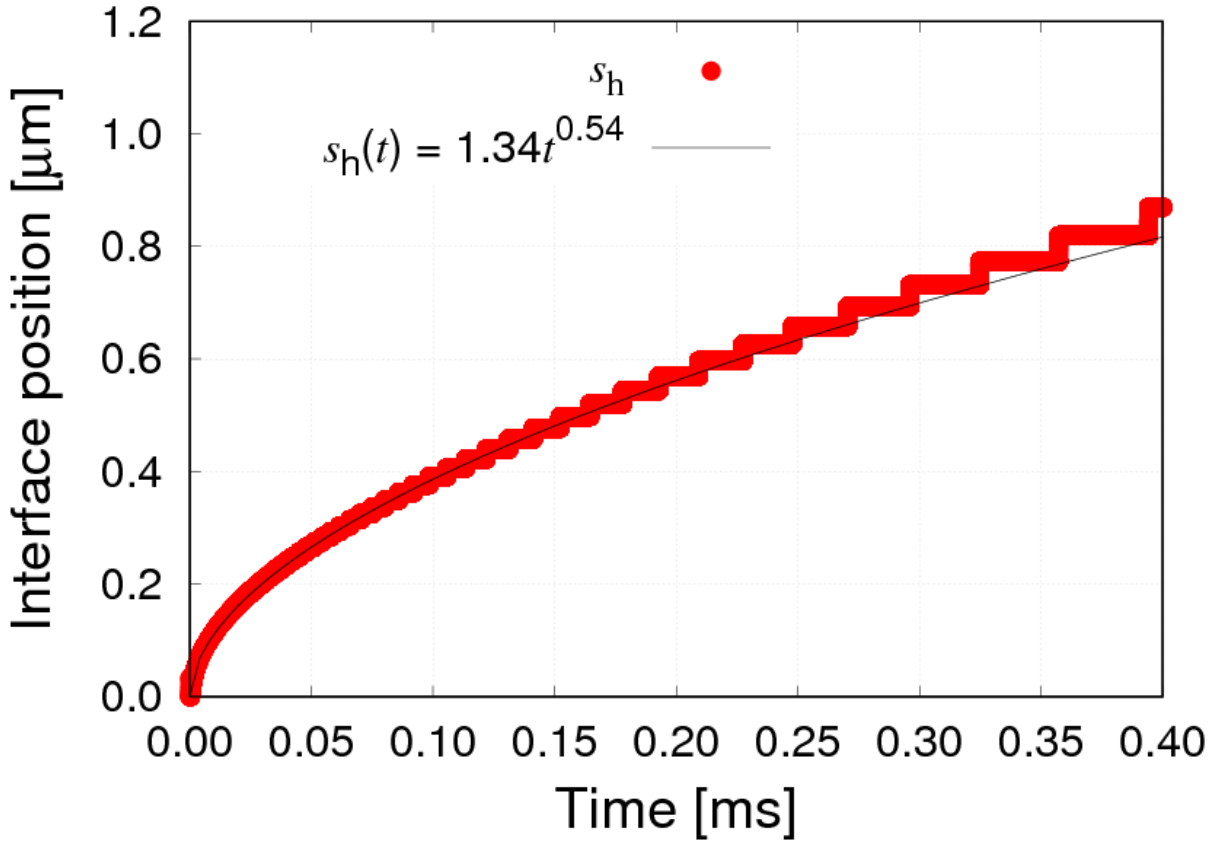

Figure 4-5: Time evolution of the hydride. The solid black lines denote the scale growth law fits to the data.

the growth of the hydride assuming an integrated hydride-metal layer. Separate drift diffusion equations are necessary to solve the Stefan problem because the oxide layer still forms a minimal hydrogen diffusion barrier [67, 159]. The vast difference between hydrogen diffusion from the hydrogen concentration profile in the oxide (Figure 4-2a) and the concentration profile in the metal (Figure 4-4) exhibits the capability of the oxide to inhibit hydrogen diffusion. By the time it reaches the metal, the hydrogen diffuses through an unimpeded medium resulting in an

instantaneous hydrogen accumulation and possible hydride formation [67, 159]. These results show that the diffusion of hydrogen in the oxide is the rate limiting step.

To simplify the numerical calculations of the equations, the model assumes the following: 1) the spatial dependence is only one-dimensional; 2) the hydrogen fraction is constant, 3) hydrogen, oxygen and zirconium are the only diffusing species and 4) no thermo-migration contribution is present. The first assumption is associated with the substoichiometric polycrystalline microstructure of the oxide as described in section 2.3. A constant hydrogen fraction was utilized to model an isotropic volumetric expansion of the hydride [34]. Having H, O and Zr to be the only chemical species is necessary to isolate the effects of hydride formation despite CRUD and water chemistry being involved in a light water reactor. Furthermore, the thermo-migration is absent because the autoclave experiments are preformed in constant temperature.

Two additonal features of the model are flux boundary conditions and hydrogen resorption. Motta et al [6] has postulated that the hydrogen concentration at the oxide-metal interface is not constant due to a varying hydrogen pickup as a function of oxide thickness. Since the model assumes a constant hydrogen function, a flux boundary condition has been incorporated in the water-oxide interface to account for a variable hydrogen concentration at the oxide-metal interface which is delineated from the results in Figures 4-2a and 4-3a. The minimum hydrogen concentration at the oxide-metal interface can serve as the initial concentration for the calculation of diffusion in the metal due to the very high diffusivity. Besides flux boundary conditions, hydrogen resorption needs to be included since hydrogen dissociates from the hydrides between 600 K and 660 K [67, 159]. Even though resorption is an important feature, its effect is almost nonexistent which can be confirmed by the almost identical results in Figures 4-2a and 4-2b.

In addition, the model has the potential to predict whether hydride formation is possible. In order to form hydrides, the hydrogen concentration at the oxide-metal interface (or crack tip) must exceed the terminal solid solubility for precipitation at temperatures between 513 K to 715 K [60, 63, 64]. The profiles from Figures 4-3a and 4-3b describe that the hydrogen concentration is larger than the TSSP in less than one hour. The data from Figure 4-5 confirm that the hydrides instantaneously form at the metal since the hydrogen diffusion becomes unimpeded.

In addition, the hydride formation formulation uses a combination of first-principles and (semi)phenomenological approaches. Including the sources of the parameters ranging from experimental data to calculations can allow solutions to relevant parameters and variables. However such key data, such as experimentally obtained hydride lengths, and comparable conditions can be elusive. From the Consortium for Advanced Simulation of Light Water Reactors (CASL) project, the research group from Oregon State University has been tasked to provide data sets for the hydride lengths using the same condition from the hydriding model while I provide the hydrogen concentration (or the population density of hydride) at the oxide/metal interface as a function of time. Unfortunately, the Oregon State group has since left the project before completing the data set.

Similar to the oxidation model, choosing an appropriate timescale and obtaining time synchronicity have been challenging because highly divergent hydrogen diffusivities in the oxide and in the metal has set time increments that need to satisfy the limits of the Neumann's stability analysis. To alleviate the issues regarding timescales, power laws are necessary to extrapolate the behavior beyond the model's time frame. In addition, the drift-diffusion equations need to be calculated separately for each layer with lookup tables and interpolation functions to impose synchronicity.

Finally, our model does not explicitly capture delayed hydride cracking and its effect on oxide kinetics. Previous studies from McRae et al [60] and Sagat et al [63] focused their models for delayed hydride cracking. Our emphasis so far has been to show that the hydrogen concentration at the oxide-metal interface exceeds the TSSP after oxide absorption and the hydride forms once the hydrogen reaches the metal. Although much work is necessary to fully understand the entire scope of the effects of hydrogen in nuclear environments, we have accomplished our primary emphasis.

4.4. Conclusions of hydride formation model

This chapter is ended with a list of the most relevant conclusions for the hydride formation model:

- A one-dimensional numerical model of hydride formation has been developed to track the hydrogen diffusion as it is absorbed by the oxide up to the hydride growth in the metal. The equations only involve a Fickian contribution because the autoclave experiments are performed at constant temperature.
- The hydride extension is coupled to the oxidation interface tracking model to follow hydrogen diffusion in the oxide and the metal. The model separately calculates the hydrogen drift diffusion equations in the following two layers to account for a large discontinuity in diffusivities: ZrO_2 + ZrO (outermost), and metallic Zr suboxides and solid-solutions (innermost).
- The model has been given a flux boundary condition at the water-oxide interface to generate a variable hydrogen concentration at the oxide-metal interface since the hydrogen fraction is assumed to be constant.

- A solubility limit criterion (or TSSP) based on zirconium-hydrogen phase diagram limits has been derived to determine a necessary condition of hydride nucleation and formation since hydrogen diffusion in the oxide is the rate-limiting step.
- The model is parameterized with both experimental and computational data consistent with Zircaloy-4, and it contains no temperature dependence.
- The model also accounts for hydrogen resorption since hydrogen dissociates from zirconium between 600 K and 660 K. However, our results show minimal effect on hydrides nucleation.
- Results show that hydride formation is possible when the hydrogen concentration exceeds the terminal solid solubility. In addition, the hydride grows instantaneously in the metal.

5. Appendix A: Analysis for justifying an exponentially-decaying charge density

The model can safely assume a maximum charge density in the vicinity of a chemical reaction site at the reaction site which gradually decreases towards zero as a function of distance away from the maximum (in the limit of an electro-neutral medium). Based on several works, an exponential decay has been suggested as the method for such a decrease [164, 165]. Here, an expression for the charge density has been derived that exhibits an exponential decay from simple kinetic considerations.

The imbalance between positively and negatively charged species can cause a charge accumulation near a moving corrosion reaction front. Assuming first-order kinetics, the rate to consume excess charge is given by:

$$\frac{d\rho}{dt} = -\alpha\rho \tag{A.1}$$

where ρ is the charge density and α is a proportionality constant. The time rate of change for the charge density in response to moving corrosion front with a velocity $v = dx/dt$, can also be expressed as:

$$\frac{d\rho}{dt} = \frac{d\rho}{dx} \cdot \frac{dx}{dt} = v\frac{d\rho}{dx} \tag{A.2}$$

Plugging eq. (A.1) to eq. (A.2) leads to:

$$\frac{d\rho}{dx} = -\frac{\alpha}{v}\rho \tag{A.3}$$

The charge rate of change with depth can be much slower than the local charge density variation despite the velocity of the oxidation front is time dependent. Consequently, the model assumes a constant velocity v for the advancing reaction front such that integration of eq. (A.3) results in:

$$\rho(x) = \rho_0.exp\left(-\frac{\alpha}{v}\right) \tag{A.4}$$

where ρ_0 is the charge density at the moving interface, and the $\frac{\alpha}{v}$ ratio represents the constant λ in Section 2.1.3.

6. Appendix B: Analysis for stability criterion

The Neumann stability criterion for linear differential equations with periodic boundary conditions provides the capability to produce a solution in a finite Fourier series. Even though each Fourier mode is defined by a corresponding wave number ω, each mode is tracked as a function of time assuming a solution of the form:

$$c_J^I = b(t_I) \cdot exp(iJ\omega\delta y) \tag{B.1}$$

where I and J represents the temporal and spatial indices, respectively to distinguish them from the complex variable i. Equation (B.1) is plugged in eq. (24) to transform into:

$$b^{I+1} \cdot exp(iJ\omega\delta y) = (1 - 2a_1 + a_5) \cdot b^I \cdot exp[iJ\omega\delta y] +$$

$$(1 + a_1 + a_2 + a_3 + a_4) \cdot b^I \cdot exp[i(J+1)\omega\delta y] +$$

$$(1 + a_1 + a_2 + a_3 + a_4) \cdot b^I \cdot exp[i(J-1)\omega\delta y] \tag{B.2}$$

where the coefficients a_1, a_2, a_3, a_4, and a_5 are constants in time and space. The Von Neumann's analysis is generally assumed to hold with slowly varying coefficients although it is not satisfied in conditions with variable temperature gradients.

Simplifying eq. (B.2):

$$b^{I+1} \cdot exp(iJ\omega\delta y) = (1 - 2a_1 + a_5) +$$

$$b^I \cdot exp[iJ\omega\delta y]\left[(1 + a_1 + a_2 + a_3 + a_4) \cdot exp[i\omega\delta y]\right] +$$

$$b^I \cdot exp[iJ\omega\delta y]\left[(1 + a_1 + a_2 + a_3 + a_4) \cdot exp[-i\omega\delta y]\right]$$

Further simplifications of the above equation yield:

$$\xi = \frac{b^{I+1}}{b^I} = 1 - 2a_1 + a_5 + (1 + a_1 + a_2 + a_3 + a_4) \cdot (exp[i\omega\delta y] + exp{-}i\omega\delta y \quad \text{(B.3)}$$

Since the relation $\exp(\pm i\omega\delta y) = \cos(\omega\delta y) \pm i \cdot \sin(\omega\delta y)$, eq. (B.3) can be expressed as

$$\xi = \frac{b^{I+1}}{b^I} = 1 - 2a_1 + a_5 + 2(1 + a_1 + a_2 + a_3 + a_4) \cdot cos(\omega\delta y) \quad \text{(B.4)}$$

The definition of the Neumann Stability Criterion is described as:

$$\xi^2 \leq 1 \quad \text{(B.5)}$$

$$\xi^2 = [1 - 2a_1 + a_5 + 2(1 + a_1 + a_2 + a_3 + a_4) \cdot cos(\omega\delta y)]^2 \quad \text{(B.6)}$$

The stability criterion based on the one of the extrema from trigonometric functions, $\omega\delta y = 0$, is simply

$$a_5 \leq 2a_1$$

while the other extrema represented by $\omega\delta y = \pi/2$ is:

$$a_5 \leq 2(a_2 + a_3 + a_4)$$

The results of both conditions are as follows:

$$a_2 + a_3 + a_4 \leq 1$$

Substituting for each coefficient expressions from Section 2.1.7, the stability criterion becomes:

$$\delta t \leq \frac{2kT}{D_{III}\left[\frac{U}{T}\left(\frac{dT}{dy}\right) + \frac{q\lambda(\rho(y) - \rho_0)}{\varepsilon}\right]} \delta y \quad \text{(B.7)}$$

7. References

[1] J. C. Scully, The fundamentals of corrosion. 2,1978.

[2] N. North, I. D. MacLeod, C. Pearson, Corrosion of metals, Butterworth-Heinemann, 1987.

[3] D. J. Young, High temperature oxidation and corrosion of metals, Vol. 1, Elsevier, 2008.

[4] P. Jacques, F. Lefebvre, C. Lemaignan, Deformation–corrosion interactions for zr alloys during i-scc crack initiation: part i: chemical contributions, Journal of nuclear materials 264 (3) (1999) 239–248.

[5] G.P. Sabol and G.D. Moan, eds., American Society for Testing and Materials: West Conshohocken, PA, 2000.

[6] A.T. Motta, A. Couet, and R.J. Comstock, Corrosion of zirconium alloys used for nuclear fuel cladding, Annual Review of Materials Research 45 (2015) 311–343.

[7] S. Kass, The development of the zircaloys, Symposium on Corrosion of Zirconium Alloys STP 368 (1964) 3–27.

[8] R.S. Shane, Nuclear power plant core materials and fabrication, Journal of Chemical Education 35 (11) (1958).

[9] D. Feron, Nuclear corrosion science and engineering, Woodhead Publishing, 2012.

[10] F. Cattant, D. Crusset, D. Féron, Corrosion issues in nuclear industry today, Materials Today 11 (10) (2008) 32 – 37.

[11] T.R. Allen, R.J.M. Konings, and A.T. Motta, 5.03 Corrosion of Zirconium Alloys, Comprehensive Nuclear Materials 5 (2012) 49–68.

[12] E. Hillner, Corrosion of zirconium-base alloys – an overview, Zirconium in the Nuclear Industry ASTM STP 633 (1977) 211–235.

[13] G.M. Ritcey, Crud in solvent extraction processing - a review of causes and treatment, Hydrometallurgy, 5 (1980) 97-107.

[14] K. A. Burrill, Corrosion product transport in water-cooled nuclear reactors, The Canadian Journal of Chemical Engineering 55 (1977) 54–61.

[15] A. Zaimovskii, Zirconium alloys in nuclear power, Atomic Energy 45 (6) (1978) 1165–1168.

[16] R. A. Causey, D. F. Cowgill, R. H. Nilson, Review of the oxidation rate of zirconium alloys, Tech. rep., Sandia National Laboratories (2005).

[17] B. Cox, Some thoughts on the mechanisms of in-reactor corrosion of zirconium alloys, Journal of Nuclear Materials vol. 336 (2) (2204) 331–368.

[18] A. T. Motta, A. Yilmazbayhan, M. J. G. da Silva, R. J. Comstock, G. S. Was, J. T. Busby, E. Gartner, Q. Peng, Y. H. Jeong, J. Y. Park, Zirconium alloys for supercritical water reactor applications: Challenges and possibilities, Journal of Nuclear Materials 371 (1) (2007) 61–75.

[19] P. Bossis, D. Pecheur, K. Hanifi, J. Thomazet, M. Blat, Comparison of the high burn-up corrosion on m5 and low tin zircaloy-4, in: 14th International Symposium on Zirconium in the Nuclear Industry, Vol. 3, 2006, pp. 494–525.

[20] R.J. Comstock, G. Schoenberger, and G.P. Sabol, Influence of processing variables and alloy chemistry on the corrosion behavior of ZIRLO nuclear fuel cladding", Zirconium in the Nuclear Industry ASTM STP 1295 (1996) 710–725.

[21] C. M. Eucken, P. T. Finden, S. Trapp-Pritsching, H. G. Weidinger, Influence of chemical composition on uniform corrosion of zirconium-base alloys in autoclave tests, in: Zirconium in the Nuclear Industry: Eighth International Symposium, ASTM International, 1989.

[22] R. A. Graham, J. P. Tosdale, P. T. Finden, Influence of chemical composition and manufacturing variables on autoclave corrosion of the zircaloys, in: zirconium in the nuclear industry: eighth international symposium, ASTM International, 1989.

[23] Z. Bangxin, L. Qiang, L. Wenqing, Y. Meiyi, C. Yuliang, The effects of water chemistry and composition on the microstructure evolution of oxide films on zirconium alloys during autoclave tests, Rare Metal Materials and Engineering 35 (7) (2006) 1009.

[24] D. Mogk, Gibbs' phase rule: Where it all begins, Integrating Research and Education, 2017, URL https://serc.carleton.edu/research_education/equilibria/phaserule.html

[25] P. Billot, A. Giordano, Comparison of zircaloy corrosion models from the evaluation of in-reactor and out-of-pile loop perfor mance, in: Zirconium in the Nuclear Industry: Ninth International Symposium, ASTM International, 1991.

[26] E. Hillner, D. Franklin, J. Smee, Long-term corrosion of zircaloy before and after irradiation, Journal of nuclear materials 278 (2) (2000) 334–345.

[27] X. Iltis, F. Lefebvre, and C. Lemaignan, Microstructural study of oxide layers formed on zircaloy-4 in autoclave and in reactor part I: Impact of irradiation on the microstructure of the zirconia layer, Journal of Nuclear Materials 224 (1995) 109–120.

[28] A. Yilmazbayhan, A.T. Motta, R.J. Comstock, G.P. Sabol, B. Lai, and Z. Cai, Structure of zirconium alloy oxides formed in pure water studied with synchrotron radiation and optical microscopy: Relation to corrosion rate, Journal of Nuclear Materials 324 (2004) 6–22.

[29] A. Denis, E. Moyano, E. A. Garcia, Model to simulate high temperature oxidation kinetics of zircaloy-4: Parabolic and linear behaviour, Journal of Nuclear Materials 110 (1) (1982) 11–19.

[30] J. A. Nesbitt, Numerical modeling of high-temperature corrosion processes, Oxidation of Metals 44 (1) (1995) 309–338. doi: 10.1007/BF01046731.

[31] B. Cheng, P. Gilmore, H. Klepfer, Pwr zircaloy fuel cladding corrosion performance, mechanisms, and modeling, in: Zirconium in the Nuclear Industry: Eleventh International Symposium, ASTM International, 1996.

[32] T. Arima, T. Masuzumi, H. Furuya, K. Idemitsu, Y. Inagaki, The oxidation kinetics and the structure of the oxide film on zircaloy before and after the kinetic transition, Journal of Nuclear Materials 294 (1?2) (2001) 148 – 153, 10th Int. Symp. on Thermodynamics of Nuclear Materials.

[33] V. Busser, J. Desquines, S. Fouquet, M. C. Baietto, J. P. Mardon, Modelling of corrosion induced stresses during zircaloy-4 oxidation in air, in: Materials Science Forum, Vol. 595, Trans Tech Publ, 2008, pp. 419–427.

[34] P. Platt, E. Polatidis, P. Frankel, M. Klaus, M. Gass, R. Howells, and M. Preuss, A study into stress relaxation in oxides formed on zirconium alloys, Journal of Nuclear Materials 456 (2015) 415-425.

[35] Review of theoretical conceptions on regimes of oxidation and hydrogen pickup in Zr-alloys.

[36] M. Steinbrück, J. Birchley, A. Goryachev, M. Grosse, T. Haste, Z. Hozer, A. Kisselev, V. Nalivaev, V. Semishkin, L. Sepold, et al., Status of studies on high-temperature oxidation and quench behaviour of zircaloy-4 and e110 cladding alloys, ERMSAR-2008, Nesseber, Bulgaria, Session S 2.

[37] M. Lindgren, I. Panas, On the fate of hydrogen during zirconium oxidation by water: effect of oxygen dissolution in [small alpha]-zr, RSC Adv. 4 (2014) 11050–11058. doi:10.1039/C4RA00020J.

[38] F. Garzarolli, H. Seidel, R. Tricot, J. Gros, Oxide growth mechanism on zirconium alloys, in: Zirconium in the Nuclear Industry: Ninth International Symposium, ASTM International, 1991.

[39] L. Zhang, D. D. Macdonald, E. Sikora, J. Sikora, On the kinetics of growth of anodic oxide films, Journal of The Electrochemical Society 145 (3) (1998) 898–905. doi:10.1149/1.1838364.

[40] G. H. M. Birks, N., F. S. Pettit, Introduction to the high-temperature oxidation of metals, Cambridge University Press, New York, 2006.

[41] A. Saillard, Modeling and simulation of stress-induced non-uniform oxide scale growth during high-temperature oxidation of metallic alloys, Ph.D. thesis, Georgia Institute of Technology 5 (2010).

[42] A. Almarshad, A. Klein, A model for waterside oxidation of zircaloy fuel cladding in pressurized water reactors, Journal of Nuclear Materials 183 (3) (1991) 186 – 194. doi:http://dx.doi.org/10.1016/0022-3115(91)90487-R.

[43] J. Belle, M. Mallett, Kinetics of the high temperature oxidation of zirconium, Journal of the Electrochemical Society 101 (7) (1954) 339–342.

[44] E. Gulbransen, K. Andrew, Oxidation of zircaloy-2 and -3a at 300 to 850 c, Trans. Met. Soc. AIME Vol: 212.

[45] H. A. Porte, J. G. Schnizlein, R. C. Vogel, D. F. Fischer, Oxidation of zirconium and zirconium alloys 107 (6) (1960) 506–515. doi:10.1149/1.2427733.

[46] P. Gondi, G. F. Missigolli, Electron microscope observations on the oxidation of zirconium. a contribution to the cubic kinetic theory., Il Nuovo CImento XLVIII B (2) (1967) 223–236.

[47] P. Tejland, H.-O. Andrén, Origin and effect of lateral cracks in oxide scales formed on zirconium alloys, Journal of Nuclear Materials 430 (1) (2012) 64–71.

[48] S.S. Raiman, A. Flick, O. Toader, P. Wang, N.A. Samad, Z. Jiao and, G.S. Was, A facility for studying irradiation accelerated corrosion in high temperature water, Journal of Nuclear Materials 451 (2014) 40–47.

[49] G.S. Was, Challenges to the use of ion irradiation for emulating reactor irradiation, Journal of Material Research 30 (9) (2015) 1158–1182.

[50] P. Wang and G.S. Was, Oxidation of zircaloy-4 during in situ proton irradiation and corrosion in PWR primary water, Journal of Material Research 30 (9) (2015) 1335–1348.

[51] G.S. Was, Fundamentals of radiation material science: Metals and alloys, New York: Springer-Verlag, Second Edition, 2016.

[52] G.J. Dienes and A.C. Damask, Radiation enhanced diffusion in solids, Journal of Applied Physics 29 (12) (1958) 1713–1721.

[53] O.T. Woo, G.M. McDougall, R.M. Hutcheon, V.F. Urbanic, M. Griffiths, and C.E. Coleman, Corrosion of electron-irradiated Zr-2.5Nb and zircaloy-2, Zirconium in the Nuclear Industry: Twelfth International Symposium ASTM STP 1354 (2000).

[54] X.T. Zu, K. Sun, M. Atzmon, L.M. Wang, L.P. You, F.R. Wan, J.T. Busby, G.S. Was, and R.B. Adamson, Effect of proton and Ne irradiation on the microstructure of zircaloy 4, Philosophical Magazine 85 (4–7) (2005) 649–659.

[55] R.S. Averback and H. Hahn, Radiation-enhanced diffusion in amorphous Ni-Zr alloys, Rapid Communications 37 (17) (1988) 10383-10386.

[56] A. Zielinski and S. Sobieszczyk, Hydrogen-enhanced degradation and oxide effects in zirconium alloys for nuclear applications, International Journal of Hydrogen Energy 36 (2011) 8619–8629.

[57] M.S. Veshchunov and A.V. Berdyshev, Modelling of hydrogen absorption by zirconium alloys during high temperature oxidation in steam, Journal of Nuclear Materials 255 (1998) 250–262.

[58] K.N. Choo, S.I. Pyun, and Y.S. Kim, Oxidation and hydrogen uptake of Zr-based Nb alloys at 400°C under 10 MPa H_2O steam atmosphere, Journal of Nuclear Materials 226 (1995) 9–14.

[59] G. J. Ackland, Embrittlement and the bistable crystal structure of zirconium hydride, Physical Review Letters 80 (10) (1997) 2233–2236.

[60] G.A. McRae, C.E. Coleman and B.W. Leitch, The first step for delayed hydride cracking in zirconium alloys, Journal of Nuclear Materials 396 (2010) 130–143.

[61] S.Q. Shi, M. Liao and M.P. Puls, Modelling of time-dependent hydride growth at crack tips in zirconium alloys, Modelling Simul. Mater. Sci. Eng. 2 (1994) 1065–1078.

[62] N. Dupin, I. Ansara, C. Servant, C. Toffolon, C. Lemaignanc, and J.C. Brachet, "A thermodynamic database for zirconium alloys, Journal of Nuclear Materials 275 (1999) 287–295.

[63] S. Sagat, C.K. Chow, M.P. Puls and C.E. Coleman, Delayed hydride cracking in zirconium alloys in a temperature gradient, Journal of Nuclear Materials 279 (1999) 107–117.

[64] O. Zanellato, M. Preuss, J.Y. Buffiere, F. Ribeiro, A. Steuwer, J. Desquines, J. Andrieux, and B. Krebs, Synchrotron diffraction study of dissolution and precipitation kinetics, Journal of Nuclear Materials 420 (2011) 537–547.

[65] S.Q. Shi and M.P. Puls, Fracture strength of hydride precipitates in Zr-2.5Nb alloys, Journal of Nuclear Materials 275 (1999) 312–317.

[66] A.M. Gardd, Enhancement of aqueous corrosion of zircaloy-4 due to hydride precipitation at the metal-oxide interface, Zirconium in the Nuclear Industry: Ninth International Symposium, ASTM STP 1132 (1991) pp.566–594.

[67] W. Chen, L. Wang, and S. Lu, Influence of oxide layer on hydrogen desorption from zirconium hydride, Journal of Alloys and Compounds 469 (2008) 142–145.

[68] Y. Shinohara, H. Abe, T. Iwai, N. Sekimura, T. Kido, H. Yamamoto, and T. Taguchi, In situ TEM observation of growth process of zirconium hydride in zircaloy 4 during hydrogen ion implantation, Journal of Nuclear Science and Technology 46 (6) (2009) 564–571.

[69] D. Xu and H. Xiao, Cluster dynamics model for the hydride precipitation kinetics in zirconium cladding", Proceedings of the 18th International Conference on Environmental Degradation of Materials in Nuclear Power Systems – Water Reactors (2017) 543–552.

[70] X. Hu, K.A. Terrani, and B.D. Wirth, Hydrogen desorption kinetics from zirconium hydride and zirconium metal in vacuum, Journal of Nuclear Materials 448 (2014) 87 – 95.

[71] J. Huang, B. Tsuchiya, Kenji Konashi, and M. Yamawaki, Estimation of hydrogen redistribution in zirconium hydride under temperature gradient, Journal of Nuclear Science and Technology 37 (10) (2000) 887–892.

[72] K.A. Terrani, M. Balooch, D. Wongsawaeng, S. Jaiyen, and D.R. Olander, "The Kinetics of Hydrogen Desorption from and Adsorption on Zirconium Hydride", Journal of Nuclear Materials, vol. 397, pp. 61 – 68, 2010.

[73] C.C. Lin, A review of corrosion product transport and radiation field buildup in boiling water reactors, Progress in Nuclear Energy 51 (2008) 207–224.

[74] D.H Lister, Corrosion products in power generating systems (No. AECL—6877), Atomic Energy of Canada Ltd., 1980.

[75] D.H. Lister, R.D. Davidson and E. McAlpine, The mechanism and kinetics of corrosion product release from stainless steel in lithiated high temperature water, Corrosion Science, 27 (2) (1987) 113–140.

[76] J. Henshaw, J.C. McGurk, H.E. Sims, A. Tuson, S. Dickinson, and J. Deshon, A model of chemistry and thermal hydraulics in PWR fuel clad depositis, Journal of Nuclear Materials 353 (2005) 1–11.

[77] J.A. Sawicki, Analyses of crud deposits on fuel rods in PWRs using mössbauer spectroscopy", Journal of Nuclear Materials 402 (2010) 124–129.

[78] M. Bojinov, V. Karastoyanov, P. Kinnunen, and T. Saario, Influence of water chemistry on the corrosion mechanism of a zirconium–niobium alloy in simulated light water reactor coolant conditions, Corrosion Science 52 (2009) 54–67.

[79] D. Pecheur, J. Godlewski, J. Peybernes, L. Fayette, M Noe, A. Frichet, and O. Kerrec, Contribution to the understanding of the effect of the water chemistry on the oxidation

kinetics of zircaloy-4 cladding, Zirconium in the Nuclear Industry: Twelfth International Symposium ASTM STP 1354 (2000) 793–811.

[80] Frattini, P. L., J. Blok, S. Chauffriat, J. Sawichi, and J. Riddle, Axial offset anomaly: coupling PWR primary chemistry with core design, Water chemistry of nuclear reactor systems 1 (2000) 24-33.

[81] J.P. Abriata, J. Garcés, The O-Zr (oxygen-xirconium) system, Bulletin of Alloy, Phase Diagrams 7 (2) (1986) 116–124.

[82] E.G. Rauh, S.P. Garg, The ZrO_{2-x} (cubic)-ZrO_{2-x} (cubic + tetragonal) phase, boundary, J. Am. Ceram. Soc. 63 (1980) 239–240.

[83] E. Gebhardt, H.D. Seghezzi, W. Durrschnabel, Research on the system zirconium-oxide, J. Nucl. Mater. 4 (1961) 255–268.

[84] B. Puchala, and A. Van der Ven, Thermodynamics of the Zr-O system from first-principles calculations, Physical Review B88 (094108) (2013) 1–15.

[85] Y. Dong, A.T. Motta, and E.A. Marquis, Atom probe tomography study of alloying element distributions in Zr alloys and their oxides, Journal of Nuclear Materials 442 (2013) 270–281.

[86] R.J. Nicholls, N. Ni, S. Lozano-Perez, A. London, D.W. McComb, P.D. Nellist, C.R. Grovenor, C.J. Pickard, J.R. Yates, Crystal structure of the ZrO phase at zirconium/zirconium oxide interfaces, Adv. Eng. Mater. 17 (2) (2015) 211-215.

[87] K.J. Annand, I. MacLaren, M. Gass, Utilising dual eels to probe the nanoscale mechanisms of the corrosion of zircaloy-4 in 350°c pressurised water, J. Nucl. Mater. 465 (2015) 390–399.

[88] Corrosion of Zirconium Alloys in Nuclear Power Plants, Tech. Rep. IAEA-tecdoc-684, International Atomic Energy Agency, 1993.

[89] R.C. Garvie, R.H. Hannik, R.T. Pascoe, Ceramic steel, Nature 258 (1975) 703–704.

[90] J. Godlewski, How the Tetragonal Zirconia Is Stabilized in the Oxide Scale that Is Formed on a Zirconium alloy Corroded at 400° C in Steam, ASTM International, West Conshohocken, PA, 1994663–683.

[91] R.C. Garvie, Ceramic steel?, J. Phys. Chem. 69 (1965) 1238–1243.

[92] M.W. Pitcher, S.V. Ushakov, A. Navrotsky, B.F. Woodfield, G. Li, J. Boerio- Goates, B.M. Tissue, Energy crossovers in nanocrystalline zirconia, J. Am. Ceram. Soc. 88 (1) (2005) 160–167.

[93] A. Garner, A. Gholinia, P. Frankel, M. Gass, I. MacLaren, M. Preuss, The microstructure and microtexture of zirconium oxide films studied by transmission electron backscatter

diffraction and automated crystal orientation mapping with transmission electron microscopy, Acta Mater. 80 (2014) 159–171.

[94] G.S. Frankel, Fundamentals of corrosion kinetics, In: A.E. Hughes, J.M. Mol, M.L. Zheludkevich, R.G. Buchheit (Eds.), Active Protective Coatings: New-generation Coatings for Metals, vol. 233, Springer Series in Materials Science, 2016, Ch. 2.

[95] H. Steiner, J. Konys, Stresses in Oxidized Claddings and Mechanical Stability of Oxide Scales, Tech. Rep. FZKA 7191, Forschungszentrum Karlsruhe, 2006.

[96] J. Chevalier, L. Gremillard, A.V. Virkar, D.R. Clarke, The tetragonal-monoclinic transformation in zirconia: lessons learned and future trends, J. Am. Ceram Soc. 92 (9) (2009) 1901–1920.

[97] E.D. Whitney, Kinetics and mechanism of the transition of metastable tetragonal to monoclinic zirconia, Trans. Faraday Soc. 61 (1965) 1991–2000.

[98] B.X. Zhou, Q. Li, M.Y. Yao, W.Q. Liu, and Y.L. Chu, Effect of water chemistry and composition on microstructural evolution of oxide on Zr alloys", Journal of ASTM International 5 (2) (2008) 360–383.

[99] The reaction of oxygen and zirconium, Thermochim. Acta 84 (1985) 357–365.

[100] A. Aryanfar, J. Thomas, A. Van der Ven, D. Xu, M. Youssef, J. Yang, B. Yildiz, J. Marian, Integrated computational modeling of water side corrosion in zirconium metal clad under nominal lwr operating conditions, JOM (J. Occup Med.) 68 (11) (2016) 2900–2911.

[101]Rubinshteĭn, The stefan problem, American Mathematical Soc., 2000.

[102] J. Cannon and M. Primicerio, Remarks on the one-phase stefan problem for the heat equation with the flux prescribed on the fixed boundary, Journal of Mathematical Analysis and Applications 35 (2) (1971) 361–373.

[103] A. Crowley, "On the weak solution of moving boundary problems, IMA Journal of Applied Mathematics 24 (1979) 43–57.

[104] K. Michel, V. Ozolins, Theory of mass transport in sodium alanate, J. Mater. Chem. 2 (2014) 4438.

[105] G.D. Rieck, H.A.C.M. Bruning, Thermal diffusion of oxygen and nitrogen in zirconium, Nature 190 (1961) 1181–1182.

[106] T.-W. Chiang, A. Chernatynskiy, M.J. Noordhoek, S.B. Sinnott, S.R. Phillpot, Anisotropy in oxidation of zirconium surfaces from density functional theory calculations, Comput. Mater. Sci. 98 (2015) 112–116.

[107] A. Couet, A.T. Motta, and A. Ambard, The coupled current charge compensation model for zirconium alloy fuel cladding oxidation: Parabolic oxidation of zirconium alloys, Corrosion Science, 100 (2015) 73–84.

[108] G. Eloff, C. Greyling, P. Viljoen, The role of space charge in the oxidation of zircaloy-4 between 350 and 450Â°c in air, J. Nucl. Mater. 199 (3) (1993) 285–288.

[109] H.J. Beie, A. Mitwalsky, F. Garzarolli, H. Ruhmann, H.-J. Sell, Examinations of the corrosion mechanism of zirconium alloys, In: Zirconium in the Nuclear Industry: Tenth International Symposium, ASTM International, 1994.

[110] B. Bell, S. Murphy, P. Burr, R. Comstock, J. Partezana, R. Grimes, M. Wenman, The influence of alloying elements on the corrosion of zr alloys, Corrosion Sci. 105 (2016) 36–43.

[111] B. Bell, S. Murphy, R. Grimes, M. Wenman, The effect of nb on the corrosion and hydrogen pick-up of zr alloys, Acta Mater. 132 (2017) 425–431

[112] M. Mamivand, M.A. Zaeem, H.E. Kadiri, L.-Q. Chen, Phase field modeling of the tetragonal-to-monoclinic phase transformation in zirconia, Acta Mater. 61 (14) (2013) 5223–5235.

[113] P. Platt, P. Frankel, M. Gass, R. Howells, M. Preuss, Finite element analysis of the tetragonal to monoclinic phase transformation during oxidation of zirconium alloys, J. Nucl. Mater. 454 (1) (2014) 290–297.

[114] H. Evans, R. Lobb, Conditions for the initiation of oxide-scale cracking and spallation, Corrosion Sci. 24 (3) (1984) 209–222.

[115] J. Armitt, R. Holmes, M. Manning, D. Meadowcroft, E. Metcalfe, Spalling of Steam-grown Oxide from Superheater and Reheater Tube Steels. Technical Planning Study 76-655, final report, Tech. rep Central Electricity Research Labs., Leatherhead (UK), 1978.

[116] N. Tang, A. Plumtree, Cavity nucleation in creep, Scripta Metallurgica 18 (10) (1984) 1045–1049.

[117] J.N. Wanklyn, C.F. Britton, D.R. Silvester, and N.J.M. Wilkins, Influence of environment on the corrosion of zirconium and its alloys in high-temperature steam, Journal of the Electrocchemical Society 110 (8) (1963) 856–866.

[118] What is wrong with current models for in-reactor corrosion, in: Fundamental Aspects of Corrosion on Zirconium Base Alloys in Water Reactor Environments.

[119]J. P. Pemsler, Diffusion of oxygen in zirconium and its relation to oxidation and corrosion, Journal of The Electrochemical Society 105 (6) (1958) 315–322.

[120] I. Ritchie, A. Atrens, The diffusion of oxygen in alpha-zirconium, J. Nucl. Mater. 67 (3) (1977) 254–264.

[121]T. Smith, Diffusion coefficients and anion vacancy concentrations for the zirconium-zirconium dioxide system, Journal of the Electrocchemical Society 112 (6) (1965) 560–567.

[122] C.O.D. Gonzalez, E.A. Garcia, Determination of the diffusion coefficients of oxygen in zirconium by means of XPS, Applied Surface Science, 44(3), 211-219.

[123] A. Madeyski, W. Smeltzer, Oxygen diffusion in monoclinic zirconia, Mater. Res. Bull. 3 (4) (1968) 369–375.

[124] D.J. Poulton, W.W. Smeltzer, Oxygen diffusion in monoclinic zirconia, J. Electrchem Soc. 117 (3) (1970) 378–381.

[125] F.J. Keneshea, D.L. Douglass, The diffusion of oxygen in zirconia as a function of oxygen pressure, Oxid. Metals 3 (1) (1971) 1–14.

[126] B. Cox and J.P. Pemsler, "Diffusion of oxygen in growing zirconia films, Journal of Nuclear Materials 28 (1968) 73–78.

[127]J. Fink, and L. Leibowitz, Thermal conductivity of zirconium, Journal of Nuclear Materials 226 (1995) 44 – 50.

[128] P. Klemens, Thermal conductivity of zirconia, Thermal Conductivity 23 (1996) 209–220.

[129] B. Nait-Ali, K. Haberko, H. Vesteghem, J. Absi, and D. Smith, Thermal conductivity of highly porous zirconia, Journal of the European Ceramic Society 26 (16) (2006) 3567 – 3574.

[130] S. Gu, T.J. Lu, D.D. Hass, and H.N.G. Wadley, Thermal conductivity of zirconia coatings with zig-zag pore microstructures, Acta mater. 49 (2001) 2539–2547.

[131] J. Chang, Y.-S. Lin, Dielectric property and conduction mechanism of ultrathin zirconium oxide films, Appl. Phys. Lett. 79 (22) (2001) 3666–3668.

[132] K. Kukli, K. Forsgren, M. Ritala, M. Leskelä, J. Aarik, A. Haårsta, Dielectric properties of zirconium oxide grown by atomic layer deposition from iodide precursor, J. Electrochem. Soc. 148 (12) (2001) F227–F232.

[133] M. Houssa, V. Afanasev, A. Stesmans, M. Heyns, Variation in the fixed charge density of sio x/zro 2 gate dielectric stacks during postdeposition oxidation, Appl. Phys. Lett. 77 (12) (2000) 1885–1887.

[134] N. Maity, R. Maity, R. Thapa, S. Baishya, Study of interface charge densities for zro2 and hfo2 based metal-oxide-semiconductor devices, Adv. Mater. Sci. Eng. (2014).

[135] P. Aldebert, J.P. Traverse, Structure and ionic mobility of zirconia at high temperature, J. Am. Ceram. Soc. 68 (1) (1985) 34–40.

[136] S.-K. Chan, Y. Fang, M. Grimsditch, Z. Li, M.V. Nevitt, W.M. Robertson, E.S. Zouboulis, Temperature dependence of the elastic moduli of monoclinic zirconia, J. Am. Ceram. Soc. 74 (7) (1991) 1742–1744.

[137] E. Yeugo Fogaing, Y. Lorgouilloux, M. Huger, C.P. Gault, Young's modulus of zirconia at high temperature, J. Mater. Sci. 41 (2006) 7663–7666.

[138] Zirconia - physical and mechanical property comparison of the different types of zirconias. URL http://www.azom.com/article.aspx?ArticleID=133.

[139] T. Mitsuhashi, T. Ikegami, A. Watanabe, S. Matsuda, Thermodynamics of zirconia system with a possibility of intelligent characters, Proc. Int. Conf. Intell. Mater. 1 (1992) 155–158.

[140] J. Yang, Y. Okaa, Y. Ishiwatari, J. Liu, and J. Yoo, Numerical investigation of heat transfer in upward flows of supercritical water in circular tubes and tight fuel rod bundles, Nuclear Engineering and Design 237 (2006) 420–430.

[141] P. Billot, B. Cox, K. Ishigure, A. Johnson, C. Lemaignan, A. Nechaev, N. Petrik, E. Reznichenko, I. Ritchi, G. Sukhanov, Corrosion of zirconium alloys in nuclear power plants, In: TECDOC-684, International Atomic Energy Agency (IAEA), 1993.

[142] A.T. Motta, M.J. Gomes da Silva, A. Yilmazbayhan, R.J. Comstock, Z. Cai, and B. Lai, Microstructural characterization of oxides formed on model Zr alloys using synchrotron radiation, Journal of ASTM International 5 (3) (2008) 486–506.

[143] R. Piotrkowski, A. Denis, J. Kovacs, E.A. Garcia, Materials interactions during high temperature transients: Discussion about the use of the kinetic rate constants in zircaloy oxidation, Journal of Nuclear Materials 202 (1993) 252–265.

[144] E.A. Garcia, G. Beranger, Diffusion model for the oxidation of zircaloy-4 at 400C in steam: The influence of metallurgical structure – Precipitates and grain size, Journal of Nuclear Materials 273 (1998) 221–227.

[145] C. Zhang, P.R. Norton, The dissolution of oxide on α-Zr (1%Nb) and β-Zr(20%Nb) alloys, Journal of Nuclear Materials 300 (2002) 7–14.

[146] J. V. Cathcart, R. E. Pawel, R. A. McKee, R. E. Druschel, G. J. Yurek, J. J. Campbell, and S. H. Jury, Zirconium alloys in nuclear power, Reactor Materials Science Conference 45(6) (1978) 430–433.

[147] A. Couet, A.T. Motta, A. Ambard, D. Livigni, In-situ electrochemical impedance spectroscopy measurements of zirconium alloy oxide conductivity: relationship to hydrogen pickup, Corrosion Sci. 119 (2017) 1–13.

[148] C. Allison, G. Berna, R. Chambers, E. Coryell, K. Davis, D. Hagrman, D. Hagrman, N. Hampton, J. Hohorst, R. Mason, et al., Scdap/relap5/mod3. 1 Code Manual Volume Iv: Matpro–a Library of Materials Properties for Light-water-reactor Accident Analysis, DT Hagrman, NUREG/CR-6150, EGG-2720 4, 1993, 4–234.

[149] P. Wang, G.S. Was, Experimental validation capabilities at um - zr corrosion and hydrogen pick-up, Presentation at the CASL-FMC All-hands Meeting, 2017.

[150] P. Wang, G.S. Was, Addendum to Experimental validation capabilities at um - zr corrosion and hydrogen pick-up, Presentation at the CASL-FMC All-hands Meeting, 2017.

[151] J. A. Spitznagel, L. R. Fleischer, W. J. Choyke, The Effects of Ion Bombardment on the Thin Film Oxidation Behavior of Zircaloy-4 and Zr-1.0 Nb, Springer US, Boston, MA (1974) 87–99.

[152] C. Yan, R. Wang, Y. Wang, X. Wang, G. Bai, Effects of ion irradiation on microstructure and properties of zirconium alloys: A review, Nuclear Engineering and Technology 47 (3) (2015) 323 – 331.

[153] S. Hua-Hai, P. Shu-Ming, Z. Xiao-Song, S. Kai, W. Lu-Ming, Z. Xiao-Tao, Microstructure evolution of zircaloy-4 during ne ion irradiation and annealing: An in situ tem investigation, Chinese Physics B 23 (3) (2014) 036102.

[154] G. S. Was, T. R. Allen, Radiation damage from different particle types, in: Radiation Effects in Solids, Springer, 2007, pp. 65–98.

[155] M. J. Fluss, P. Hosemann, J. Marian, Charged-particle irradiation for neutron radiation damage studies, Characterization of Materials (2012) 1–17.

[156] S. Zinkle, L. Snead, Opportunities and limitations for ion beams in radiation effects studies: bridging critical gaps between charged particle and neutron irradiations, Scripta Materialia 143 (2018) 154–160.

[157] A.T. Motta, A. Yilmazbayhan, R.J. Comstock, J. Partezana, G.P. Sabol, B. Lai, and Z. Cai, Microstructure and growth mechanism of oxide layers formed on Zr alloys studied with micro-beam synchrotron radiation, Journal of ASTM International 2 (5) (2005) 205–231.

[158] P. Wang, G.S. Was, Recent updates to Experimental validation capabilities at um - zr corrosion and hydrogen pick-up, 2018.

[159] A. Zielinski, S. Sobieszczyk, Hydrogen-enhanced degradation and oxide effects in zirconium alloys for nuclear applications, International Journal of Hydrogen Energy 36 (2011) 8619-8629.

[160] J.J. Kearns, Diffusion coefficient of hydrogen in alpha zirconium, zircaloy-2, zircaloy-4, Journal of Nuclear Materials 43 (1972) 330–338.

[161] T. Smith, An ion beam study of hydrogen diffusion in oxides of Zr and Zr-Nb, *Journal of Nuclear Materials* 166 (1989) 300–306.

[162] D. Khatamian, Hydrogen diffusion in oxides formed on surfaces of zirconium alloys, *Journal of Journal of Alloys and Compounds* 253–254 (1997) 471–474.

[163] M. Tupin, F. Martin, C. Bisor, R. Verleta, P. Bossis, J. Chene, F. Jomard, P. Berger, S. Pascal, N. Nuns, Hydrogen diffusion process in the oxides formed on zirconium alloys during corrosion in pressurized water reaction conditions, Corrosion Science 116 (2013) 1–13.

[164] S. Saraf, M. Markovich, A. Rothschild, Defect chemistry of Pn junctions in complex oxides, Phys. Rev. B 82 (2010) 245208.

[165] A.R. Hassan, A. El-Azab, M. Manuel, Electrochemical effects of isolated voids in uranium dioxide, J. Phys. Chem. Solid. 75 (4) (2014) 550–557.

[166] M. Reyes, A. Aryanfar, S.W. Baek, J. Marian, Multilayer interface tracking model of zirconium clad oxidation, Journal of Nuclear Materials 509 (2018) 550–565.

[167] M. Reyes, P. Wang, G.S. Was, J. Marian, Experimentally-validated model of zircaloy clad oxidation under irradiation, Journal of Nuclear Materials: in preparation for publication.

[168] M.W. Chase, NIST-JANAF Themochemical Tables, Fourth Edition, J. Phys. Chem. Ref. Data Monograph 9 (1998) 1-1951. National Institute of Standards and Technology Chemistry WebBook, SRD 69, URL https://webbook.nist.gov/cgi/cbook.cgi?ID=C1314234&Mask=2